HIGH CYCLE FATIGUE OF ADDITIVELY MANUFACTURED INCONEL 625

A Thesis
Presented to
The Academic Faculty

by

Alvaro Espejo Abela

In Partial Fulfillment
of the Requirements for the Degree
Master's in Mechanical Engineering in the
Georgia Institute of Technology

Georgia Institute of Technology
December 2020

COPYRIGHT © 2020 BY ALVARO ESPEJO ABELA

HIGH CYCLE FATIGUE OF ADDITIVELY MANUFACTURED INCONEL 625

Approved by:

Dr. Richard W Neu, Advisor
School of Mechanical Engineering
Georgia Institute of Technology

Dr. Antonia Antoniou
School of Mechanical Engineering
Georgia Institute of Technology

Dr. Aaron Stebner
School of Mechanical Engineering
Georgia Institute of Technology

Date Approved: December 1, 2020

[To the students in Dr. Richard W. Neu's group and to Dr. Richard W. Neu]

ACKNOWLEDGEMENTS

The following project has been developed in the Georgia Institute of Technology in the research group of Dr. Richard W. Neu. This work was funded in part by the US Department of Energy funded project, “Digital Twin Model for Advanced Manufacture of a Rotating Detonation Engine Injector”, Award No DE-FE0031644, led by Southwest Research Institute with partner Aerojet Rockdyne.

TABLE OF CONTENTS

LIST OF TABLES

LIST OF FIGURES

LIST OF SYMBOLS AND ABBREVIATIONS

AF	As Fabricated.
AM	Additive Manufacturing.
E	Young Modulus.
E-PBF	Electron Powder Bed Fusion.
HCF	High Cycle Fatigue.
HIP	Hot Isostatic Pressing.
IN718	Inconel 718.
L-DED	Laser Directed Energy Deposition.
L-PBF	Laser Powder Bed Fusion.
NSA	NIST Alternative Stress Relief.
PSPP	Processing Structure Properties Performance.
SA	Standard Anneal.
SEM	Scanning Electron Microscope.
L-PBF	Laser Powder Bed Fusion.
SR	Stress Relief.
UTS	Ultimate Tensile Strength.
VED	Volumetric Energy Density.
YS	Yield Strength.

SUMMARY

This research aims to investigate the influence of the microstructure, defect features, and surface roughness on the high cycle fatigue (HCF) strength of IN625 manufactured using Laser Powder Bed Fusion (L-PBF) additive manufacturing (AM) process. 11 AM builds each containing several fatigue test specimens with axis of specimen oriented in either the z-direction (build direction) or transverse direction were manufactured to explore the influence of variations in laser scan speed, hatch spacing, and L-PBF machine system. These processing conditions resulted in variations in microstructure, defect features, and surface roughness, all of which can influence fatigue strength. All specimens were stress-relieved before removal from build plate and then a hot isostatic pressing (HIP) was performed. Specimens were tested in either as-is condition, with no further machining or polishing, or in a polished condition to establish the role of surface roughness on fatigue strength. The fatigue strength of each specimen was determined using a step test method. To establish a reference stress-life curve and to validate the step test method, fatigue tests were also conducted on a cold-rolled IN625 sheet having similar strengths as the AM specimens. Stress-life curves that include the influence of microstructure are estimated using the fatigue strength data and the reference stress-life curve from the wrought IN625. The fatigue fracture surfaces were characterized with SEM microscopy to determine the microstructure feature associated with fatigue crack nucleation and understand the variability of the fatigue results. Average roughness for all builds was measured to find trends with the high cycle fatigue results. Tensile test results for various mechanical properties including Young's modulus, yield strength, ultimate tensile strength and strain to failure z and xy specimens was plotted against fatigue strength to find trends. Fatigue strength was also evaluated against processing parameters to assess the influence and find optimal design parameters. Finally, mean stress correction methods for different R values were used to calculate average fatigue strength for designer specifications.

1. INTRODUCTION

Improvements in the quality of additive manufacturing techniques has opened doors to new possibilities in design and manufacture. Although the concept was first introduced by Raymond F. Jones in an article known as *"Tools of the Trade"* as early as the 1950's, industry adoption of additively manufacturing processes is relatively recent. Additive manufacturing offers improvements with respect to more traditional methods producing pieces with shapes that were previously not attainable with conventional casting, hot working, and machining processes. Unfortunately, new techniques bring new challenges, and additive manufacturing is no different. The purpose of this study is to study high cycle fatigue (HCF) of additively manufactured specimens manufactured by the Laser Powder Bed Fusion (L-PBF) process and find correlations between tensile mechanical properties, internal porosity and roughness for optimal design specifications and future studies with IN625. Therefore, the ultimate motivation is to obtain just as good fatigue performance as traditional methods, or improve them at the same time as conserving the improvements that additive manufacturing brings to industry applications, which will give way to new findings and designs.

Although specimens with good yield strength tend to obtain high fatigue life, it is not always the case. This is the motivation behind the tensile tests and the comparison of static mechanical properties with fatigue stress-life. Furthermore, the design of experiments was set up to introduce variability to the results by modifying processing AM parameters. This will underline the best design parameters than generate optimal results for the 11 available builds.

Due to the nature of process, additive manufactured parts contain defects depending on the processing parameters. Although they can be optimized to some extent, the surfaces will have a specific roughness and internal defects caused by unfused material. High roughness profiles and porosity have been found to be detrimental to high cycle fatigue properties. The motivation is to correlate roughness measurement results with fatigue life. In many cases, these properties correlate better than static mechanical properties, so a specific design of experiments was created to understand the impact of surface finish and internal defects.

In other words, the objective is to create a design of experiments for AM L-PBF IN625, obtain data from tensile tests, HCF testing, roughness tests and microstructure measurements to design a machine learning model than can be used by designers in the future. More in depth explanation of this process is detailed in the next chapter.

2. BACKGROUND

The motivation of the study is shown in FIGURE 1. The objective is to establish process-structure-property-performance (PSPP) relationships using machine learning methods, highlighted by the yellow boxes in the diagram. To achieve this, the first step is to develop a database by creating different structures generated by different process parameters. For this project, a design of experiment was developed, which consisted in manufacturing different builds of fatigue, tensile, and microstructure characterization specimens with the objective of collecting history information, treating each of these specimens as a discretized digital volume. Then, the critical features and attributes that control properties (tensile and high cycle fatigue) were characterized. This structural information of the different specimens is put into a specific form that can be used in machine learning methods. The purpose of this tool is to then get a component, collect processing history of different locations within that component and relate those processing parameters to structure to predict local properties, in this case for high cycle fatigue (HCF). This model can then be used for design specifications, process optimization, performance prediction, quality assurance, qualification and certification. This thesis reports on the work to generate the structure and property database to achieve this objective.

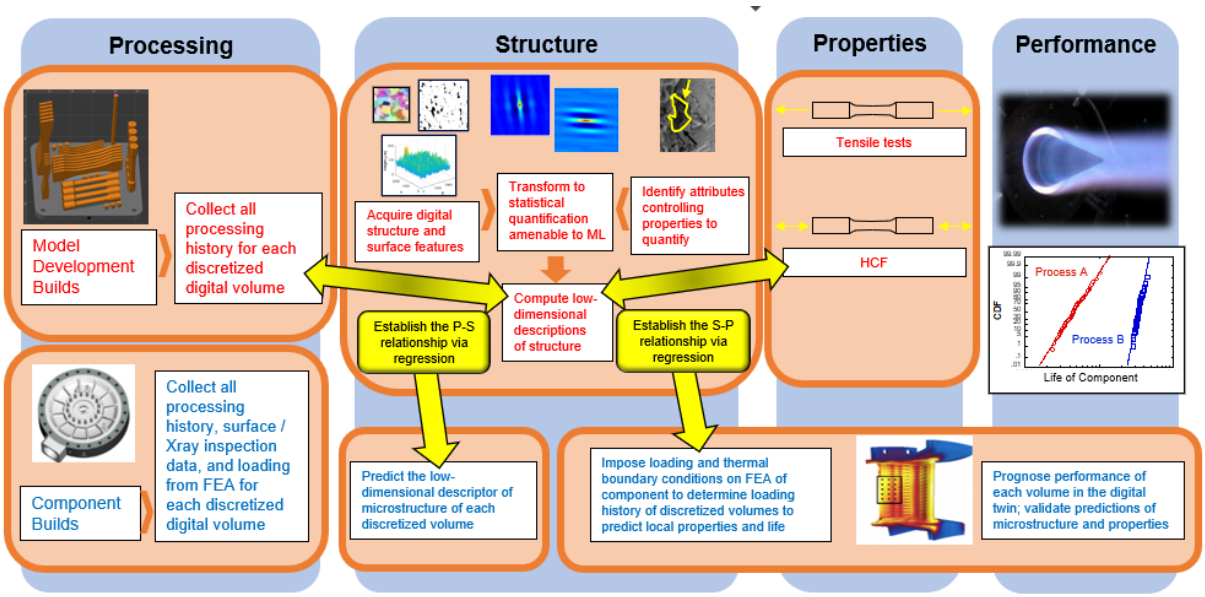

FIGURE 1: PSPP map for IN625 project.

2.1. Additive manufacturing

Additive manufacturing (AM) has opened the gates to new forms of design and production of parts. Some of the benefits of AM include:

1. Reduce number of parts and process steps to fabricate a component, which replaces multiple *"subtractive, joining and formative"* [1] processes. Moreover, further machining is normally not needed unless the part requires a specific roughness or polish finish.
2. Increase in automation.
3. Reduction in waste.
4. Constraint reduction for different geometrical shapes that cannot be readily manufactured by conventional methods.

In particular, IN625 can effectively be manufactured by different AM processes including E-PBF (Electron Powder Bed Fusion), L-PBF (Laser Powder Bed Fusion), L-DED (Laser Directed Energy Deposition) and binder jetting. The methodology used for this project was Laser Powder Bed Fusion (L-PBF).

2.1.1. Laser Powder Bed Fusion

There are two main laser-based processes involving PBF: L-PBF (Laser Powder Bed Fusion) and SLS (Selective Laser Sintering). SLS employs a high in energy laser to partially melt powder into the desired shape by scanning the laser over the different layers [2]. This process however does not fully melt the material; it heats it enough to fuse the particles at a molecular level [3]. On the other hand, L-PBF (see FIGURE 2) provides sufficient powder so as to fully melt the powder for fusion. This process normally requires additional stress relief while on the build plate but is an effective way of synthesizing titanium alloys, steels, and Ni-base alloys like IN625 or IN718. Both methods are selective which means they target certain parts of the powder to create the desired part.

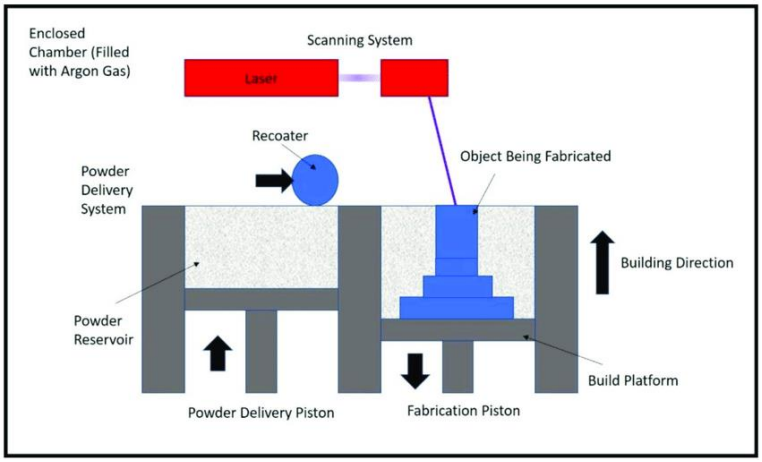

FIGURE 2: Laser Powder Bed Fusion [4].

The microstructure and properties of parts built by PBF are anisotropic and therefore the influence of orientation needs to be considered. FIGURE 3 shows the two possible build directions (among many others). These directions will affect mechanical and fatigue properties, as additional manufacturing can lead to certain anisotropy.

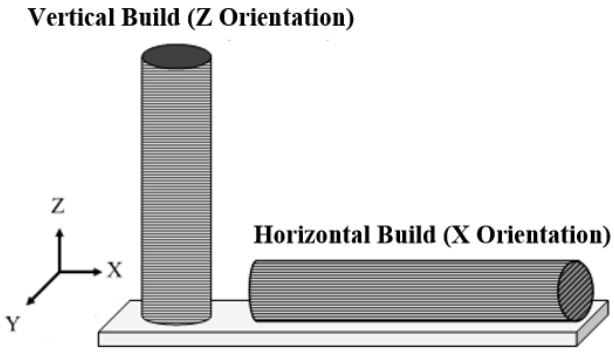

FIGURE 3: Z and XY build directions [19].

2.1.2. Additive manufacturing parameters for Laser Powder Bed Fusion

There are several parameters that can be modified in the L-PBF process to optimize properties to the desired applications. These include thickness of the layers **t** (FIGURE 4) , powder size, substrate temperature, scan angle (), hatch spacing **D** (FIGURE 6), scan speed **V** and laser power **P**. Further parameters will be related to post-processing of laser manufactured parts.

Hatch spacing is the distance between two consecutive beam passes, measured from the center of one beam pass to the next. A larger spacing will significantly reduce production time, while thinner spacings produced finer features but increase the lead time of the process [5]. Having a larger hatch spacing will require a larger diameter laser spot size to avoid the formation of pores within the part. Note that there is no real "spacing" between every pass of the laser, as the melt pool between them overlap. This is necessary ensure the melting of all the powder together, reducing the formation of defects. These beams can be approximated to a Gaussian beam, where the strength of the laser beam is higher in the center compared to the edges.

The scan strategy is the rotation of the scanning direction after each layer. Two common scan strategies are 67 and 90 degrees with counterclockwise rotation. Moreover, scanning direction can be alternating or unidirectional, the second being more time consuming. The scan angle, on the other hand, relates to the angle between the position of the laser source and the location of the build, with larger angles at locations near the edges of the build. Some of these parameters are used to calculate the volumetric energy density (VED) [6]:

$$VED = \frac{P}{VDt} \quad \text{[eq. 1]}$$

This represents the amount of energy supplied to the local spot in the powder bed per unit of volume. The volumetric energy density will affect the geometry of the melt pool, the quality of the fusion, the cooling rate and consequently the microstructure of the manufactured part [7].

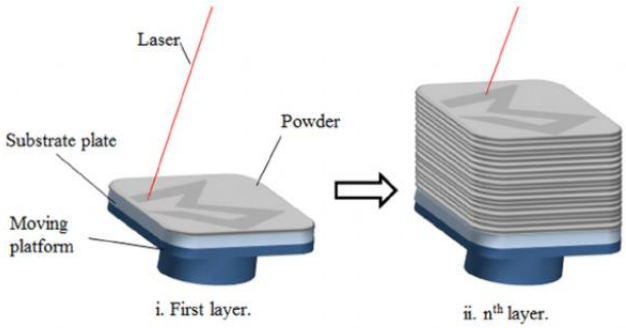

FIGURE 4: Different layers and their thickness [19].

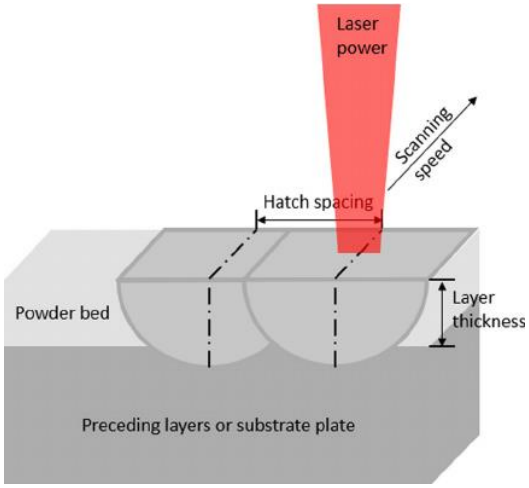

FIGURE 5: Hatch space [19].

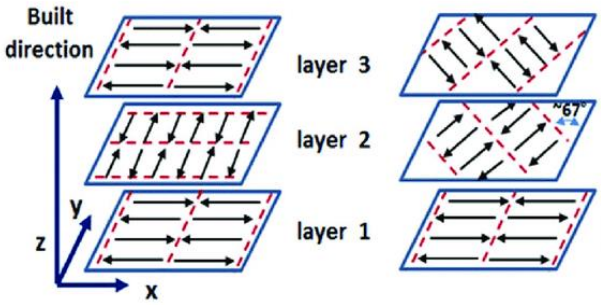

FIGURE 6: 90 vs 67 degrees scan angles [18].

2.2. Inconel 625

Inconel 625 (IN625) is a high strength, high fatigue resistance Ni-base superalloy. By definition, superalloys are alloys capable of withstanding temperatures at a high fraction of their melting point [8]. The alloy receives its name from the trademark *"Inconel"*, which belongs to Special Metals Corporation, a company based in New Hartford, USA. IN625 belongs to a family of austenitic nickel-chrome alloys with different compositions [9] [10] [11], which can be found in TABLE 1. This alloy is considered a modification of IN718 so the solidification studies carried out for IN718 can be used to extrapolate the behavior of IN625.

IN625 has a specific composition that gives excellent mechanical and fatigue properties as well as resistance to corrosion. Mo and Cr are responsible for a high corrosion resistance and strength properties. Elements such as Nb and Fe are used to obtain a higher degree of strength in the material. Other elements including Ti and Al are used for refining and for welding purposes [12].

Common applications of this alloy include supercritical water reactors or high temperature engines [13], and is therefore highly used by the aerospace and energy industries. These outstanding properties are reflected in the cost, and Inconel parts are considerably more expensive than stainless steels, due to a high market price of the elements used in the composition, but have better higher temperature strength and durability.

TABLE 1: Different compositions for various Inconel superalloys. [21]

Inconel alloy	Element, proportion by mass (%)																		
	Ni	Cr	Fe	Mo	Nb & Ta	Co	Mn	Cu	Al	Ti	Si	C	S	P	B	W	V	Y	Zr
600	≥72.0	14.0–17.0	6.0–10.0				≤1.0	≤0.5			≤0.5	≤0.15	≤0.015						
601	58.0-63.0	21.0 - 15.0	Remainder			≤1.0	≤1.0	≤1.0	1.0 - 1.7		≤0.50	≤0.1	≤0.015						
617	44.2–61.0	20.0–24.0	≤3.0	8.0–10.0		10.0–15.0	≤0.5	≤0.5	0.8–1.5	≤0.6	≤0.5	0.05–0.15	≤0.015	≤0.015	≤0.006				
625	≥58.0	20.0–23.0	≤5.0	8.0–10.0	3.15–4.15	≤1.0	≤0.5		≤0.4	≤0.4	≤0.5	≤0.1	≤0.015	≤0.015					
690	≥58	27–31	7–11				≤0.50	≤0.50			≤0.50	≤0.05	≤0.015						
718	50.0–55.0	17.0–21.0	Remainder	2.8–3.3	4.75–5.5	≤1.0	≤0.35	≤0.3	0.2–0.8	0.65–1.15	≤0.35	≤0.08	≤0.015	≤0.015	≤0.006				
X-750	≥70.0	14.0–17.0	5.0–9.0		0.7–1.2	≤1.0	≤1.0	≤0.5	0.4–1.0	2.25–2.75	≤0.5	≤0.08	≤0.01						
C-276	Remainder	14.5-16.5	4.0-7.0	15.0-17.0		≤2.5	≤1.0				≤0.08	≤0.01	≤0.03	≤0.04		3.0-4.5	≤0.35		
602 CA	Remainder	≤26.0	11				0.15	0.1	2.4	0.2	0.5	0.25						0.12	0.1
22	Remainder	20.0-22.5	2.0-6.0	12.5-14.5		≤2.5	≤0.5				≤0.08		≤0.02	≤0.02			≤0.35		
725	55.0-59.0	19.0-22.5	Remainder	7.0-9.5	2.75-4.0		≤0.35		≤0.35	1.0-1.7	≤0.20	≤0.03	≤0.01	≤0.015					

2.3. Solidification of Inconel 625

Different cooling profiles after solidification and processes will affect the microstructure of the material. The existence of different phases will impact the resulting mechanical properties and fatigue performance.

FIGURE 8 shows the TTT diagram for wrought IN625, although TTT diagrams will slightly differ depending on the composition. The primary phases that can form include carbides (MC, M_6C, $M_{23}C_6$), γ", Laves, and delta. These phases can improve or impoverish fatigue properties. The most relevant phases are their effects are described below.

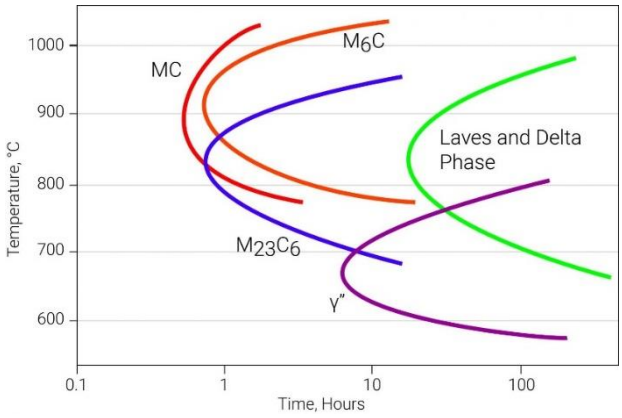

FIGURE 8: TTT diagram of IN625 [7]

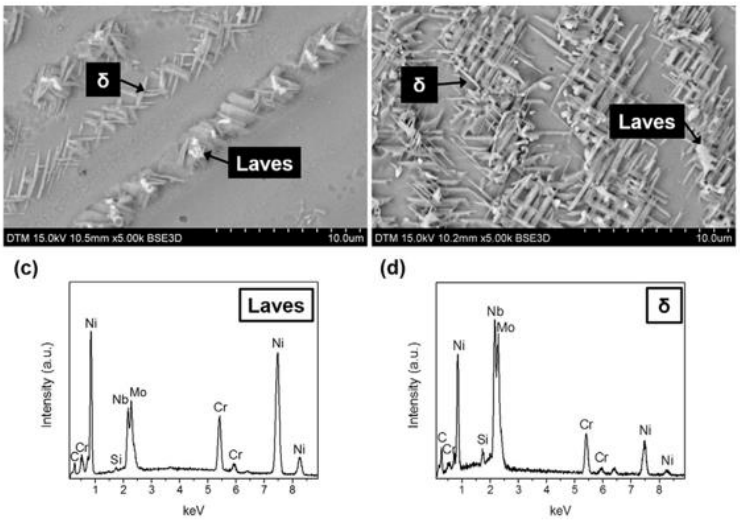

FIGURE 7: BSE images of the δ-Ni 3 (Nb, Mo) and the Laves phases formed in the Inconel 625 [61].

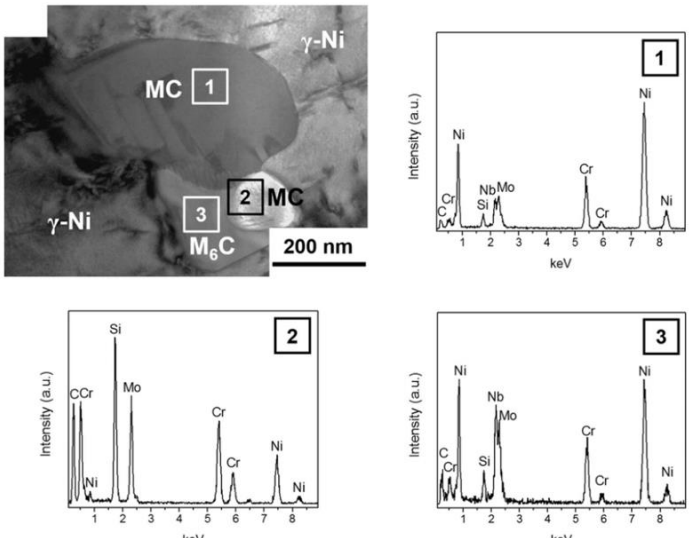

FIGURE 9: Example of carbides detected at the dendritic boundaries of the γ-Ni crystals of Inconel 625 clads [63].

2.3.1. Laves and carbides

A common microstructure feature of IN625 are Laves phases, which are intermetallic compounds that take the form of A_2B. The approximate composition of this phase can be found in FIGURE 7. Niobium is the primary element responsible for Laves phases and carbides that appear as a result of the enrichment of the interdendritic liquid [14]. These phases have been found to significantly reduce room temperature ductility and ultimate tensile strength for IN718 [15]. This reduction is caused by several mechanisms, being brittle fracture the most dominant. Moreover, as they take large amounts of Nb, the matrix is depleted of the main hardening agent forming coherent g" phase. In order to minimize the Laves and delta phases and hence increase toughness, the iron and silicon content can be reduced. TABLE 2 shows Charpy V-Notch tests of two different composition samples.

TABLE 2: V-Noch Charpy for standard vs Low Fe, Si specimens. [6]

Filler Wire	Test Temp.	Charpy V-Notch Impact Energy
Standard	RT -320°F	42.3 37.2
Low Fe & Low Si	RT -320°F	152.7 127.7

A loss in ductility and toughness can also be produced by the bands of carbides (see FIGURE 9 for composition), which can debond and coalesce to localize the fracture. However, the impact of carbides to toughness and ductility has been shown to be nowhere near as detrimental as Laves phase [16].

Moreover, Cieslak et al. [14] concludes that microstructure is heavily influenced by *"minor alloying elements*" such as C and Si. The presence of carbon is responsible for the formation of the MC carbides. However, it can reduce Laves for low Si alloys, so fine tuning is necessary to obtain optimal performance of parts. Furthermore, Si causes the formation of Laves and M_6C carbides

for low carbon samples. If both elements are present at a high composition, high amounts of Laves phase and carbides in the form of MC will occur.

Some processes can be performed to mitigate the effect or reduce carbide and Laves phases. As for Laves, solution annealing can significantly reduce or eliminate them. MC carbides (e.g., NbC) form a stable phase and cannot be eliminated by traditional methods. One way of eliminating carbides is solution annealing "at 1093°C or higher" [17] for an exposure of 1 hour.

2.3.2. Delta phase

The delta phase is shown in FIGURE 5. This phase is known to form in conventional solid solution strengthened when subjected to high temperatures for an extended time period. Industry standard stress-relief heat treatments for 1 hour at 870°C has been shown to generate a significant amount of this phase in L-PBF [18]. Its chemical composition is Ni_3Nb (FIGURE 7), forming a D0a structure. Delta phases can be easily observed after etching and form a "needle-like structure".

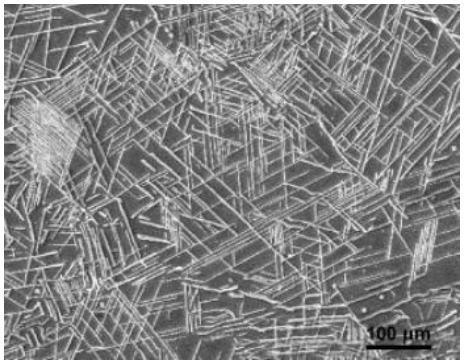

FIGURE 10: Delta phase precipitation of Inconel 718 [8].

Homogenization treatments can be used to mitigate or eliminate formations of delta phase. Zhang et al. [19] found out that homogenization treatments will reduce or eliminate delta phase formation (see section 2.4.4.).

2.3.3. Fine tuning

The influence of the various alloying elements in IN625 on microstructure and properties are summarized in TABLE 3 and TABLE 4, respectively. Taking Nb as an example, minimizing its concentration in the alloy has a very positive effect on reduction of carbides, Laves phase and delta phase during solidification and precipitation during heat treatments. However, reducing Nb can also have a negative effect on mechanical properties, as it greatly reduces strength of the main Nickel matrix.

TABLE 3: Effect of microstructure of fine-tuning composition [7].

Element	Minimise Formation of Niobium Carbide During Solidification	Minimise Formation of Laves Phase During Solidification	Minimise Carbide Precipitation During Heat Treatment	Minimise Laves and Delta Precipitation During Heat Treatment	Avoid γ" Precipitation
Minimise Nb	Positive Effect	Positive Effect	Positive Effect	Positive Effect	Positive Effect
Minimise Fe	No Effect	Positive Effect	No Effect	No Effect	No Effect
Minimise Mo	No Effect	Positive Effect	Positive Effect	Positive Effect(2)	No Effect
Minimise Al & Ti	No Effect	No Effect	No Effect	No Effect	Positive Effect
Minimise C	Positive Effect	Negative Effect(1)	Positive Effect	No Effect	No Effect
Minimise Si	No Effect	Positive Effect	Negative Effect	Positive Effect(2)	No Effect

Notes:
1. The effect of a lower carbon/niobium ratio probably outweighs the effect of minimising the solidification range.
2. Low molybdenum and/or silicon retard the formation of Laves phase, but have little effect on the formation of Delta phase.

TABLE 4: Effect of minimizing composition on properties of Alloy 625 [7].

Element	Strength	Corrosion Resistance	Weldability
Minimise Nb	Negative Effect	No Effect	Positive Effect
Minimise Fe	Negative Effect	No Effect	Positive Effect
Minimise Mo	Negative Effect	Negative Effect	Positive Effect
Minimise Al & Ti	Negative Effect(1)	No Effect	Negative Effect(2)
Minimise C	No Effect	Negative Effect(3)	Positive Effect
Minimise Si	No Effect	Negative Effect(3)	Positive Effect

Notes:
1. Aluminium and titanium are only important to strength if precipitation hardening is employed.
2. Some aluminium and titanium are helpful to weldability, but the minimum levels required are not known.
3. If grain boundary carbides are necessary for corrosion resistance, minimum levels of carbon and silicon need to be specified.

2.4. Additive manufacturing of Inconel 625

2.4.1. Mechanical properties of Inconel 625

As for many other alloys, mechanical properties will highly depend on the different manufacturing processes. However, according to the MMPDS-14 [20], for annealed material at room temperature, the Young's modulus is 206 GPa and Poisson ratio is 0.28. Increasing the temperature up to 900°C causes a decrease in the Young's Modulus of 50% and an increase of the Poisson ratio of 20%.

Typical mechanical properties for different forms and conditions of Inconel 625 are provided in TABLE 5.

TABLE 5: Nominal room temperature mechanical properties [21].

Form and Condition	Tensile Strength	Yield Strength	Elongation	Reduction of area	Hardness, Brinell
	MPa	MPa	%	%	
ROD, BAR, PLATE					
As-Rolled	827-1103	414-758	30-60	40-60	175-240
Annealed	827-1034	414-655	30-60	40-60	145-220
Solution-Treated	724-896	290-414	40-65	60-90	116-194
SHEET and STRIP					
Annealed	827-1034	414-621	30-55	-	145-240
TUBE and PIPE,					
COLD-DRAWN					
Annealed	827-965	414-517	30-55	-	-
Solution-Treated	689-827	276-414	40-60	-	-

TABLE 6 summarizes the same mechanical properties of IN625 according reported for different additive manufacturing processes, post processing and orientation. The three methods are commonly used: L-DED (Laser Direct Energy Deposition), E-PBF (Electron Powder Bed Fusion), and L-PBF (Laser Powder Bed Fusion). The post-processing of these parts was one or a combination of the following: AF (As Fabricated), SR (Stress Relief), SA (Standard Anneal), and HIP (Hot Isostatic Pressing). Each of these treatments is described in more detail below.

2.4.2. Annealling and Stress Relief Treatments

Annealing is performed to improve ductility, reduce internal stresses and refine the internal structure by increasing homogeneity while reducing brittleness. Annealing treatments for IN625 range from 900 to 1200°C for 1 hour [22], which are typically temperatures above the recrystallization temperature of the metal.

Stress relief, however, consists of heating to a predetermined temperature below recrystallization temperature followed by cooling in air [23]. For the standard stress relief, parts are exposed to a temperature of 1600°F (871°C) for an hour. On the other hand, the alternative treatment subjects builds to 1475°F (802°C) for 4 hours with the aim to reduce the formation of delta phase which can be detrimental to ductility and fatigue properties. These stress relief treatments are typically performed before the parts are removed from the build plate.

2.4.3. Hot Isostatic Pressing (HIP)

The purpose of Hot Isostatic Pressing, also known as HIPing, illustrated in FIGURE 11, is to reduce internal porosity, which improves the mechanical properties. The part is subjected to a high isostatic pressure at a high temperature using an inert gas [25]. For IN625, the temperature the part is subjected varies between 1170 to 1280°C and the pressure is 100 to 150 MPa. The main objectives of HIPing include reducing internal porosities, removing internal defects and possibly the rejuvenation of fatigue or creep damaged parts. Hot Isostatic Pressing or HIPing treatment can reduce internal porosities; however, HIPping will not be successful in minimizing porosity in cases

where the manufactured parts contain a high porosity after the build process. With ideal processing and HIPping parameters, the porosity is less than 0.1-0.25% [26].

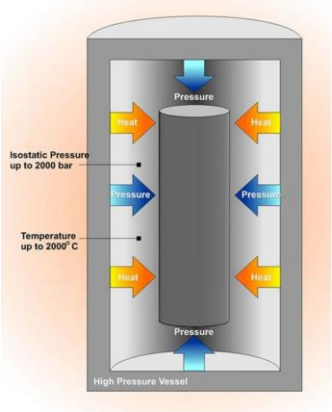

FIGURE 11: Diagram describing the HIPing process [24].

2.4.4. Homogenization treatment

Homogenization treatments are often carried out to mitigate the formation of the delta phase for IN625. The typical treatment is similar to annealing but includes subjecting components to a higher temperature. 1150°C for 1 hour was found to be an effective homogenization treatment of L-PBF IN625. This treatment reduces the delta phase formation, but it has been shown to promote grain growth, which can be deleterious to mechanical properties [27].

TABLE 6 shows shows the tensile properties that have been obtained on AM IN625. It shows that very high yield strengths and ductilities are possible, though there is considerable variability in properties reported. Note that the majority of specimens had 0.2% offset yield strengths (YS) that exceeded 400 MPa, with 800 MPa being the highest value (data point 8). Nevertheless, some low values where observed for E-PBF (data points 11, 14), probably due to the annealing that occurs during the build due to the higher temperature in the build chamber. It is important to note that the different post-processing techniques will further affect mechanical properties.

TABLE 6: Mechanical properties of AM IN625 reported in the literature.

Data point label	Author	Year	Process	Post-Processing	Orientation	0.2% YS (MPa)	UTS, MPa	% Elongation	Reference
1	Xue	2007	L-DED	AF	X-Y	477	744	48	[28]
2	Xue	2007	L-DED	AF	Z	518	797	31	[28]
3	EOS	2010	L-PBF	AF	X-Y	725	990	35	[29]
4	EOS	2010	L-PBF	AF	Z	615	900	42	[29]
5	Betts	2011	L-PBF	AF	X-Y	384	898	60	[30]
6	Betts	2011	L-PBF	AF	Z	376	884	57	[30]
7	Yadroitsev	2009	L-PBF	AF	X-Y	720	1070	9	[31]
8	Yadroitsev	2009	L-PBF	AF	Z	800	1030	9	[31]

TABLE 6 continued

9	Optomec	2012	L-DED	AF	X-Y	694	1052	33	[32]
10	Optomec	2012	L-DED	AF	Z	490	829	43	[32]
11	Murr	2011	E-PBF	AF	X-Y	300	590	53	[33]
12	Murr	2011	E-PBF	AF	Z	410	750	44	[33]
13	Murr	2011	E-PBF	SA+HIP	Z	330	770	69	[33]
14	Murr	2011	E-PBF	SA+HIP	Z	230	610	70	[33]
15	Rombouts	2012	L-DED	AF	X-Y	480	882	36	[34] [35]
16	Rombouts	2012	L-DED	AF	Z	656	1000	24	[34] [35]
17	Amato	2012	L-PBF	SA+HIP	X-Y	380	900	58	[36]
18	Amato	2012	L-PBF	SA+HIP	Z	360	880	58	[36]
19	EOS	2011	L-PBF	SR	X-Y	720	1040	35	[37]
20	EOS	2011	L-PBF	SR	Z	650	930	44	[37]
21	Dutta	2011	L-DED	-	Z	598	795	14	[38]
22	MMPDS	2019		AMS 5666		414	827	30	

Although additively manufactured IN625 can achieve tensile properties comparable or better than wrought form, the fatigue strength many not necessarily correlate to the tensile properties. Defects such as porosity and high surface roughness may not significantly affect tensile properties, particularly the yield and ultimate strength, unless porosity is extreme, but can have considerable influence under cyclic loading. This is because local defects, acting as localized volumes where the cyclic stress is raised, drive the local fatigue crack formation process. Therefore, the objective is to understand the relationship between the local defects and their impact on fatigue crack formation and early crack growth.

The effects of these process parameter settings together with powder material characteristics on the variations of the resultant part quality in terms of density, material properties, dimensional quality, surface roughness, and defects are not well understood. [7]. Presently, these parameters are established by trial-and-error methods using simple relationships such as *VED* as guidance. Empirical data can help when designing new parts. FIGURE 12 shows how different combinations of scan speed and laser power will generate different depth to width melt pool ratios, with a ratio 0.5 considered close to optimal [39].

The common powder size used for IN625 is 15-45 μm in diameter, though small powder thickness variations with respect to the previous thickness has no noticeable effect on properties [40].

Criales et al. [41] experimented with different parameters to study the influence of processing parameters on the microstructure. The variables were scan angle (90° vs 67°), laser power, scan speed and hatch distance. The following conclusions were found:

- Larger energy densities lead to larger grain sizes.
- A scanning angle of 67° helps with the reduction of the relationship between laser power and speed vs. grain growth directions. It also obtains finer sized grains than 90°.
- Medium to high speeds and medium hatch distances are needed to obtain structures with nearly isotropic behavior.

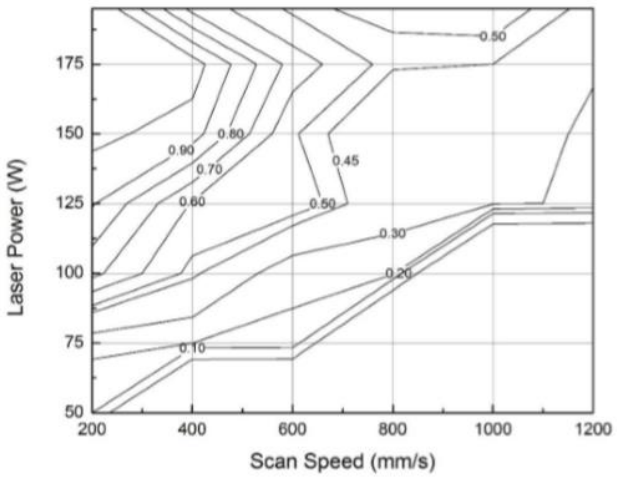

FIGURE 12: Melt pool depth to width ratios for different laser power and speed combinations for Inconel 625 (L-PBF). [21]

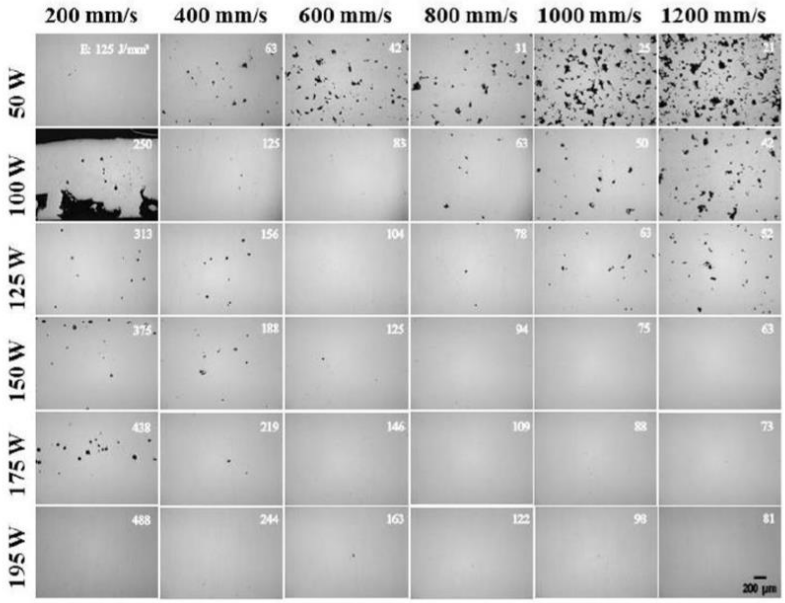

FIGURE 13: Microscope imaging for power and laser speed combinations for IN625 fabricated by L-PBF [21].

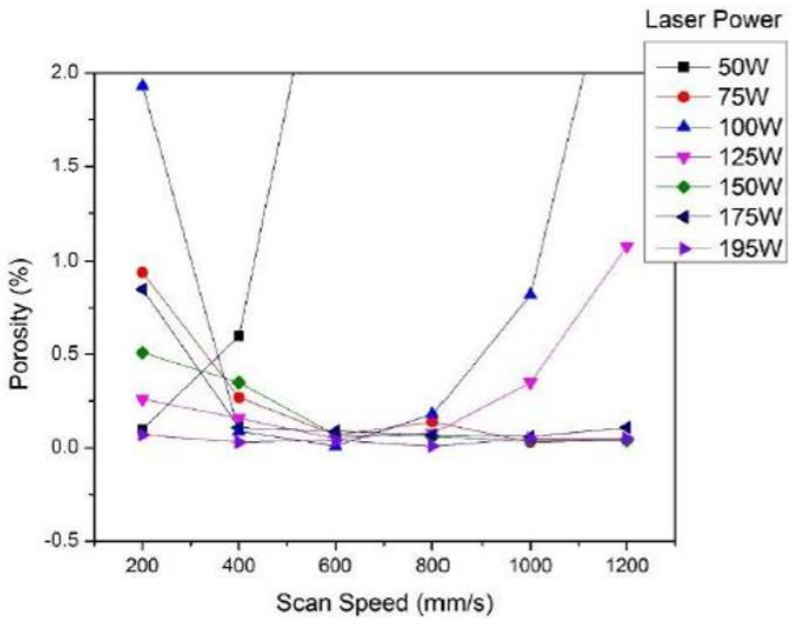

FIGURE 14: Porosity measurements (%) for different scan speeds and laser power [21].

FIGURE 13 shows optical microscope images showing porosity for different scanning speeds and laser power. FIGURE 14 shows the same information porosity quantified as a percentage. There is a clear trend: the higher the scanning speed and laser power, the lower the porosity. In other words, the higher the energy density provided by the scanner, the lower the porosity and the higher the relative density. However, very high energy densities with lead to keyholing defects, increasing porosity again as illustrated in FIGURE 15.

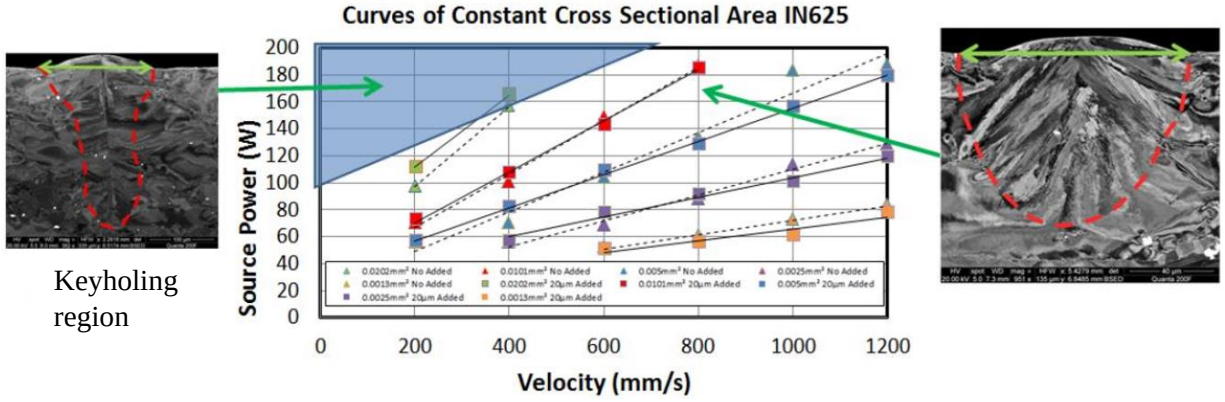

FIGURE 15: Experimental curves of constant cross-sectional area for IN625 and an annotation for the keyholing region. Colors represent a given cross sectional area. [33]

Inadequate combinations of the previous parameters will give way to AM defects. High VEDs are used to reduce internal porosity, but they can increase surface roughness [42]. However, roughness

and porosity can also be caused by very low VEDs. Moreover, higher roughness can also be caused by overhanging geometries due to the effect of gravity during solidification [26].

FIGURE 15 shows curves of constant cross-sectional area for a range of source power and laser velocity. The region where keyholing has been found to be generated is shown in blue. High power with low speeds will promote the formation of this defect and should therefore be avoided [33].

2.5. Fatigue of L-PBF parts

Fatigue describes the process of degradation associated with an applied cyclic load that is sufficient to cause of crack to nucleate, typically at some defect or heterogeneity of the microstructure, and the subsequent growth the crack and eventual failure of a component [43]. This phenomenon occurs in rotating machines and is one of the most likely causes of component failure. Fatigue processes can be classified according to the number of cycles until failure, distinguishing low cycle and high cycle fatigue. For this report, only high cycle fatigue (HCF) will be described, as it is the process the designed component will undergo. HCF includes processes with a high number of cycles that involve primarily elastic deformation. Stresses applied are typically less than the yield stress but plastic deformation is still occurring locally near internal stress concentrations associated with the microstructure or defects within the surface or on the surface [44].

The maximum stress generated by cyclic loading can be well under the yield strength of the material, meaning that parts can perform perfectly during a given time, but fail after the component has experienced several cycles. Some materials like steel or titanium have an **endurance limit** or **fatigue limit**, defined as the stress level that can be endured for infinite cyclic loads in a benign environment. However, this endurance limit can be highly affected and reduced by periodic overloads and corrosive and high temperature environments. Longer cycles than typically defined as the endurance limits (10^7 cycles) can result in other defects, often internal defects, be site of crack nucleation. Furthermore, this endurance limit is not strictly related to the material, as many variables can affect the fatigue life. These include surface finish or roughness, temperature, notch sensitivity, size, environment and reliability [45].

2.5.1. Fatigue review of previous work on L-PBF IN625

External and internal defects can reduce fatigue life of L-PBF parts. HCF strength is typically reduced by an increase in surface roughness [46]. Furthermore, build direction and the size of specimens affect fatigue life of L-PBF IN718, as it has been seen that this alloy can develop anisotropic columnar grain structures for certain processing parameters [47]. FIGURE 16 highlights the effects of post-processing treatments on grain structure.

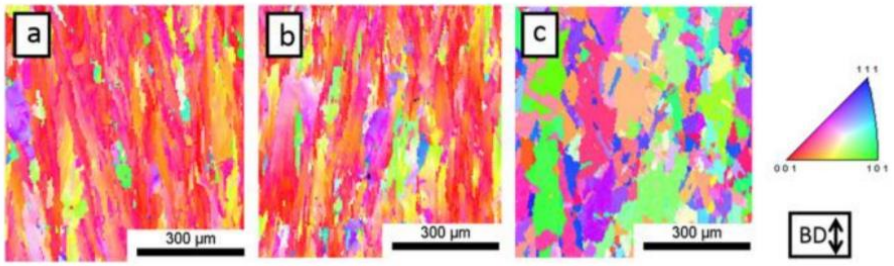

FIGURE 16: EBSD IPF map of (a) as built Inconel 718, (b) solution annealed Inconel 718, (c) post HIP Inconel 718. [50]

There has been some fatigue tests reported on AM IN625 in the literature. Koutiri et al. investigated the influence of the surface roughness on the HCF of IN625 with results shown FIGURE 17 suggesting an endurance limit around 200 MPa and that polishing the surfaces to remove the influence of surface roughness generally increases the fatigue life.

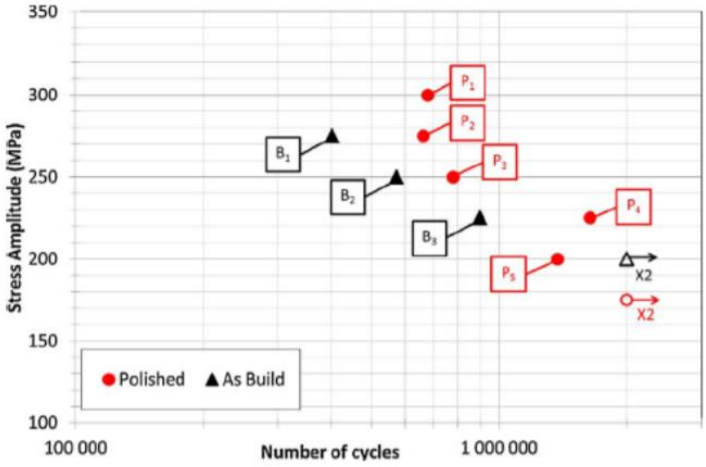

FIGURE 17: SN curve of IN625, fabricated using 180 W of power, 500 mm/s of laser speed and 70 µm of hatch spacing with no heat treatment tested under uniaxial loading with R = -1 [6].

FIGURE 18 shows results published by Witkin et al. *[48]* It can be inferred from the data that HIP and machining improve the fatigue properties to those similar to wrought. Hip with shot peening of the as-built condition almost has the same benefit as HIP and machining. However, data points show that the most important factor for this study was machining L-PBF specimens. It was found that machining before testing obtained very similar fatigue properties to wrought IN625 bar.

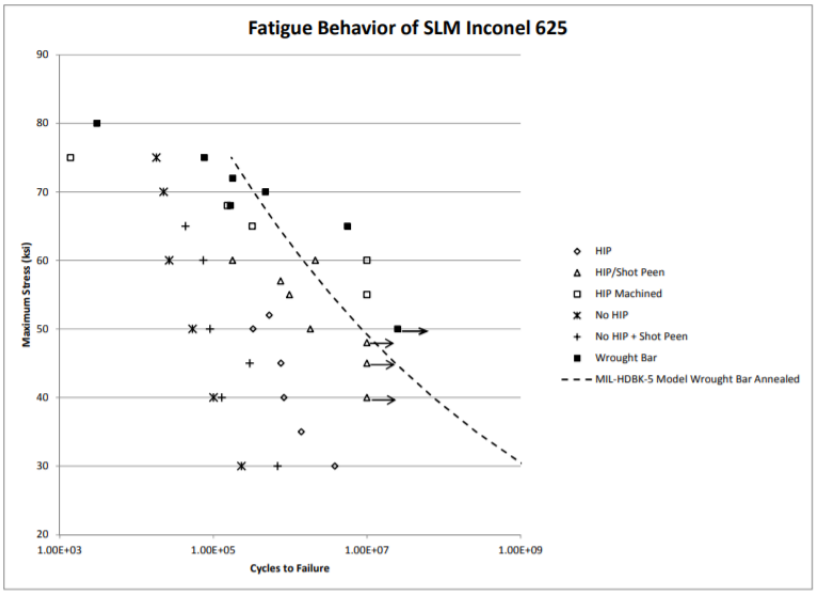

FIGURE 18: SN Data of IN625 from Witkin et al, fabricated per ASTM E466 (L-PBF parameters not specified by vendor), uniaxial loading with R = -1 [48].

In another study carried out by Witkin et al. [49] a few years later (FIGURE 19) no substantial difference between polished and as-is specimens was found. The absence of fatigue resistance improvement after abrasive and laser polishing was attributed by the authors to failure of the process to alter the stress concentration of the notch-like surfaces. Although average roughness was significantly improved (Sa value was reduced), the polishing made the features shallower but did not alter the interior. This meant that fatigue life was not increased because these features preserved similar elastic stress concentration after the polishing process.

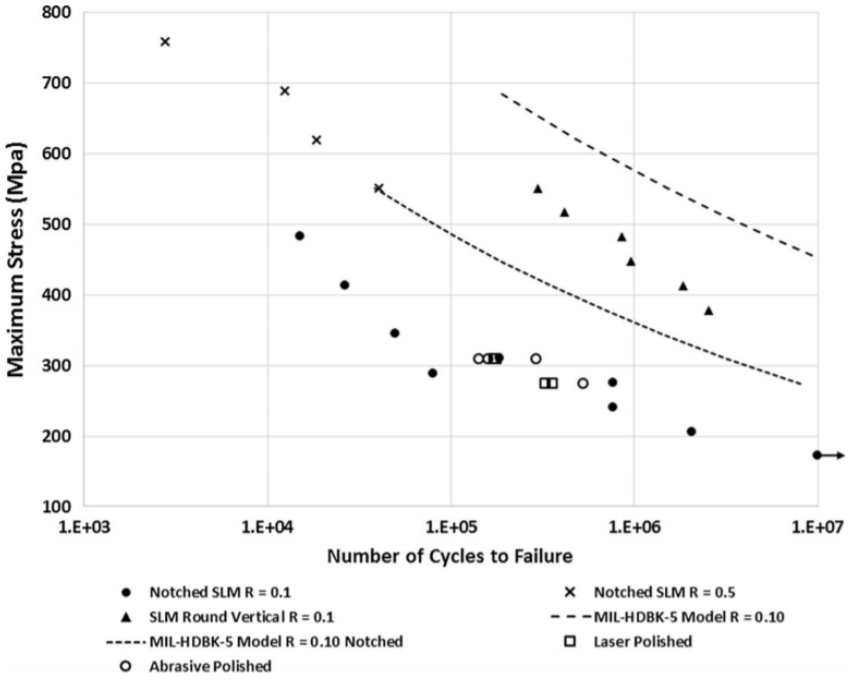

FIGURE 19: SN curve of fatigue results for L-PBF notched IN625 fabricated at 200 W of power, spot size of 30 μm, R=0.1 [49].

Anam carried out a cyclic fatigue investigation for IN625, varying build orientation and heat treatment (annealing), although the specifications of the different treatments are not clear in her work (50% of samples were heated to 1038°C for 1 hour in an argon-filled furnace for stress relief and quenched (see section 2.4.2) but the other 50% were not heat treated). However, as seen in FIGURE 20, the heat treatment did not have a large impact on fatigue performance. It shows the results of her investigation, revealing that building along the Z-axis (axial direction of fatigue specimens) lead to a lower fatigue life. Anam attributes this to z samples being more likely to develop defects such as voids caused by lack-of-fusion or gas entrapment.

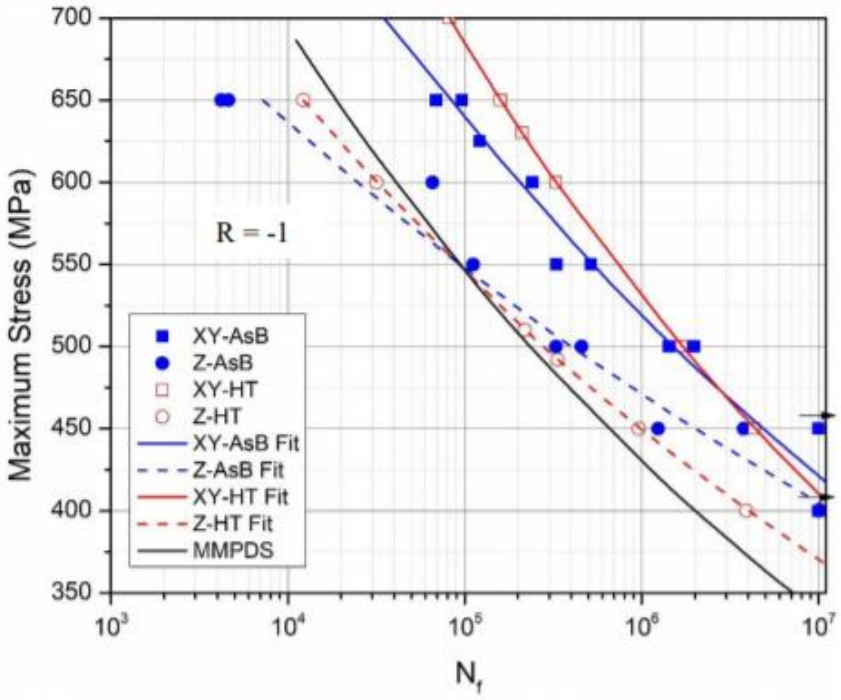

FIGURE 20: Plot of maximum stress versus cycles to failure for L-PBF IN625 fabricated using 195 W of power, scan speed of 800 mm/s, layer thickness of 20 µm, spot size of 100 µm and hatch spacing of 100 µm for samples with different build orientations and post-processing under uniaxial loading with R = -1 [39].

2.6. Fatigue crack initiation of IN625

Fatigue crack initiation can take different definitions. From a mechanical engineer standpoint, crack detection is the threshold for crack initiation. Materials engineers go deeper in their observation, and consider nucleation of defects along persistent slip bands or at an internal interface between microstructure features as a starting point of the fatigue crack [50]. The principal mechanism that drives crack nucleation of repeated loads in pure ductile metals is stated in Wood's postulate (1958): *"repeated cyclic straining of the material leads to different amounts of net slip on different glide planes"*. These displacements are responsible for the increase of surface roughening and can be observed as peaks and valleys in the surface. Once these valleys are generated, they serve as stress concentration points that aid in fatigue crack nucleation and further slipping.

2.6.1. Fracture surfaces and common defects of IN625

FIGURE 21 to FIGURE 23 show fatigue fractures of different IN625 specimens [51]. FIGURE 21 shows a HCF fracture surface from a wrought bar specimen. FIGURE 21b shows the origin of the fracture. FIGURE 21c magnifies the previous image and shows a detached feature from the nickel matrix, a carbide. Carbides reduce fatigue life due to several factors including increase brittle behavior as they act as stress risers and, as described in the background section, form due to specific cooling curves of the material. This feature can be found across different manufacturing processes and it is not a defect particular to L-PBF.

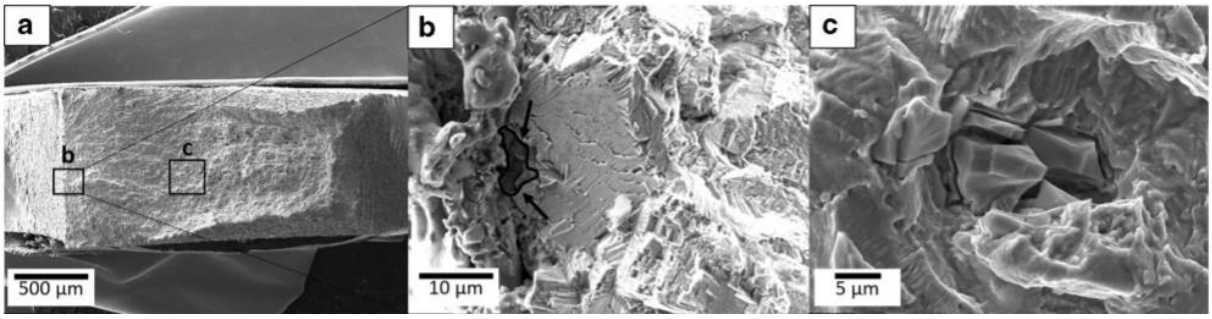

FIGURE 21: HCF fracture surface of a wrought bar IN625 specimen hot rolled extruded and annealed at different magnifications studied using SEM fractography [51].

FIGURE 22 shows the fatigue fracture surface of as-deposited additively manufactured IN625 fabricated using the MELD process. It can be clearly seen on this image the river marks that point towards the fracture initiation site, which in this case forms a cracked surface instead of a cracked particle as in the last example. Finer microstructures consisting of reduced grain and carbide size reduces brittle behavior and generate surface fractures like the one shown in FIGURE 22d.

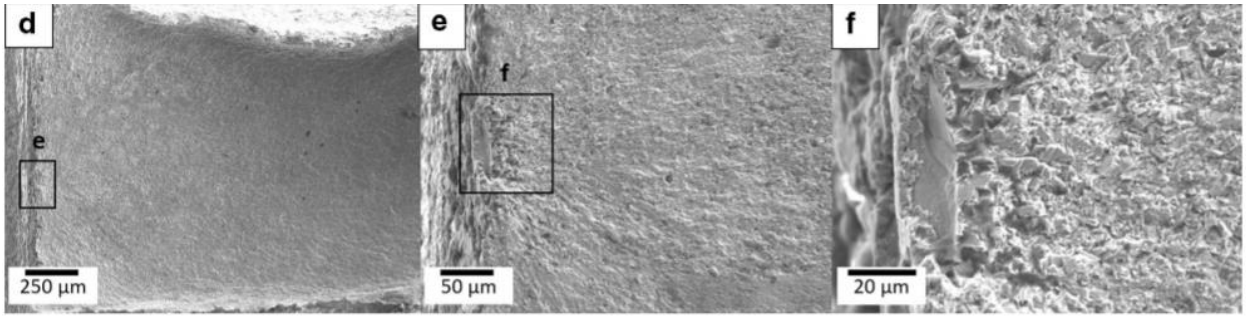

FIGURE 22: HCF fracture surface of as-deposited Inconel 625 fabricated using the MELD process [51].

Another type of fracture that can be observed in L-PBF IN625 is interlayer delamination. Due to the nature of the manufacturing process, the material forms layers that may fracture or debond when subjected to cyclic loads (FIGURE 23).

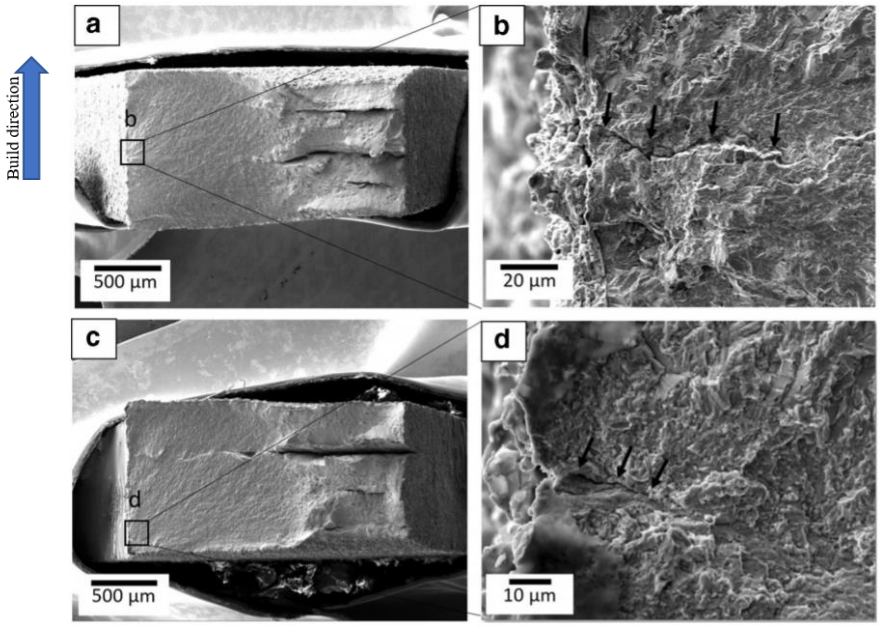

FIGURE 23: HCF fracture surface caused by delamination of as-deposited IN625 fabricated by the MELD process [51].

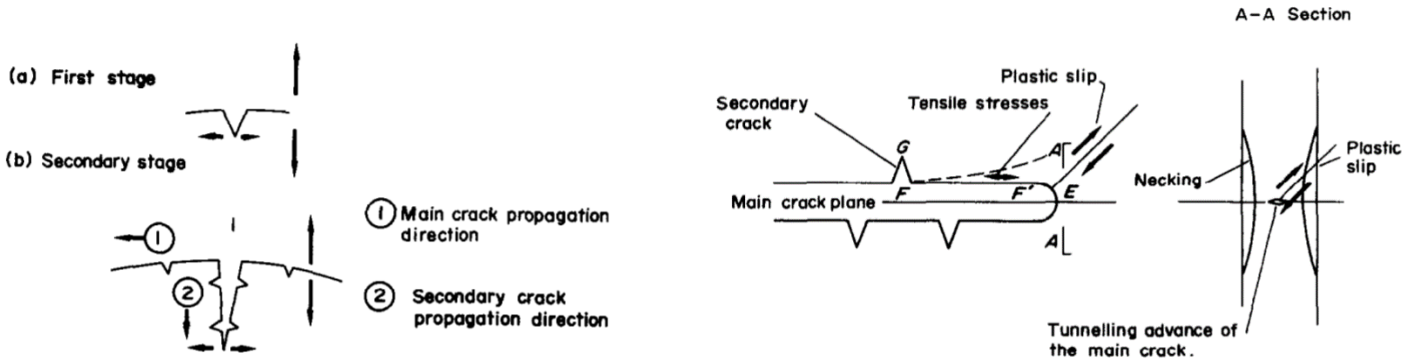

(a) *(b)*

FIGURE 24: Secondary crack nucleation (a) and explanation of secondary crack formation (b) [55].

Secondary cracks may form with a propagation direction perpendicular to the main crack propagation direction [52]. The occurrence of these cracks on the main crack propagation surface can be caused by the local elongation of the material due to tensile stresses parallel to the direction of propagation of the main crack, caused by plastic deformations and microstructure heterogeneity. This phenomenon can be observed in tensile specimens as well as fatigue samples. FIGURE 24 shows the mechanism that causes secondary cracks to form.

Sub-optimal energy densities will generate different types of porosities caused by gas entrapment, vaporization, keyholing, expulsion of metal in the weld pool or lack-of-fusion voids [53]. They take specific shapes and forms and are easily distinguished using SEM fractography. Gas entrapment pores are usually rounded while lack-of-fusion voids have jagged or irregular shapes. Gas entrapment is caused when rapid cooling of the material causes dissolved gases in the matrix to get trapped [39]. Lack-of-fusion voids, however, have been found to be larger and more detrimental to tensile and fatigue properties [54]. Keyholing is caused when excessive energy densities are used for the manufacture of components (see FIGURE 15 for optimal velocity and power com-

binations to avoid keyholing for L-PBF IN625) and generate porosities on the lower part of the melt pool. This is caused by the collapse of the keyhole when the molten material in the upper part moves downwards due to gravity and surface tension, which causes entrapment of gas [55].

Other features that can be observed in a fatigue fracture surface of hot rolled and annealed IN625 are shown in FIGURE 25. In this region, a beach marked surface can originate (FIGURE 25b and FIGURE 25c) which indicates stable crack growth. As the crack advances and the stress intensity range increases at the crack tip, the rate of the crack growth increases until the fracture toughness is reached, and fast fracture occurs.

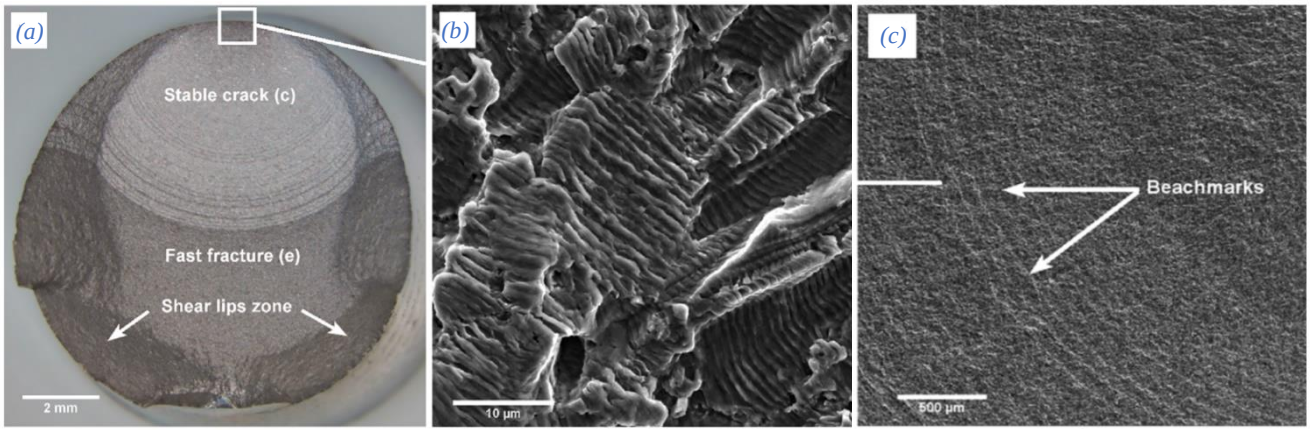

FIGURE 25: Fracture surface of HCF IN625 specimens fabricated by hot rolling and annealed at 910ºC for 2 hours. Beachmarks or striations show a stable crack formation.

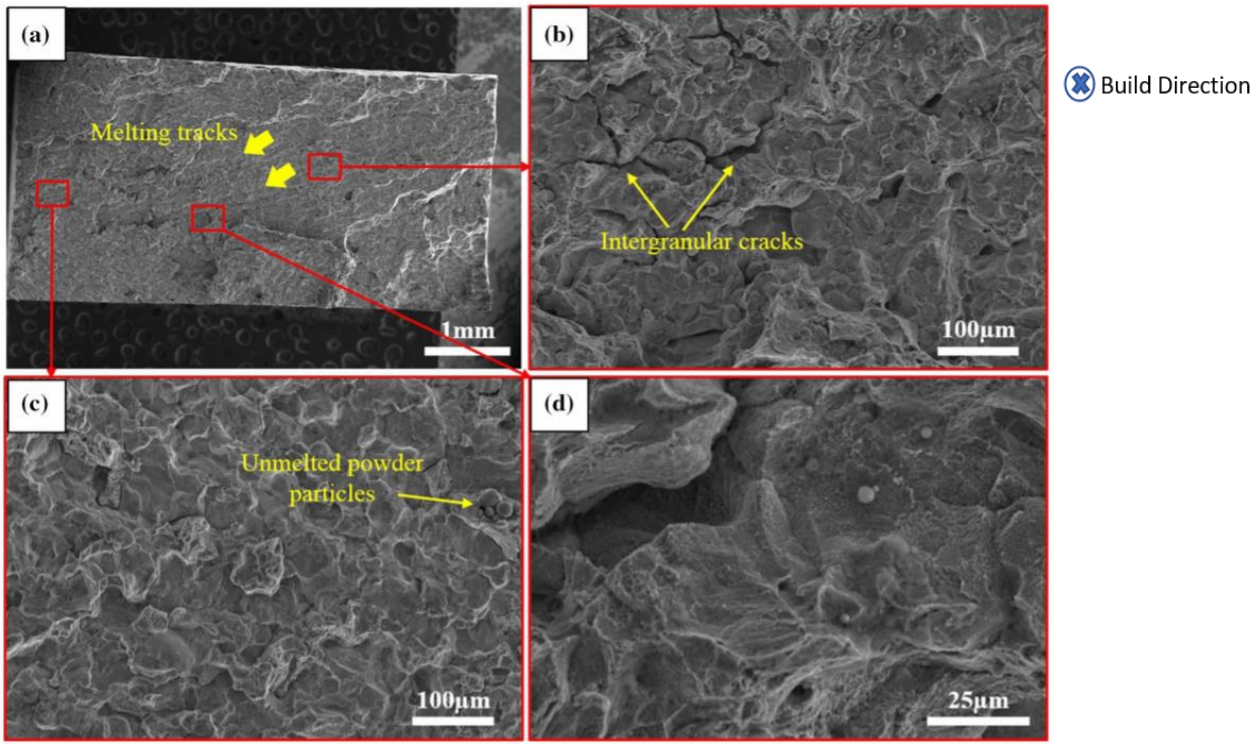

FIGURE 26: LCF specimens of high power L-PBF IN625 fabricated with 0.04 mm laser thickness, 0.1 mm spot size and 1kW of laser power. (b) (c) (d) show of lack-of-fusion defects, including unmelted powder and unfused particles [56].

3. MATERIALS AND METHODS

3.1. Design of the build plate

As shown in FIGURE 27, several mechanical test specimens, of different sizes and types, were built with axis either along the z-direction (build direction) or transverse to the z direction, denoted xy direction. The cylindrical dogbone specimens (25-32) correspond to the tensile specimens. The HCF specimens (1-24) include four types of flat dogbone specimens (small and large xy specimens, and small and large z specimens). Finally, the small cylindrical specimens (33-41), with diameter 10 mm and length 15 mm, correspond to the microstructure characterization specimens. The HCF testing and the characterization of the microstructure specimens were performed at the Georgia Institute of Technology while the tensile tests were conducted at Southwest Research Institute, San Antonio, TX.

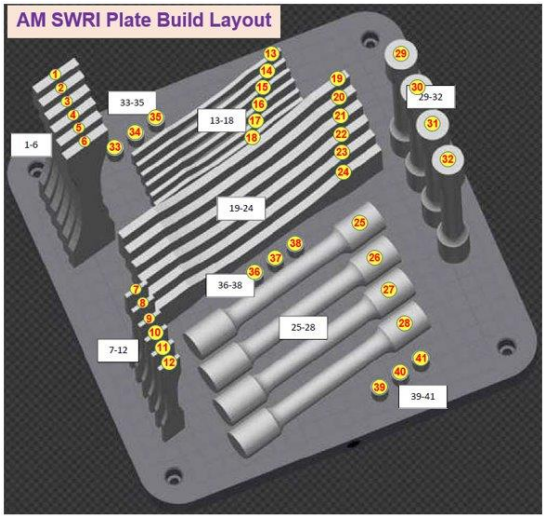

FIGURE 27: Build plate set up. Black dot represents front.

3.2. Geometry of the HCF specimens

In order to assess anisotropy on mechanical properties, the HCF specimens were built in the z and xy directions. To consider size effects, two different sized fatigue specimens were also considered. The geometry and dimensions of the small and large specimens is shown in FIGURE 28 and FIGURE 29.

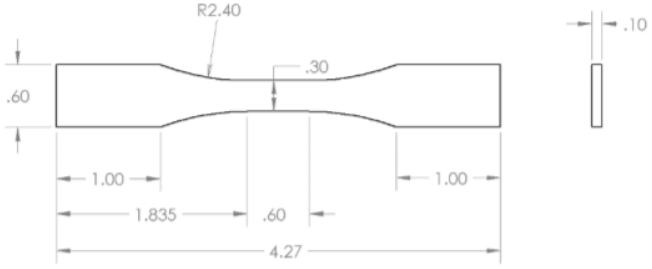

FIGURE 28: Nominal dimensions in inches of small fatigue specimens.

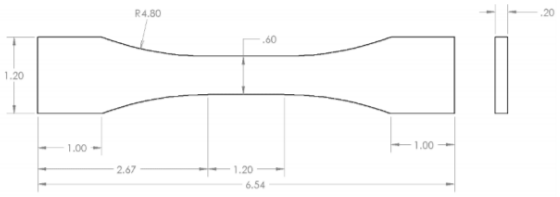

FIGURE 29: Nominal dimensions in inches of large fatigue specimens

3.3. Fixed and variable parameters for production of research specimens

3.3.1. AM systems

The AM systems used for the L-PBF process are the Concept M2 and the Renishaw AM250. The Concept M2 uses a 90 degrees rotation per layer, and each sample is lasered independently before moving on to the next. The Renishaw AM250 uses a pulsed laser as opposed to most of the systems. Furthermore, argon gas flows right to left on both machines while the wiper for the powder moves from right to left on the Concept M2 and back to front on the Renishaw AM250. The differences are summarized in TABLE 7.

TABLE 7: Differences in parameters and methodology.

	Concept M2	**Renishaw AM250**
Laser	Continuous	Discrete (pulsed)
Laser Spot Size	90 µm	70 µm
Wiper movement direction	Right to left	Back to front
Inert gas flow direction (Argon)	Right to left	Right to left

3.3.2. Powder

The powder used by both machines was manufactured using the gas atomization process, vacuum induction melt argon gas atomization.

TABLE 8: ASTM F3056-14 standards for IN625 powder composition [57].

Element	Ni	Cr	Mo	Nb	Fe	Mn	Co	P	Si	Ti	Al	S	C
Min (wt %)	remainder	20.0	8.0	3.15	-	-	-	-	-	-	-	-	-
Max (wt %)		23.0	10.0	4.15	5.0	0.5	1.0	0.015	0.5	0.4	0.4	0.015	0.1

TABLE 9: Composition of the powder used for all specimens.

Element	Ni	Cr	Mo	Nb+Ta	Nb	Fe	Co	Al	Ti	O	C
Wt %	63.2	22.2	9.0	3.8	3.8	0.69	0.44	0.33	0.24	0.016	0.01
Element	Cu	Mn	Si	Ta	V	Zr	P	N	S	B	
Wt %	<0.01	<0.01	<0.01	<0.01	<0.01	<0.01	<0.003	0.0019	0.001	<0.0009	

The powder composition has a low amount of C compared to ASTM F3056-14, which should be beneficial in limited the number of carbides in the microstructure. The powder used was spherical, and the size allowance ranged from 15 to 45 µm, with a mean diameter of 30 µm. TABLE 10 includes the parameters that were kept constant during the manufacture stage:

TABLE 10: Build Parameters kept constant.

Parameter	**Value**
Layer Thickness	40 µm
Laser Power	110 W
Substrate preheating	80 °C
Alternating laser path	90° (angle is set by Concept M2 machine that only supports 90° rotation)

The parameters in TABLE 11 and the scan pattern were varied across builds. The specific parameters varied for each build are stated in TABLE 12.

TABLE 11: Build parameters that were varied.

Parameter	**Value**
Laser speed	Varied between 800 mm/s and 900 mm/s with a center point of 850 mm/s
Hatch spacing	Varied between 70 and 100 µm with a center point of 85 µm
Heat treatments	Two different treatments were applied: 1. (SR + HIP): Industry standard stress relief cycle followed by HIPing (1121°C, 101.7 MPa, 4 hr). 2. (NSR + HIP): Alternative stress relief cycle (based on NIST recommendations to avoid delta-phase formation, 802°C/4 hr) followed by HIPing (1121°C, 101.7 MPa, 4 hr).

The complete design of experiments for the 11 builds is shown in TABLE 12. This study considered two L-PBF systems, with builds 1-6 fabricated on the Concept M2 and builds 7-11 fabricated on the Renishaw AM250.

3.3.3. Post-processing of L-PBF Parts

After the completion of the build in the L-PBF machine and before the specimens were removed, they underwent a stress relief (SR). Two different SR were included in the DoE. SR stands for standard stress relief, while NSR stands for the alternative NIST stress relief (see sections 2.4.2. and 2.4.4). After removal from the build plate by fatigue from breakout build supports, all specimens except for one microstructure specimen (designated BN-35) underwent hot isostatic pressing. The conditions for the heat treatments and HIP are stated in TABLE 11.

TABLE 12: Design of experiments.

Build No.	**Pattern**	**Velocity (mm/s)**	**Hatch spacing (µm)**	**Heat Treat Cycle**	**Machine**	**Energy Density (J/mm^3)**
1	---	800	70	SR+HIP	Concept M2	49.1
2	++-	900	100	SR+HIP	Concept M2	30.6
3	+-+	900	70	NSR+HIP	Concept M2	43.7
4	-++	800	100	NSR+HIP	Concept M2	34.4
5	Center Point	850	85	SR+HIP	Concept M2	38.1
6	++-	900	100	SR+HIP	Concept M2	30.6
7	+++	900	100	NSR+HIP	Renishaw AM250	30.6
8	-+-	800	100	SR+HIP	Renishaw AM250	34.4
9	Center Point	850	85	SR+HIP	Renishaw AM250	38.1
10	+--	900	70	SR+HIP	Renishaw AM250	43.7
11	--+	800	70	NSR+HIP	Renishaw AM250	49.1

3.4. Fatigue Testing Procedures

3.4.1. Pre-test preparations

To evaluate both the intrinsic fatigue properties of the material as well as the effects of the surface finish resulting from different builds, the testing regime was divided as follows: out of a batch of six z specimens (either small or large), one specimen was set aside for X-ray Computed Tomography (CT) analysis to later be tested, two specimens were polished on all sides of the gage section prior to testing, and three specimens were tested with as-is surface finishes. For xy specimens, the bottom edge of all specimens (i.e., the side closest to the build plate) was polished due to excessive roughness originating from the use of build supports. In addition to this, two specimens had their other narrow edge polished, and two specimens were tested in the fully polished state.

Prior to initializing tests, specimens underwent hardness testing in the grip section if they were the first of a build condition. The ratio of specimen hardness to the hardness of a sheet specimen was assumed to be similar to the ratios of fatigue strength to estimate the starting stress amplitude,

which was set at 80% of the stress value determined by this method. The hardness data was gathered using an AFFRI METALTESTER MKII. The specimens were laid flat on a thin sheet of packing foam on top of a table to prevent scratching, and hardness measurements were taken at four points on the grip sections; one point per grip face.

Polishing of the specimens was performed using a drill press and Dremel heads for narrow edges of the gage section, and an electric disk sander for wide faces. The sander operates at a constant speed and was fit with a 5" (127mm) disk attachment. The processes for polishing are described in TABLE 13 and TABLE 14.

TABLE 13: Polishing procedure for wide faces.

Step no.	Procedure
1	Initial thickness was recorded.
2	Disk sander was fitted with 180 grit SiC sandpaper, and water was applied. Sander was set to lowest speed at all stages of polishing. Sanding was done by placing sander face-up and holding sample with gentle to moderate force against sandpaper. Sample was moved in circular patterns regularly during sanding. The directions of these circular patterns were frequently against the direction of rotation of the sander, but both directions of rotation were used.
3	One face of specimen was polished until pits that originated from the surface were not present (viewed under stereoscope), and change in thickness was recorded. This was typically approximately 70 microns. Sandpaper was changed out as needed.
4	Steps 2 and 3 were repeated for opposing face.
5	Specimen was washed in water and acetone and blown dry, sandpaper was changed to 240 grit.
6	One face was polished until scratches from coarser grit are not apparent, change in thickness was recorded. As in step 3, it was ensured that residual marks from sanding were aligned in the direction of loading.
7	Step 6 was repeated for second face
8	Steps 5 through 7 were repeated using the following grits: 320, 500, 800, and 1200.
9	It was ensured that a total of no more than 200 microns of material were removed overall.

TABLE 14: Polishing procedure for narrow faces.

Step no.	Procedure
1	Initial width was recorded
2	A Dremel ½ in. sanding drum (part number 407) was fitted with 60 grit sandpaper and attached to drill press.
3	Specimen was moved back and forth continuously over sandpaper to ensure unbiased material removal on both gage and fillet sections of the specimen. It was held to the drum with light to moderate pressure, comparable to. Specimen was oriented such that residual marks were parallel to direction of loading.

TABLE 14 continued

4	Edge was polished using sanding drum fitted with 180 grit sandpaper until scratches from 60 grit paper were removed. The specimen was held against the drum with light to moderate pressure and moved continuously, as in step 3.
5	Edge was polished with 320, 500, 800, and 1200 grit sandpaper, sequentially, using method described in step 3
6	Above procedure was repeated for other edge if required.
7	Wide polished faces were repolished by hand as needed to remove any scratches from polishing the narrow edges procedure. Specimen was secured by hand and polished along loading direction with light pressure, as these scratches were generally very shallow.

FIGURE 30: Specimens ready to test. The specimen on the top followed the polishing procedure.

After polishing was completed, all specimens were fitted with rectangular G10/FR4 tabs covering both sides of both grip sections in order to prevent fretting fatigue failure in the wedge clamping grips, shown in FIGURE 30. The tabs were cut from sheets purchased from McMaster-Carr (part numbers were 8667K211 for small specimens and 8667K213 for large specimens), and had thicknesses of 1/16 in. (1.59 mm) and 1/8 in. (3.18 mm), respectively. Their nominal dimensions were 0.7 in. x 1.2 in. (17.78 mm x 30.48 mm) and 1.3 in. x 1.2 in. (33.02 mm x 30.48mm) for the small and large specimens, respectively. The tabs were cut via waterjet and were glued to the specimen using Instant-Bond Adhesive (McMaster-Carr part number 7729A23). Tabs were positioned on the specimen such that there was a 0.05 in. (1.27 mm) overhang on xy sides of the grip section and a 0.1 in. (2.54 mm) overhang on the z sides.

Prior to testing, surface roughness of the specimens was measured using the steps described in section 3.5.

Just before testing, the dimensions of the gage section of the specimens were measured using a caliper. The average of measurements taken at three points along the gage section (top, middle and bottom) was used to determine the cross-section area of each specimen. The widths of the small z specimens were all within 0.05 mm (0.002 in.) of the nominal dimension, and specimens were both over and undersized. The xy specimens had severely poor tolerances likely from the use of support material during the build. The thicknesses of all specimens were oversized but were within 0.10 mm (0.004 in.) of the nominal dimension. All specimens of a specific build condition were manufactured on a single substrate, with specimens being oriented and labeled as shown in FIGURE 27.

3.4.2. Test Frames

All tests were performed on uniaxial servohydraulic test systems. Several systems were used. These included MTS model 370 (rated to 250 kN) and Instron Satec TC-25 servohydraulic test frames fitted with MTS 647 hydraulic wedge grips. Machines were equipped with either TestStar IIs or Flextest40 controllers. The control software was either MTS Multipurpose Testware or MTS TestSuite Multipurpose Elite depending on machine used. Test processes were identical for both software packages. All grips were rotated and positioned to ensure that grips were parallel. Additionally, lower and upper fixtures like the one depicted in FIGURE 31 (lower grip fixture shown) were used to horizontally align the specimen. These were aligned by bolting them to the wedge grips and sliding them into place. The grips were moved to a fixed z offset such that specimens were leveled against both grips simultaneously, and then the bottom grip was closed. The frames were then set to maintain 0 N force, and the top grip was quickly secured as well. Grips were spaced apart such that they clamped between 0.9 in. and 1.0 in. of the grip section (not including FR4 tabs) ensuring that no pressure was applied to the fillet section. Grip pressure ranged from 2500 to 3000 psi, depending on the frame.

FIGURE 31: The fixture used to ensure fatigue specimens are horizontally aligned.

3.4.3. Fatigue Testing Parameters

All tests were conducted in force control with a stress ratio of

$$R = \frac{\sigma_{min}}{\sigma_{max}} = 0.1$$

and a frequency of 20 Hz, unless otherwise specified. Prior to testing, the frames were warmed up with dummy specimens and the PID control parameters of the frames were modified if needed. Tests were initialized by ramping the force to the mean value of the fatigue test over a period of 5 seconds. The force was then applied as a sinusoidal waveform, which was programmed

to stop after a fixed number of cycles (2 million for step tests, 10 million for standard fatigue tests). Force, displacement, and force error data were collected from each test as a circular buffer containing the most recent 1024 data points. If the measured force dropped below 100 N during the fatigue test (this force is low enough to imply specimen failure), a software interlock was tripped, halting the test.

3.4.4. Fatigue testing of rolled sheet

In addition to the AM specimens described in the previous sections, numerous specimens machined from a rolled IN625 sheet were tested to provide a reference value for fatigue strength. The sheet was manufactured by Special Metals via cold rolling. These specimens were cut from a single sheet, nominally 0.093 in. (2.36 mm) thick and 12 in. x 36 in. (304.80 mm x 914.4 mm) using a waterjet, and the gage and fillet sections were then machined via wire EDM. The wide faces of the specimens were polished as described TABLE 13 to remove scratches that were present on some of the specimens. The narrow edges of these specimens were not polished and left in the EDM condition. No systematic failure on the EDM edges was detected from the tests on the rolled IN625 sheet.

Before beginning testing of AM materials, a stress-life (SN) curve was developed for specimens machined from the rolled IN625 sheet. Tests were performed at stress amplitudes between 425 MPa and 250 MPa, with runout being defined at 10^7 cycles. The loading frequencies of the tests were 10 Hz at 425 MPa, 15 Hz at 375 MPa, and 20 Hz for all other stress amplitudes. Four specimens were also tested via the step test method to verify the suitability of the step test method for IN625. Data was fit via regression to both the Basquin equation:

$$\sigma_a = A(N_f)^a \qquad \text{[eq. 2]}$$

And the double power law:

$$\sigma_a = A(N_f)^a + B(N_f)^b \qquad \text{[eq. 3]}$$

3.4.5. The Step Test method

When assessing high cycle fatigue strength, the length and quantity of tests necessary can often limit the amount of data that can be gathered. An alternative method that can be used to determine the fatigue strength for a specified number of cycles is the step test, which has been described and validated by Bellows et al. [3]. Additionally, if it is assumed that the stress-life (SN) curve of the material being tested has a similar slope as a known SN curve, an SN curve of the material being tested can be estimated for use to estimate cycles to failure for finite life conditions.

The workflow of a step test is shown in FIGURE 33. All step tests were performed with a loading frequency of 20 Hz. After the first specimen of a set of specimens was tested and a fatigue strength measured, the starting stress amplitude of subsequent specimens of the same set was initialized at 90% of this value. If a step is completed, which occurs after running the test for 2 million cycles, then the stress range is increased by 5%, and the next step is initialized. If the specimen fails during the step, then the specimen's fatigue strength is calculated using the following equation:

$$\sigma_e = \sigma_{ps} + (\sigma_{fs} - \sigma_{ps}) \frac{N_f}{N_r} \qquad \text{[eq. 4]}$$

Here, σ_e is the fatigue strength (in terms of stress amplitude for a given R) of the material from known test parameters; σ_{ps} is the stress amplitude of the previous step, N_r is he cycles to the reference cycle, here set at 2x10^6 cycles, σ_{fs} is the stress amplitude being applied when failure occurred, and N_f cycles to failure in the step when failure occurred.

The loading parameters and outcome of the test are recorded for all steps. The face of the broken specimen in contact with the top front grip was marked with sharpie, and the approximate crack nucleation location was also recorded. Grip sections of broken specimens were secured to one another via rubber band with both fracture faces oriented in the same direction and stored in envelopes to protect the fracture surfaces for further characterization.

If the fatigue specimen fails during the first step, a different relationship is used to establish the fatigue strength. In this case, the number of minimum cycles for the data point to be valid was >10^5 cycles. The fatigue strength was estimated assuming that SN curves of AM materials have the same shape on a linear-log SN curve as that of the rolled sheet, but is shifted as illustrated in FIGURE 32. Using the double power law, the SN curve for first step failure specimens can be calculated assuming a linear shift in a linear-log scale or log scale:

$$\sigma_f = AN_f{}^a + BN_f{}^b + \Delta\sigma \qquad (1)$$

$$\sigma_e = AN_r{}^a + BN_r{}^b + \Delta\sigma \qquad (2)$$

where A, a, B, b are the double power law parameters obtained from the reference rolled sheet SN curve and N_r is the reference life set at 2x10^6 cycles. Solving for $\Delta\sigma$ in (1), substituting in (2) and simplifying, the following relationship is obtained:

$$\sigma_e = \sigma_f + A\left(N_r^a - N_f^a\right) + B\left(N_r^b - N_f^b\right) \quad \text{[eq. 5]}$$

In this equation σ_f and N_f are stress amplitude of the first step and cycles to failure, respectively.

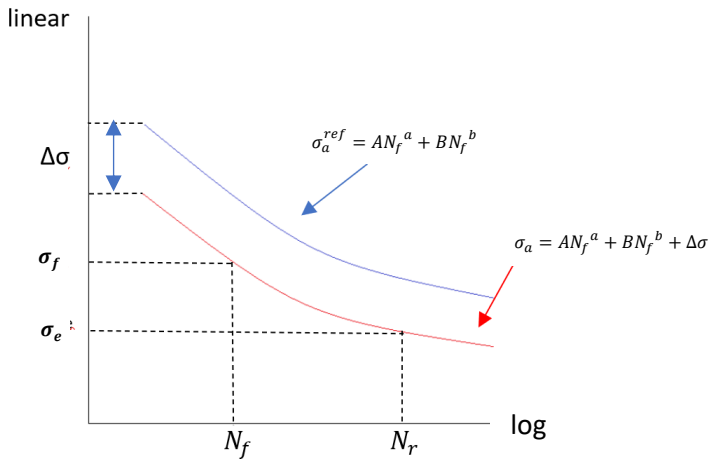

FIGURE 32: Linear-log shift to obtain fatigue strength for first step failures using reference rolled IN625.

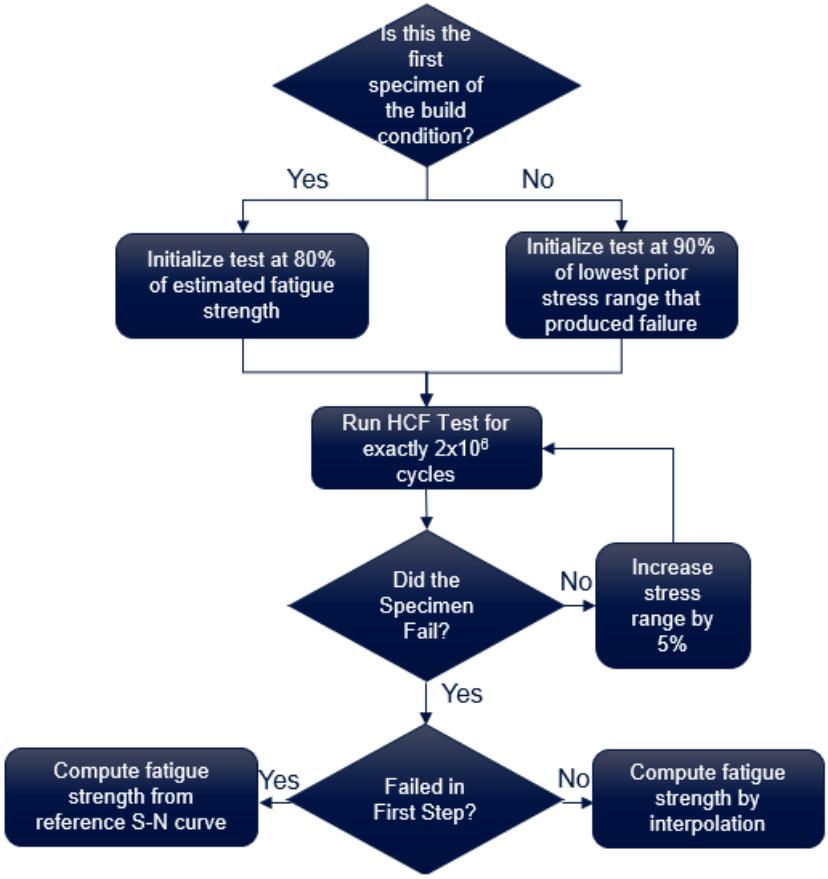

FIGURE 33: Process diagram for testing specimens using the step test method.

3.4.6. Fatigue life prediction methods

In order to develop design curves for stress ratios different from R = 0.1, four methods have been considered: Smith Watson Topper (SWT), Goodman, Gerber, and Walker. They relate fatigue strengths (stress amplitudes, σ_a), and their associated stress ratios $R = \frac{\sigma_{min}}{\sigma_{max}}$ to their equivalent fatigue strengths (stress amplitude, σ_{ar}) under fully-reversed loading.

3.4.7. Smith Watson Topper (SWT)

The SWT relationship is given by

$$\sigma_{ar} = \sqrt{\sigma_{\max}\, \sigma_a} \qquad \text{[eq. 6]}$$

The stress ratio $\sigma_{min} = R\, \sigma_{max}$ and the stress amplitude $\sigma_a = \frac{\sigma_{\max} - \sigma_{\min}}{2}$ can be used to obtain an equivalent relationship of SWT:

$$\sigma_{ar} = \sigma_a \sqrt{\frac{2}{(1-R)}} \qquad \text{[eq. 7]}$$

3.4.8. Goodman

Following a similar procedure, an alternate form of the Goodman equation can be obtained. The Goodman relationship takes the following form:

$$\frac{\sigma_a}{\sigma_{ar}} + \frac{\sigma_m}{\sigma_u} = 1 \qquad \text{[eq. 8]}$$

Combining the mean stress equation and the stress ratio $\sigma_m = \frac{(1+R)\,\sigma_{max}}{2}$ two alternate forms can be obtained:

$$\sigma_{ar} = \frac{\sigma_a}{1-\frac{\sigma_a}{\sigma_u}\left(\frac{1+R}{1-R}\right)} \qquad \text{[eq. 9]}$$

$$\sigma_{ar} = \frac{\sigma_a \sigma_u (1-R)}{\sigma_u(1-R) - \sigma_a(1+R)} \qquad \text{[eq. 10]}$$

3.4.9. Gerber

One of the earliest to be employed, the Gerber parabola takes the form:

$$\frac{\sigma_a}{\sigma_{ar}} + \left(\frac{\sigma_m}{\sigma_u}\right)^2 = 1 \qquad \text{[eq. 11]}$$

Rearranging the equation $\sigma_{ar} = \frac{\sigma_a}{1-\left(\frac{\sigma_m}{\sigma_u}\right)^2}$, using the relationship from the Goodman derivation and using the same methodology as in the previous relations, the following forms can be obtained:

$$\sigma_{ar} = \frac{\sigma_a}{1-\left(\frac{\sigma_a}{\sigma_u}\left(\frac{1+R}{1-R}\right)\right)^2} \qquad \text{[eq. 12]}$$

$$\sigma_{ar} = \frac{\sigma_a {\sigma_u}^2 (1-R)^2}{{\sigma_u}^2(1-R)^2 - {\sigma_a}^2(1+R)^2} \qquad \text{[eq. 13]}$$

3.4.10. Walker

The Walker Equation differs from the rest in that it uses a material constant γ that needs to be fit to a set of fatigue data tested at different stress ratios (R).

$$\sigma_{ar} = {\sigma_{max}}^{1-\gamma} {\sigma_a}^{\gamma} \qquad \text{[eq. 14]}$$

Rearranging the equation, $\sigma_{ar} = \left(\frac{2\sigma_a}{1-R}\right)^{1-\gamma} {\sigma_a}^{\gamma}$ two different forms can be obtained by rearranging:

$$\sigma_{ar} = \sigma_a \left(\frac{2}{1-R}\right)^{1-\gamma} \qquad \text{[eq. 15]}$$

$$\sigma_{ar} = \sigma_a \left(\frac{1-R}{2}\right)^{\gamma-1} \qquad \text{[eq. 16]}$$

When $\gamma = 0.5$, the Walker equation is equivalent to SWT. These equations serve two purposes: determine the equivalent fatigue strength σ_{ar} for fully-reversed loading and solve for σ_a to deter-

mine fatigue strength for any value of R if σ_{ar} is known. From the MMPDS data sheet, γ =0.42 for Inconel 625 correlated to fatigue life data with *R* ranging from -0.5 to 0.5 [58]. We assumed this exponent applied for fully-reversed loading too (R = -1) since no other data was available to establish a more refined value. For Goodman and Gerber, the ultimate tensile strength of the material σ_u was estimated based on the average ultimate tensile strengths measured in the tensile tests conducted on the additive manufactured specimens, removing all outliers that had reduced ductility resulting in a reduced ultimate tensile strength.

3.5. Roughness Measurements Methods

Roughness measurements were acquired using a Zygo Optical Profiler and analyzed using Zygo MX software. The measurement of interest was the Sa value, which is the average roughness value for the scanned area in µm. Another potentially relevant measurement is the Sv value, which is the maximum depth of the scanned surface. The measurements were taken for specimens in the as-is condition before the HCF testing. Measurements were taken on all four sides: wide towards back (of the build plate), wide to-wards front; narrow side 1 and narrow side 2 for z specimens; narrow side top and narrow side bottom for xy specimens. These sides were differentiated using a notation, which varied de-pending on the xy or z configurations:

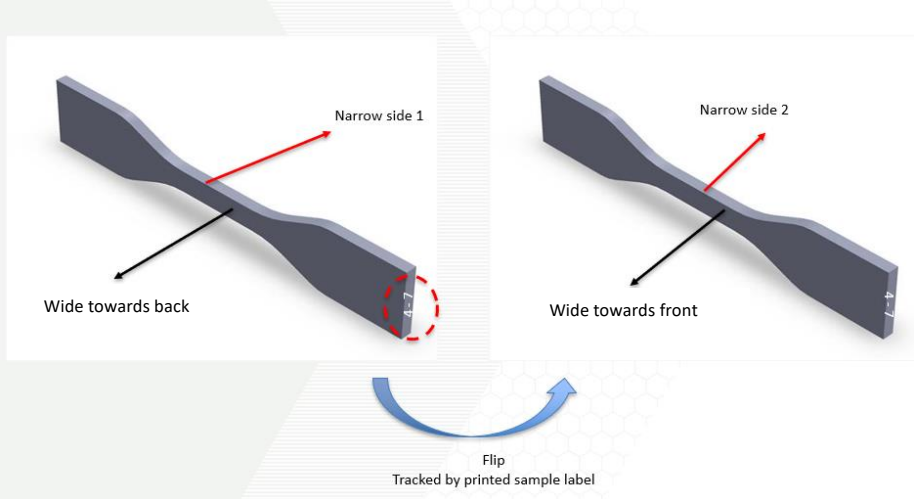

FIGURE 34: Side denotations for z specimens.

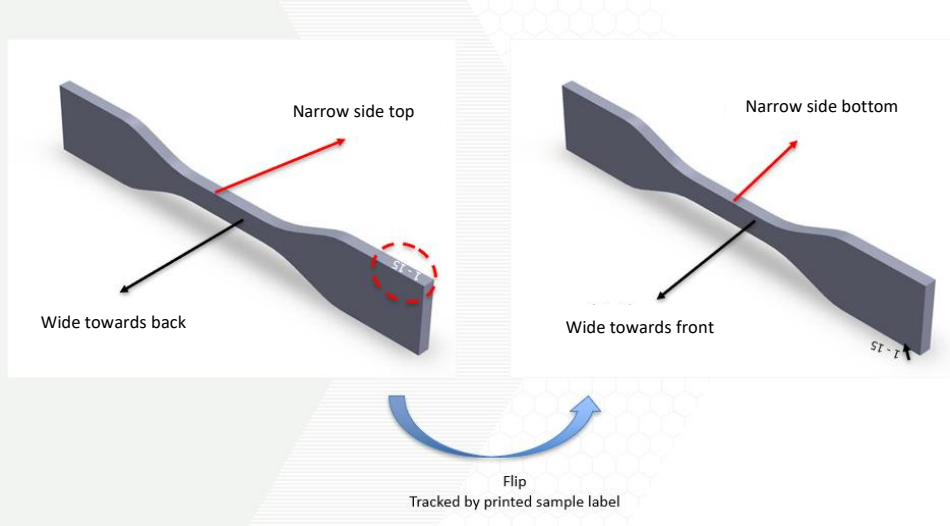

FIGURE *35*: Side denotations for xy specimens.

The workflow for scanning specimens is described in TABLE 15 for wide sides and TABLE 16.

TABLE 15: Procedure for roughness scans of wide sides.

Step no.	Procedure
1	All samples are previously mounted ahead of time with tabs on grips sections.
2	The specimen was fixated using standard tape on its flat side (see FIGURE 36a). Reference lines drawn in the stage were used to center specimens.
3	Find the center of specimen (longitudinal direction), and then find the point in left edge that corresponds to the height of the center of the specimen. Set the orgin of the stitch. Create a stich size that covers the entire width of the flat side 3x12 ($0.5mm^2$ per unit, with a total of 36 units). Set the new origin of the stitch in the scan unit noted as number three, and then reduce stitch size to 3x6 (0.5mm). This allows the final scan size to be centered in the flat side (FIGURE 36b).
4	Calculate scan width (lowest valley to highest peak) and begin scan from the highest point.

TABLE 16: Procedure for narrow sides.

Step no.	Procedure
1	The samples were taped on their side. The samples were equally centered using the reference lines in the platform.
2	Tape the stand-up sample with two grip ends. Closely tape the side, making sure there is no triangular space (there is no space between the tape and the specimen or the platform).
3	Use the clamps at both ends to ensure stability of the sample during the scanning. It will avoid rotation of the sample during the movements of the machine. The bottom of the clamp should rest evenly on the platform (FIGURE 38).

TABLE 16 continued

4	Find the center of the specimen, create a stitch size that covers the entire width 4x5 ($0.5mm^2$ per scan unit). Note that this scan size is slightly larger than the total width, so make sure that the scan area is centered to include all of the narrow side in the final output of the program.
5	Calculate scan width of the profile (lowest valley to highest peak) and start scan from highest point downwards.

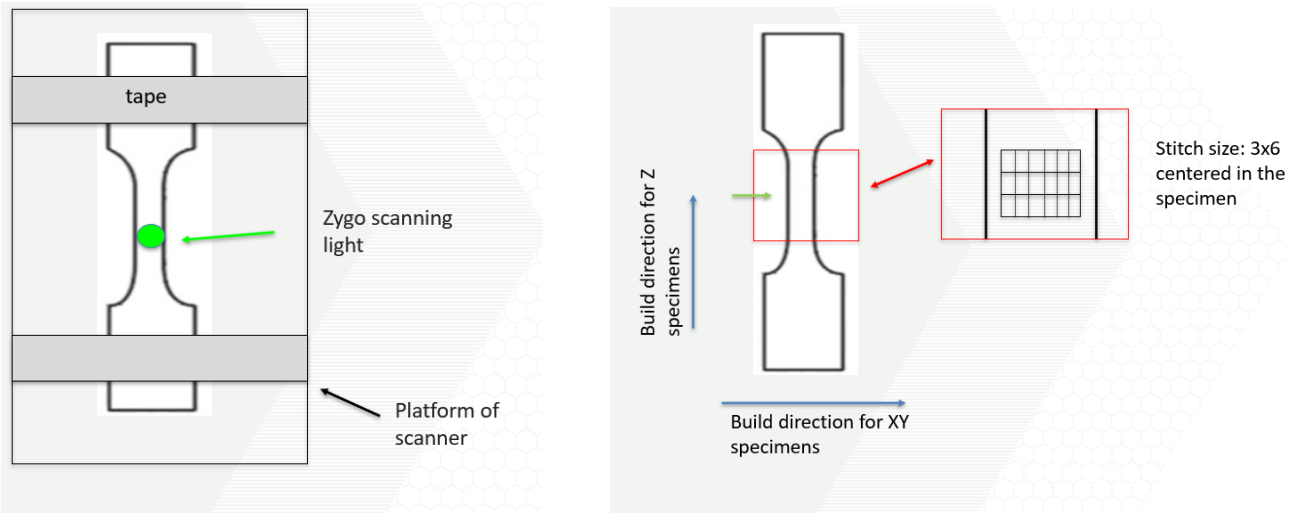

(a) *(b)*

FIGURE 36: Mounting (a) and scanning (b) of flat surfaces.

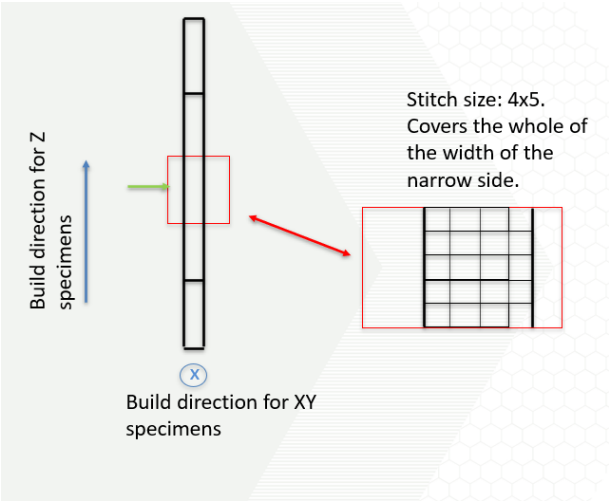

FIGURE 37: Mounting and scanning of narrow side surfaces.

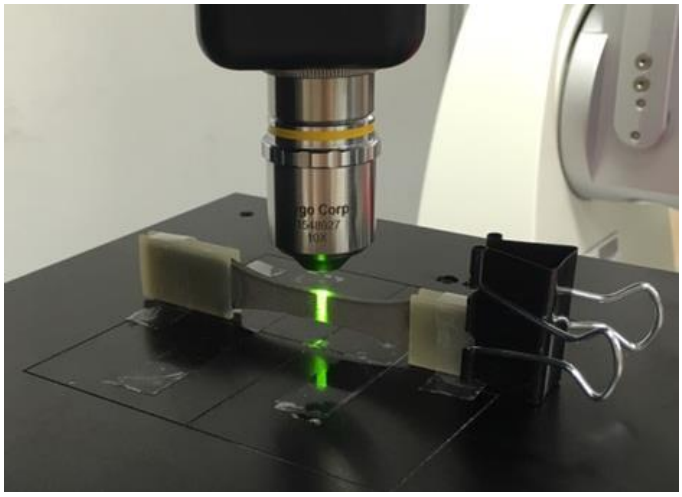

FIGURE 38: Scanning of the narrow edge of pre-test samples.

3.6. Porosity Measurements Methods

Each build included microstructure samples with the purpose of measuring porosity and characterizing the microstructure. These samples were mounted, polished using different grit paper, polished using the diamond polishing technique and imaged with an optical microscope.

3.6.1. Cutting

Each sample was cut longitudinally to divide into two equal parts, although the characterization was done for only one half.

3.6.2. Mounting

Both hot and cold mounting were used to create the microstructure samples. Hot mounts were 1 in. (25.4 mm) sized, and the cold mounts 1 ¼ in. (31.75 mm).

For the cold mounting, the process consisted in mixing hardener with a resin with a 1:4 ratio. The resin used was EpoxiCure 2 resin (20-3430-064) 3 (Buehler, Chicago, Il, Usa), while the hardener used was EpoxiCure 2 hardener (20-3432). A release agent was applied to extract the mounted samples from the cups once the curing was finished (48 hours to fully cure).

For hot mounting, the Techpress 3 (Allied, Los Angeles, CA) was used. Particularly, the mounting mode used for the samples was the conductive program with the following characteristics: 1-minute curing at 180C and 4408 PSI, and 4 minutes of cooling. The total time for the process is 5 minutes, making it more desirable than the cold mount if both resources are available.

3.6.3. Grinding

After mounting, the samples were grided using progressively finer grit paper. For grinding, the orbital sander Rotopol-15 (Struers, Copenhagen, Denmark) was used. Each batch of samples (3 samples at a time) was grinded at 250 rpm with running water (enough to lubricate the grind). It is important to note that the samples should be thoroughly cleaned between steps to avoid remains

scratching the sample in the next step. Pressurized air was used to dry each sample after cleaning. The griding steps are listed in TABLE 17.

TABLE 17: Steps for grinding microstructure specimens.

Step No.	Procedure
1	Sonicate for 5 minutes.
2	5N of applied force, 10 minutes at 250 rpm (500 grit paper).
3	5N of applied force, 10 minutes at 250 rpm (800 grit paper).
4	10N of applied force, 10 minutes at 250 rpm (2000 grit paper).

Every step the samples were checked to see uniformity in the scratches before moving on to next step.

3.6.4. Diamond polishing

Three different diamond polishing liquids were used to obtain a fully polished sample (9, 3,1 μm). The water flow was turned off and the diamond fluid was applied to the polisher each 1:30 minutes. After polishing with grit paper, TABLE 18 lists the steps performed.

TABLE 18: Diamond polishing steps for microstructure specimens.

Step No.	Procedure	Comments
1	5N of applied force, 10 minutes at 250 rpm with 9 μm diamond fluid.	This step can sometimes be problematic, as scratches can generate if the samples are not correctly cleaned or the exerted force has not been reduced from 10 to 5N. After this step the sample should look mirror polished to the naked eye but not to the microscope. If scratches remain, repeat this process until they have completely disappeared.
2	5N of applied force, 10 minutes at 250 rpm with 3 μm diamond fluid.	Check for uniformity of scratches with the microscope.
3	5N of applied force, 10 minutes at 250 rpm with 3 μm diamond fluid.	This step should completely eliminate any scratch, both seen by the naked eye and the microscope.

3.6.5. Imaging

An optical microscope was used to image the samples at 100x. The hardware was the Olympus BX-40 microscope, using the **Motic Images Plus 2.0 ML** software. Every image was taken with a 3664x2748 pixel resolution. For porosity imaging, 10 images were taken per sample following

the diagram in FIGURE 39. The sketch corresponds to the polished surface, and each blue square corresponds to each image taken from the samples and their order.

Before imaging, the polished faces were cleaned using running tap water and dried with compressed air. For unHIPed or porous samples, very thorough cleaning and drying had to be done, because dirt, water and polishing diamond liquid gets trapped within the pores and will show in the images. Moreover, any scratches present will also negatively affect the quality of the image, so if scratches are seen the last steps in TABLE 18 had to be repeated, depending on the width and amount of scratches.

Five small lines were drawn for reference on the lower edge of the polished face to aid with the microscope positioning (shown in green in FIGURE 39). The images were taken horizontally from the lines in a random manner. Before imaging,

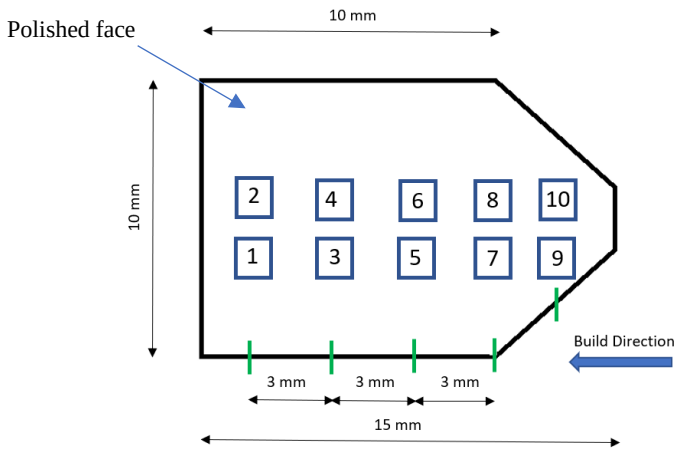

FIGURE 39: Schematic of the distribution of the images taken.

4. RESULTS AND DISCUSSION

4.1. High cycle fatigue data

4.1.1. High cycle fatigue results of IN625 rolled sheet

The first step taken was to benchmark the fatigue data by generating a "reference curve" using specimens machined from an IN625 rolled sheet (2.36 mm thick). The tensile properties of the reference rolled sheet were the following: Elastic Modulus was 190 MPa, the 0.2% offset yield strength was 550 MPa, and the UTS was 958 MPa. The complete tensile curves are shown in the Appendix. The hardness measured converted to Rockwell scales were 72 HRA, 113 HRB and 41 HRC. Macroscopic imaging of the fractured tensile specimens revealed ductile failures, as shear lips could be observed in most of the fracture surfaces. The SN curve of the Inconel 625 rolled sheet is shown in FIGURE 40, where the double power law fit (Eq. 3) the data better than a simple Basquin curve (Eq. 2). The data used was acquired as described in section 3.4.4, although the step tests are also included. The double power law coefficients were: A = 31,420 MPa/cycles, a = -0.485, B = 217 MPa, and b = 0. These were obtained by numerical minimization of the SSE (sum of squared errors) of the curve with a constraint that exponents must be nonpositive. The SSE of the double power law was 1148 MPa^2. The double power law relation with these parameters represented the reference curve behavior. It is valid for cycles to failure between 5 x 10^4 to 10^7.

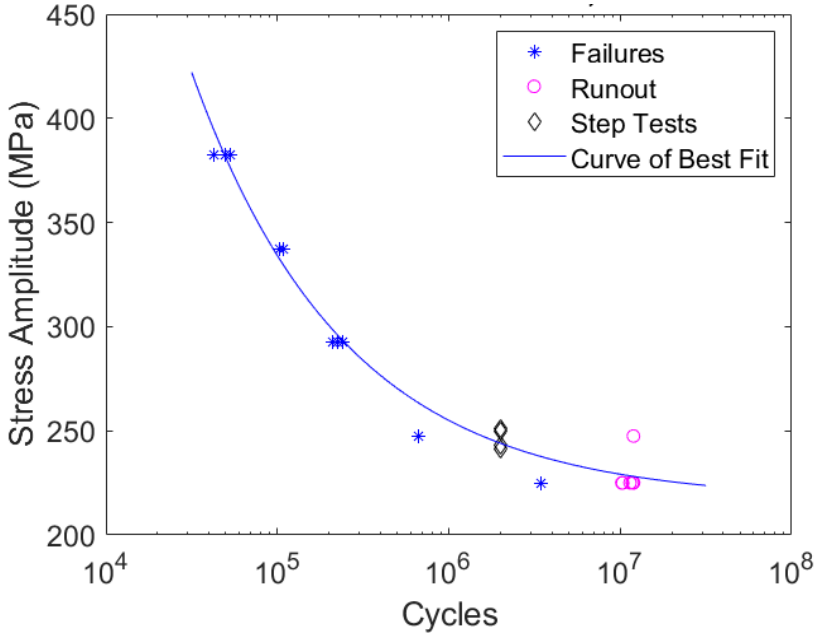

FIGURE 40: Double power law curve fit to SN data of Alloy 625 sheet test at R = 0.1.

This work focuses on the small xy and z specimens. Due to the COVID-19 outbreak, these specimens were prioritized over the large specimens in order to give a comprehensive overview of all 11 builds. Some large z specimens were tested, but not enough data was gathered to obtain meaningful conclusions and trends. The following SN curves represent the data for the different builds and are separated according to the testing conditions: polished or as-is. The graphs include the rolled IN 625 plate a reference curve in black and the rest of the builds are color-coded accordingly. First step failures with a step count greater than 100,000 were considered valid to obtain a good estimate of the curve. The validity of the double power law fit for first step failures can be observed

in the different SN curves, as the data points resulting from first step failure do not deviate from their SN curves more than other step test points. Each data point represents one fatigue test specimen. The points aligned with $2x10^6$ cycles are the fatigue strengths obtained using the step-test procedure. Any data points shown plotted as failed at less than $2x10^6$ cycles, fractured during the first step.

4.1.2. High cycle fatigue results of additively manufactured IN625

FIGURE 41 shows the fatigue strength at 2 million cycles for small z specimens, comparing the fatigue strengths for the 11 builds tested in both as-is and polished conditions. The variation bars represent the range in fatigue strengths measured from multiple specimens. In nearly all builds, the polished specimens had higher fatigue strength, especially prevalent in the higher fatigue strength cases. There is a high variability in the strengths of the specimens across builds. It can be observed from the plots that builds 1-3 and 9-11 performed much better than the rest. In fact, builds 3 and 11 in the polished conditions had very similar fatigue strengths to the rolled IN625 plate. This is explained by the difference in microstructure and presence of defects in the fracture surface shown later. It is worth highlighting that the expected strength of the as-is small z specimens for build 11 was higher than the obtained data. This is due to a large porosity defect found on the surface of one of the specimens (11-10), and due to lower number of tested specimens (2 units), the average strength is considerably penalized. Overall, the step test method was successful at measuring fatigue lives, with the exception of specimens from build 7 which had very low performance due to extreme lack-of-fusion porosity.

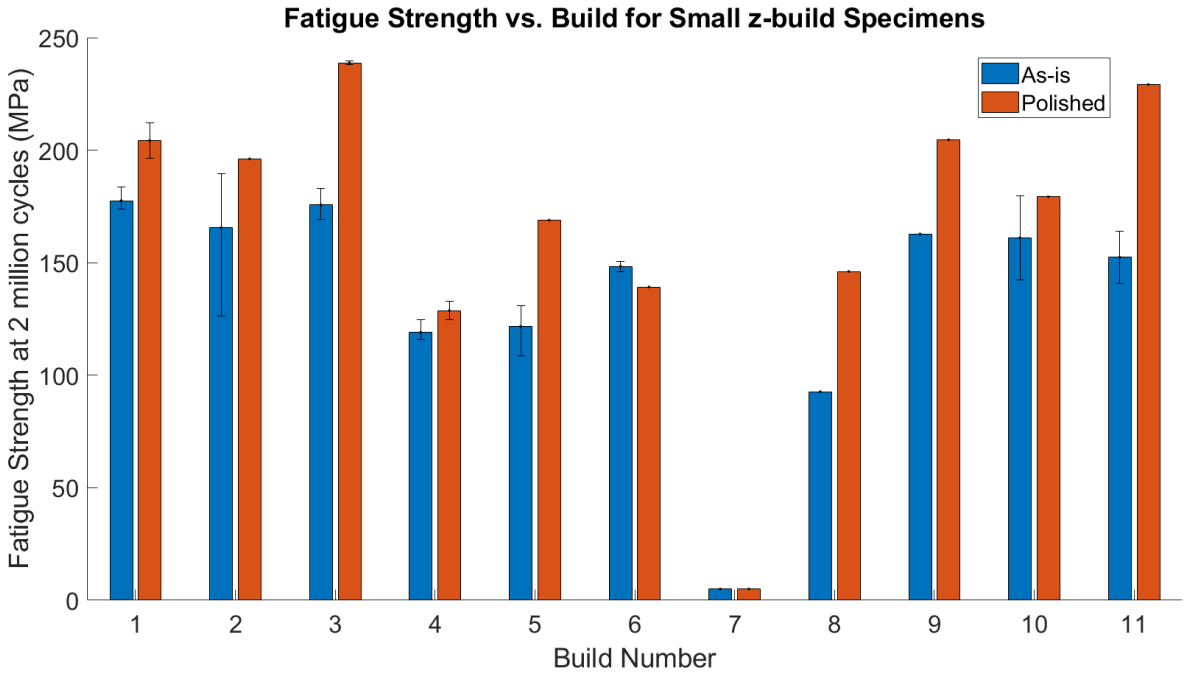

FIGURE 41: Fatigue strengths for the small z specimens in the as-is and polished condition. (R=0.1)

FIGURE 42 compares the fatigue strengths of the small z and xy specimens tested in the as-is condition. For the Concept M2 builds (1-6), a significant difference of fatigue strengths was found between the two orientations, especially for the cases with good fatigue strength properties in the z-direction. This is consistent with the notion that cases where there is larger amount of porosity,

the difference becomes lower or almost negligible because the fatigue crack formation is completely governed by porosity defects and not surface roughness features. An interesting insight from this plot is that there is a larger anisotropy in fatigue strengths between z and xy specimens for the Renishaw AM250 than the Concept M2 machine, with the exception of build 11. However, as stated earlier, the strength of the small z as-is specimens is expected to rise as additional specimens are tested.

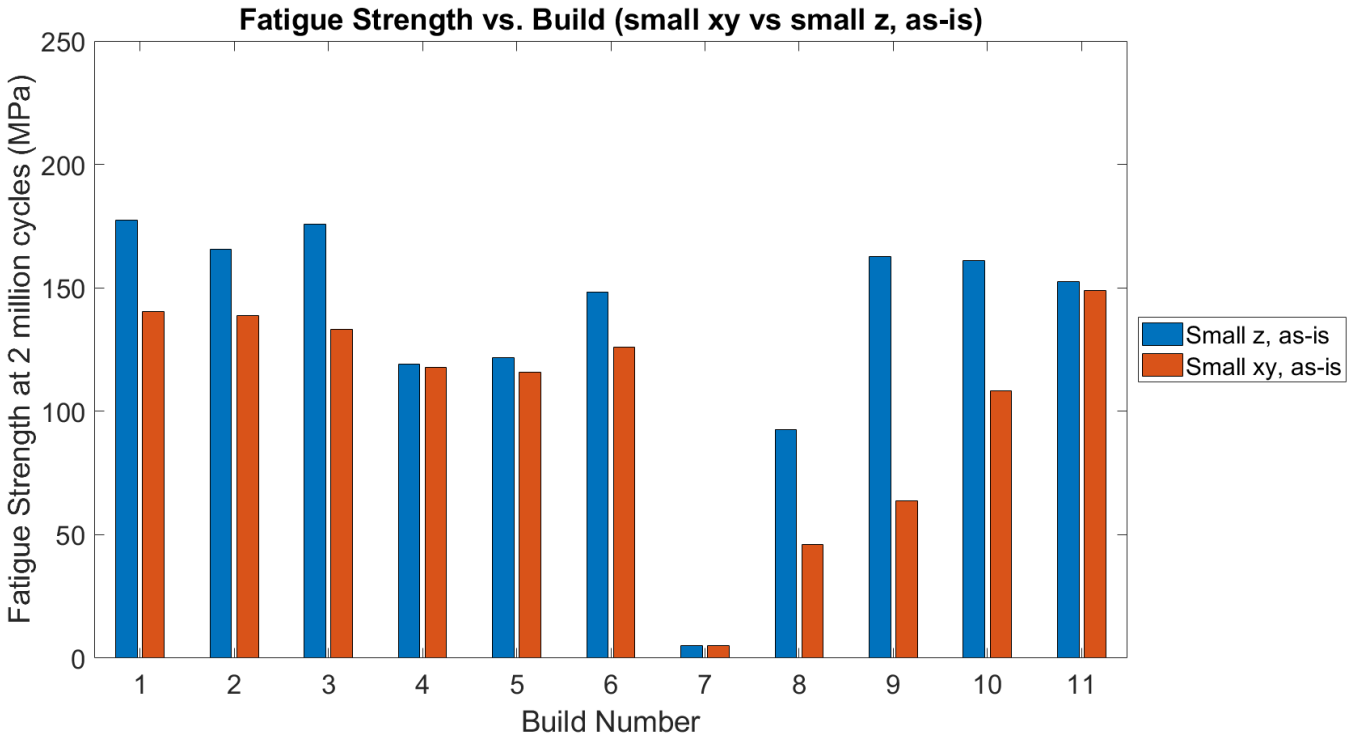

FIGURE 42: Fatigue strength for small xy and z specimens tested in the as-is condition. (R=0.1)

FIGURE 43, FIGURE 44 and FIGURE 45 show the projected SN curves for the small z and xy specimens in polished and as-is conditions according to the build. Actual data points from experiments are denoted by a symbol. If the specimen made it to more than 1 step, the strength at $2x10^6$ was calculated and plotted. Data points that do not plot at $2x10^6$ cycles are first step failures and indicate the number of cycles the specimen endured at the applied stress level.

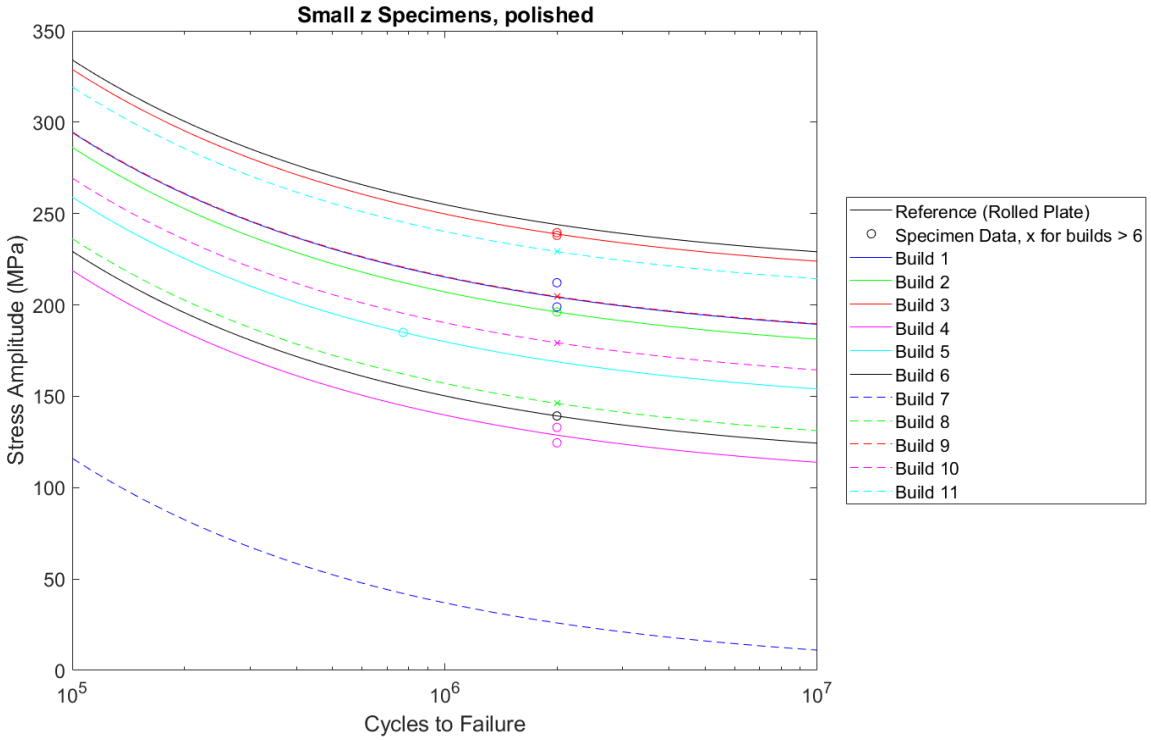

FIGURE 43: SN curve for the small z specimens in polished condition. (R=0.1)

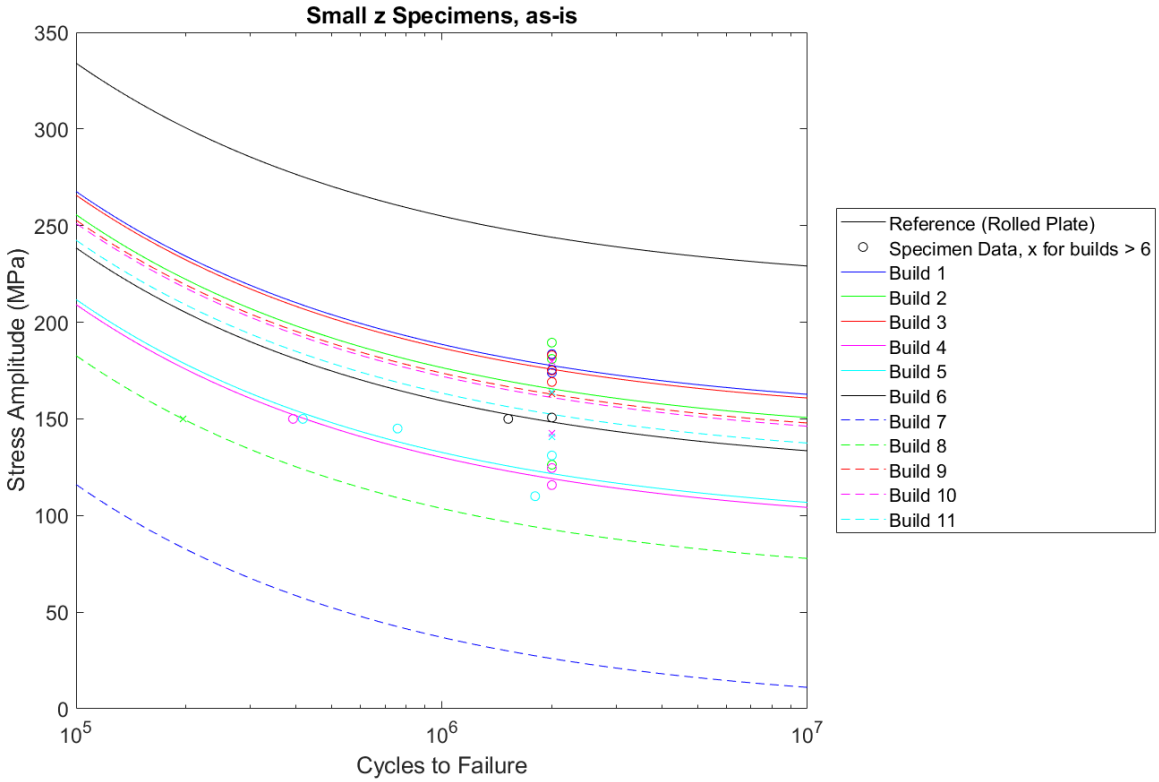

FIGURE 44: SN curve for the small z specimens in as-is condition. (R=0.1)

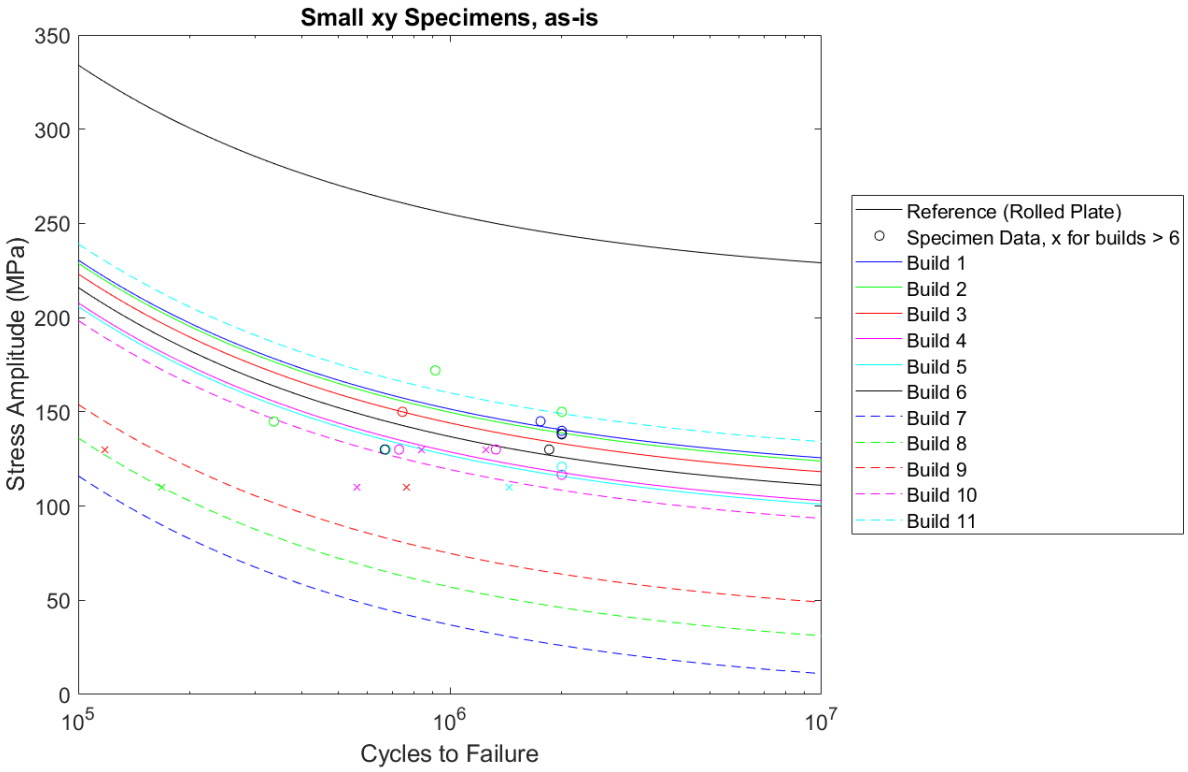

FIGURE 45: SN curve for the small xy specimens in the as-is condition. (R=0.1)

4.2. Comparison of fatigue strength to tensile properties

Tensile tests were performed on both z and xy specimens. These tests were conducted by Southwest Research Institute, San Antonio, TX. There were 8 tensile specimens per build (see FIGURE 27), 4 xy and 4 z. All tensile specimens were tested in a machined condition to eliminate the influence of surface roughness. Some specimens could not be tested because they were either too warped to be machined or had fractured during the build. These issues were more prominent for xy specimens than z specimens, making z tensile results more reliable. The full stress-strain curves are given in the Appendix. The test results are summarized for builds 1 through 11 and separated according to the build direction. For as-is specimens and for every build direction, all four mechanical properties are plotted against build number.

4.2.1. z tensile properties

A comparison of the elastic modulus (E), yield strength (YS), and ultimate tensitle strength (UTS) in the z direction is shown in FIGURE 46, FIGURE 47, and FIGURE 48, respectively. A low variability in these properties was observed across builds for the same machine. In fact, the values are invariant for those builds by the same machine even with variations in the AM process parameters. The YS and UTS of the specimens fabricated on the Concept M2 were significantly higher than on the Renishaw.

In contrast, the strain to failure exhibited a high variability across builds (FIGURE 49), very similar to the variability seen in the HCF results. Builds with less than 25% strain to failure experienced consistently poor fatigue strength while those with over 25% strain to failure had much higher fatigue strengths. In fact, a clear correlation can be seen between strain to failure and fatigue strength (FIGURE 53). The trend seems to be good with the exception of build 4 which presented a very good ductility compared to its HCF strength.

Overall, no apparent correlation between the previous mentioned mechanical properties (E, YS and UTS) and HCF strength of small z as-is specimens was found (FIGURES 50-52). This is a relevant observation, as previous studies [39] have found correlations between yield strength and fatigue, proving that it does not necessarily have to be the case for HCF.

4.2.2. xy tensile properties

The xy specimens exhibited considerably more variability in properties, particularly in strength and ductility. The elastic modulus (FIGURE 54) maintains the low variability observed previously with z specimens but the strength and ductility show different findings. As a result, no correlation has been found between the strain to failure and HCF strength for this xy specimen group. However, the yield strength does positively correlate with fatigue (FIGURE 59), with the exception of build 11 that presented a higher fatigue strength compared to the tensile test result. There is also a weak positive correlation between the ultimate tensile strength and fatigue with the exception of build 10 (FIGURE 60). However, these results are not as reliable for xy samples as these outliers could be due to low number of xy tensile specimens tested for build 10 and 11 (one specimen for build 10, two specimens for build 11). This suggests that the tensile strength is controlled by the post-build treatments, which was expected before designing the DoE.

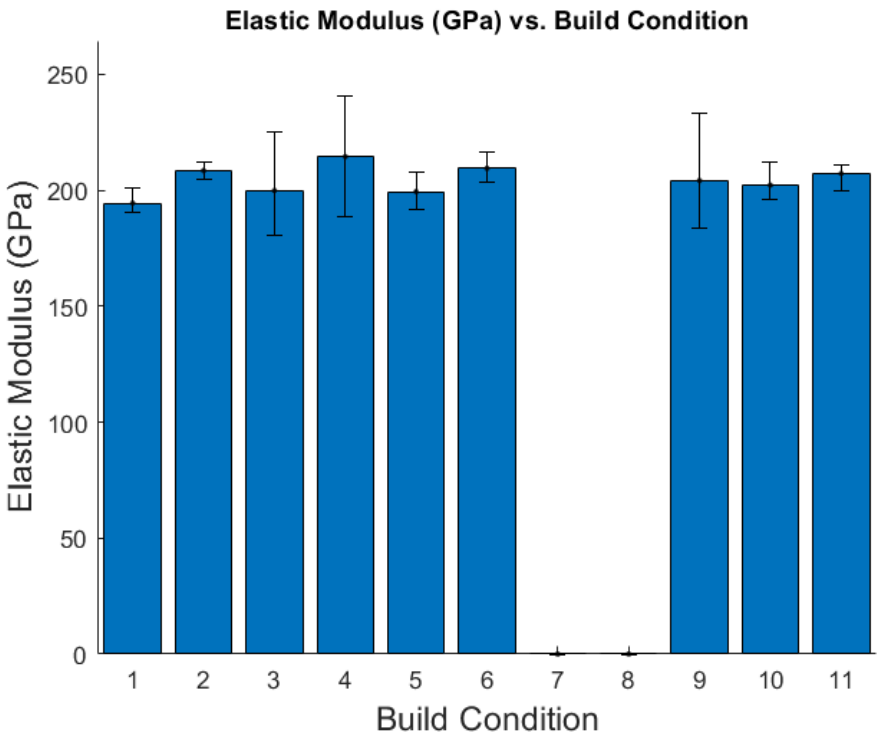

FIGURE 46: Elastic modulus for the z tensile specimens.

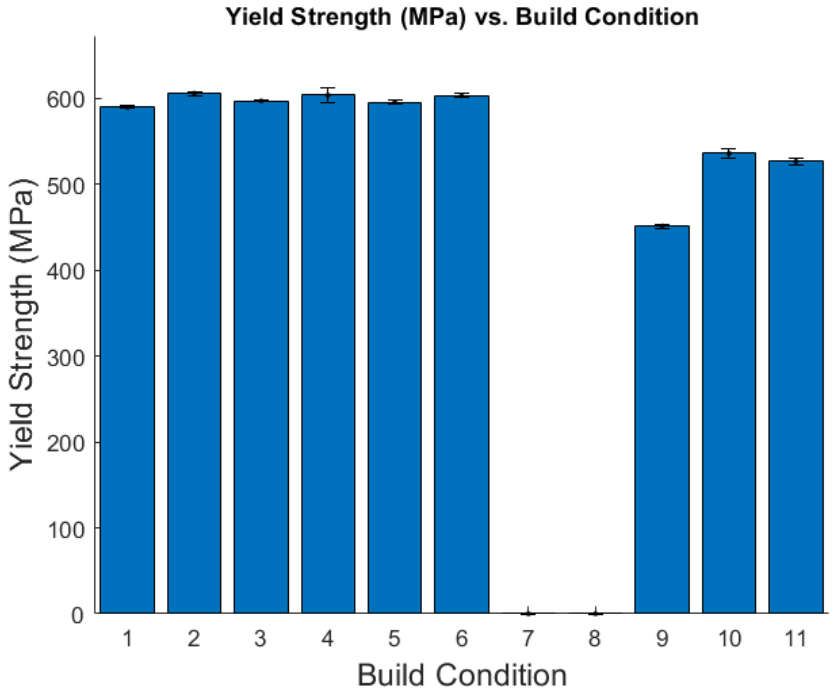

FIGURE 47: Yield strength for the z tensile specimens.

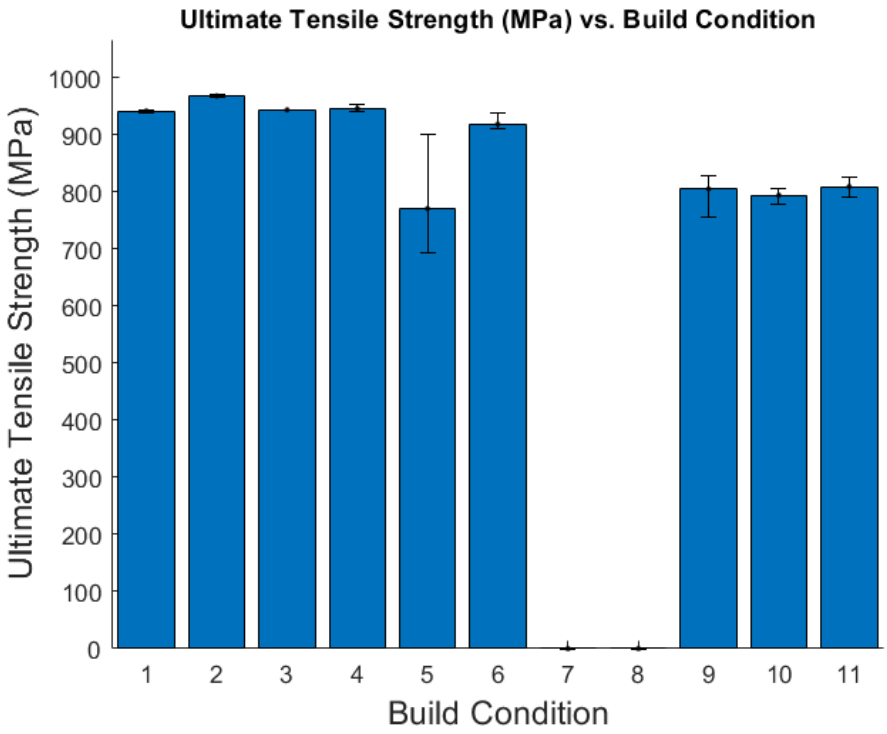

FIGURE 48: Ultimate tensile strength for the z tensile specimens.

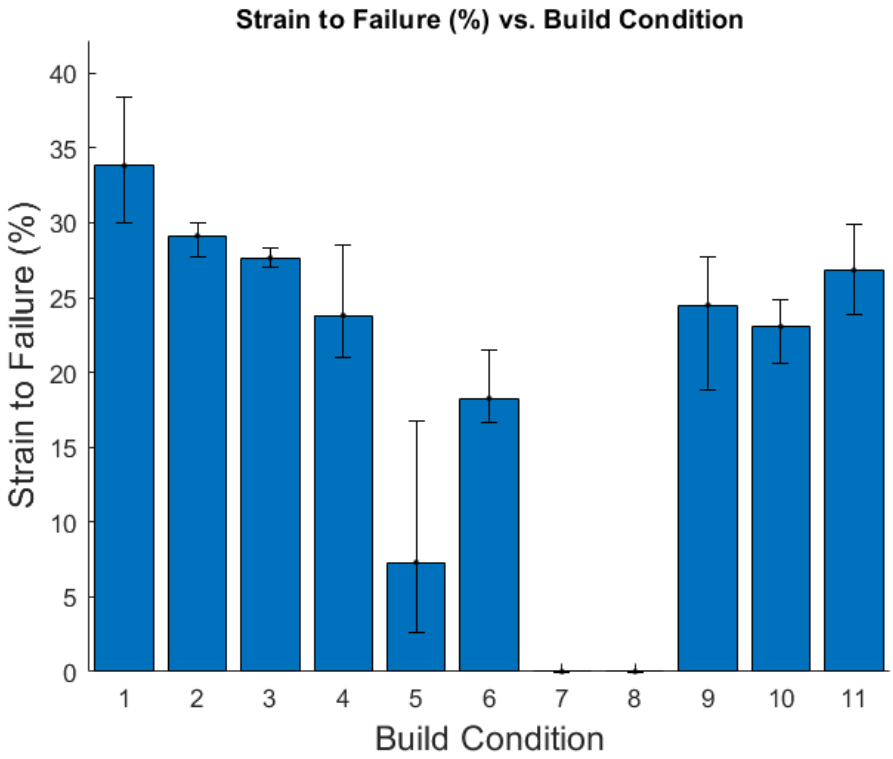

FIGURE 49: Strain to failure for the z tensile specimens.

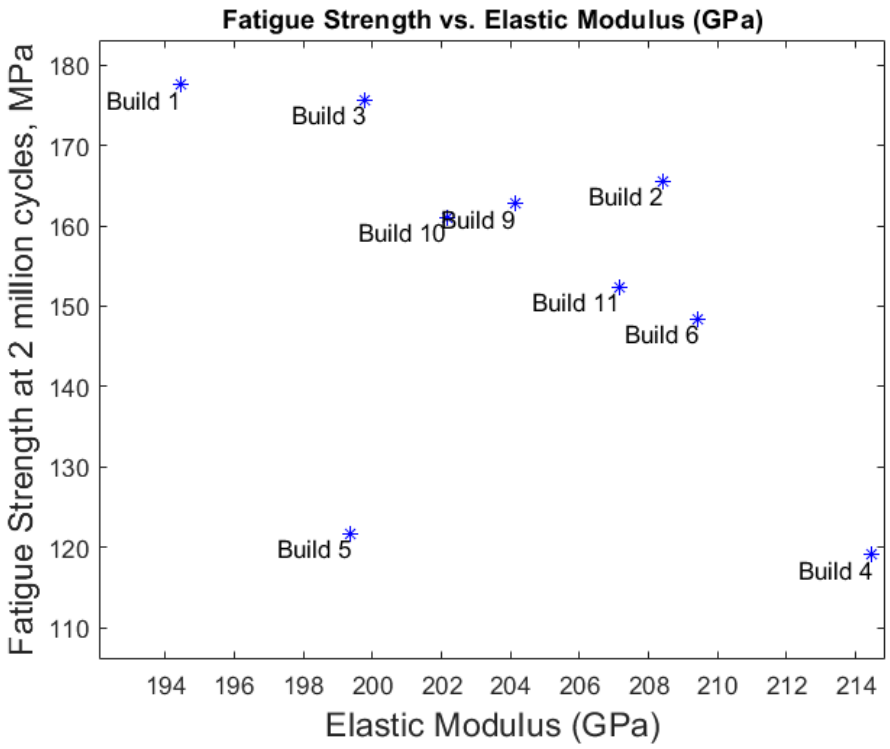

FIGURE 50: Fatigue strength (small z, as-is) vs. elastic modulus for z specimens.

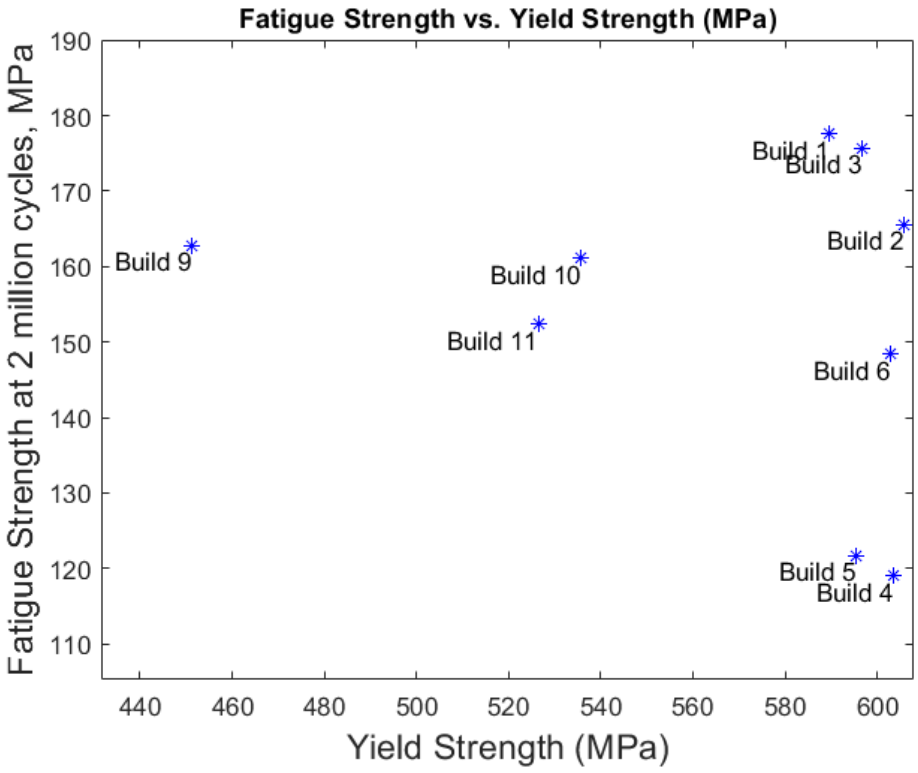

FIGURE 51: Fatigue strength (small z, as-is) vs. yield strength for z specimens.

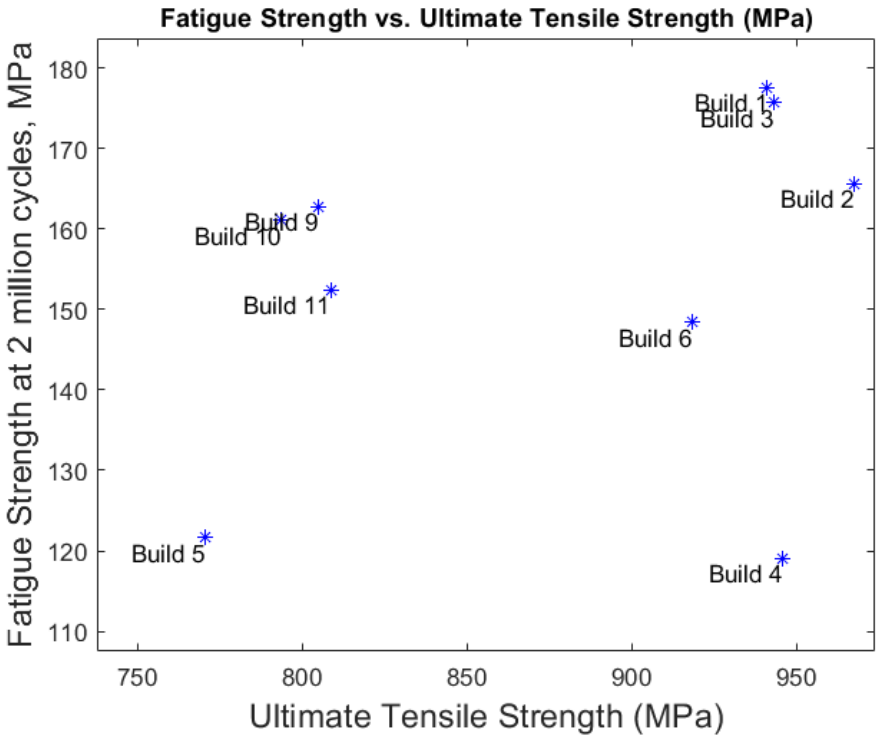

FIGURE 52: Fatigue strength (small z, as-is) vs. ultimate tensile strength for z specimens.

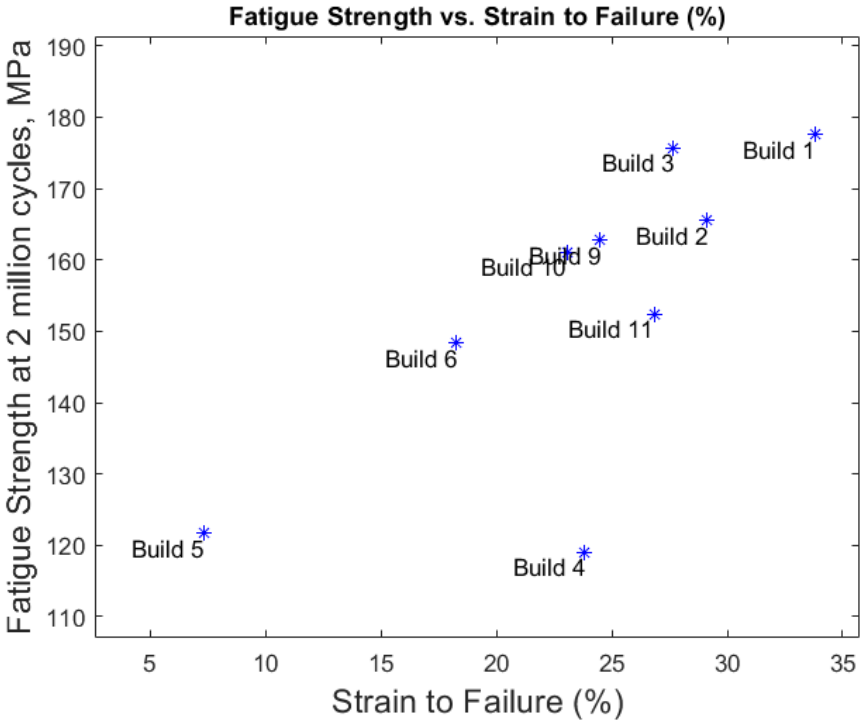

FIGURE 53: Fatigue strength (small z, as-is) vs. strain to failure for z specimens.

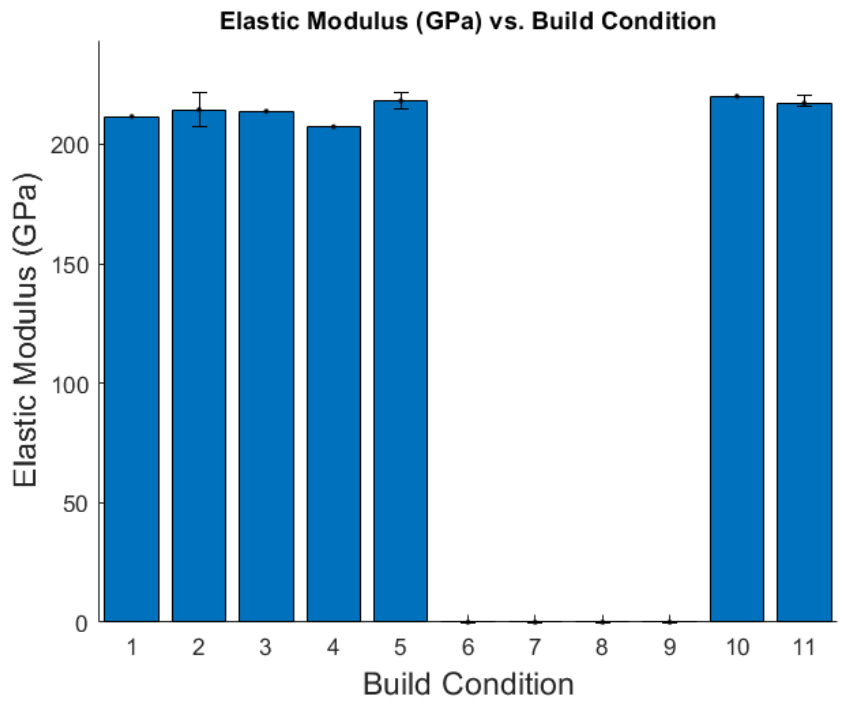

FIGURE 54: Elastic modulus vs. build condition for xy tensile specimens.

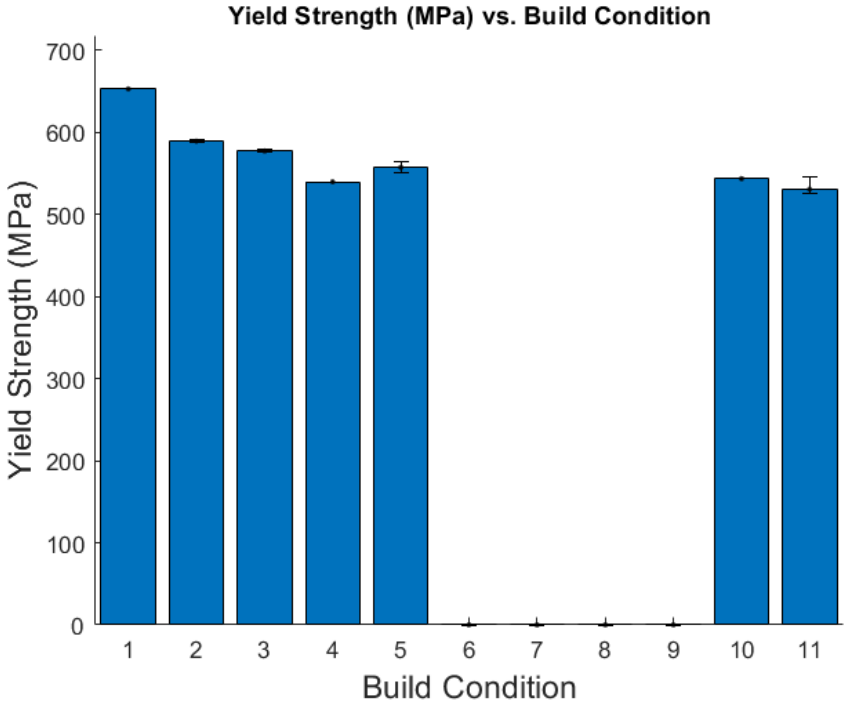

FIGURE 55: Yield strength vs. build condition for xy tensile specimens.

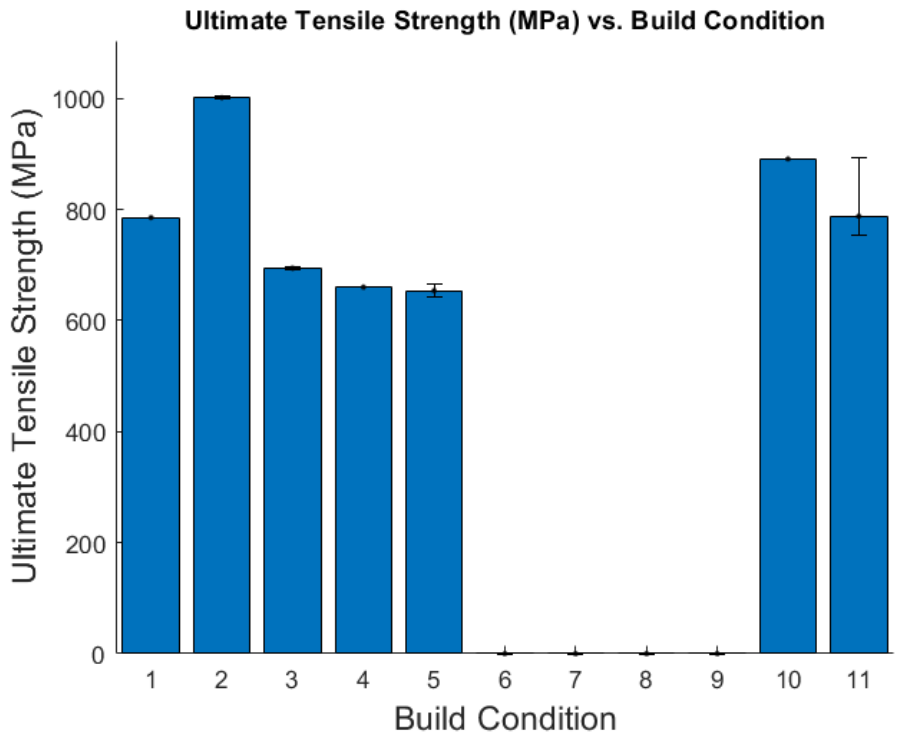

FIGURE 56: Ultimate tensile strength vs. build condition for xy tensile specimens.

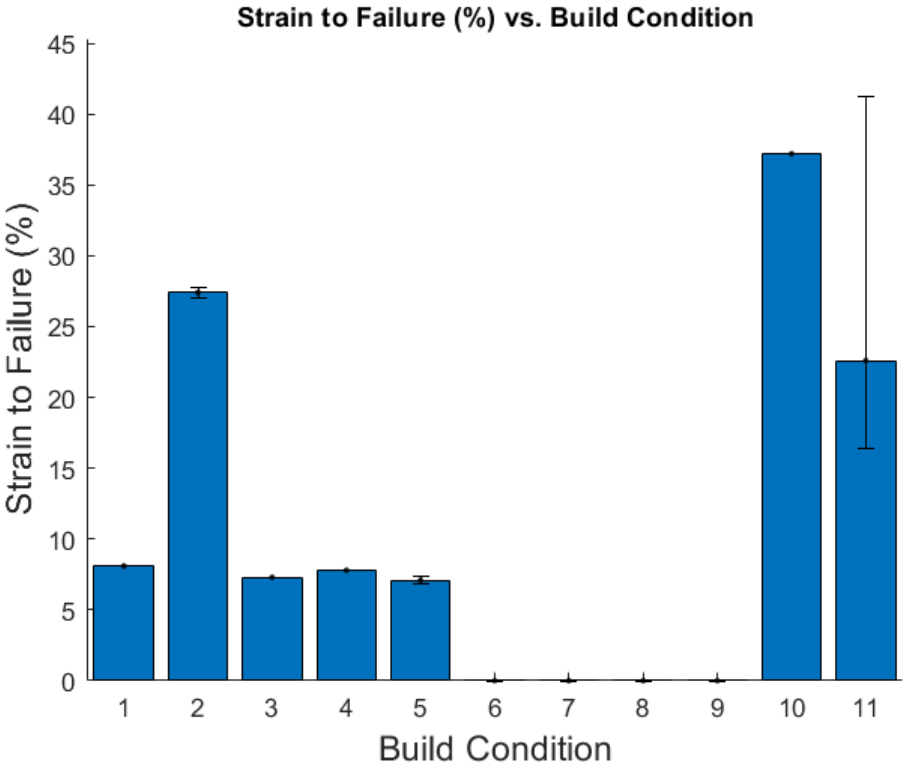

FIGURE 57: Strain to failure vs. build condition for xy tensile specimens.

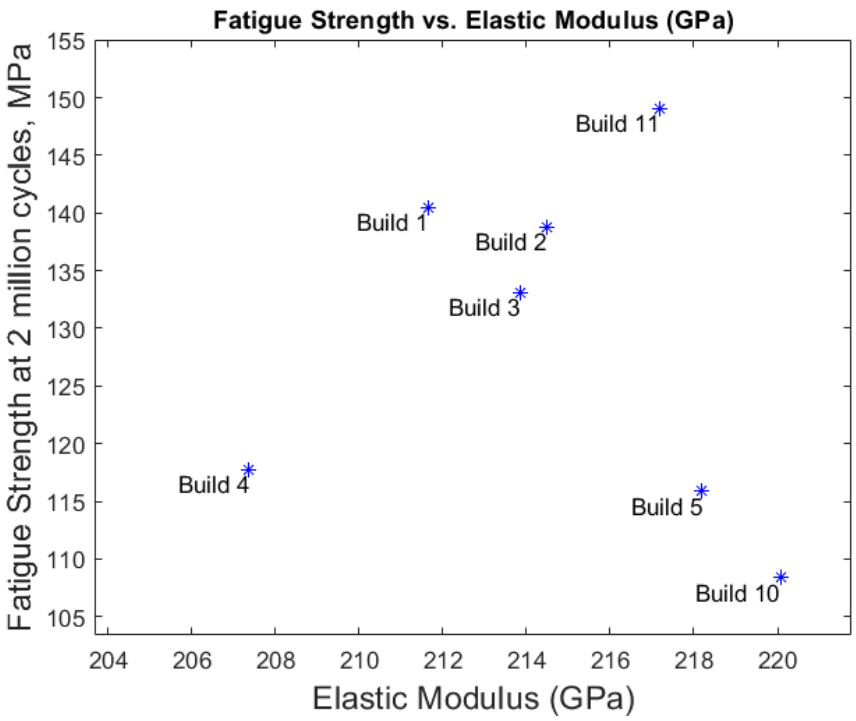

FIGURE 58: Fatigue strength (small xy, as-is) vs. elastic modulus for xy specimens.

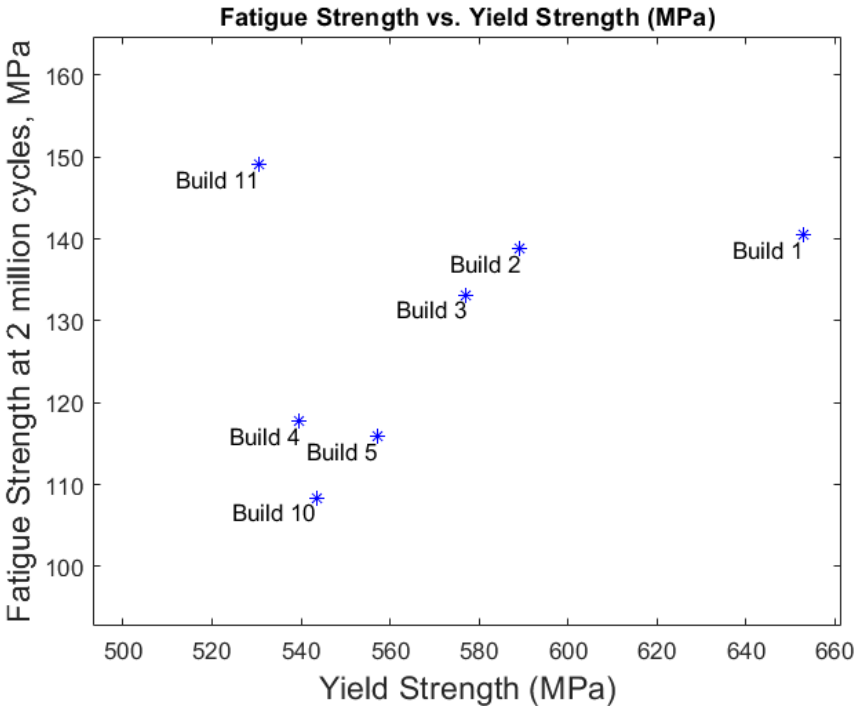

FIGURE 59: Fatigue strength (small xy, as-is) vs. yield strength for xy specimens.

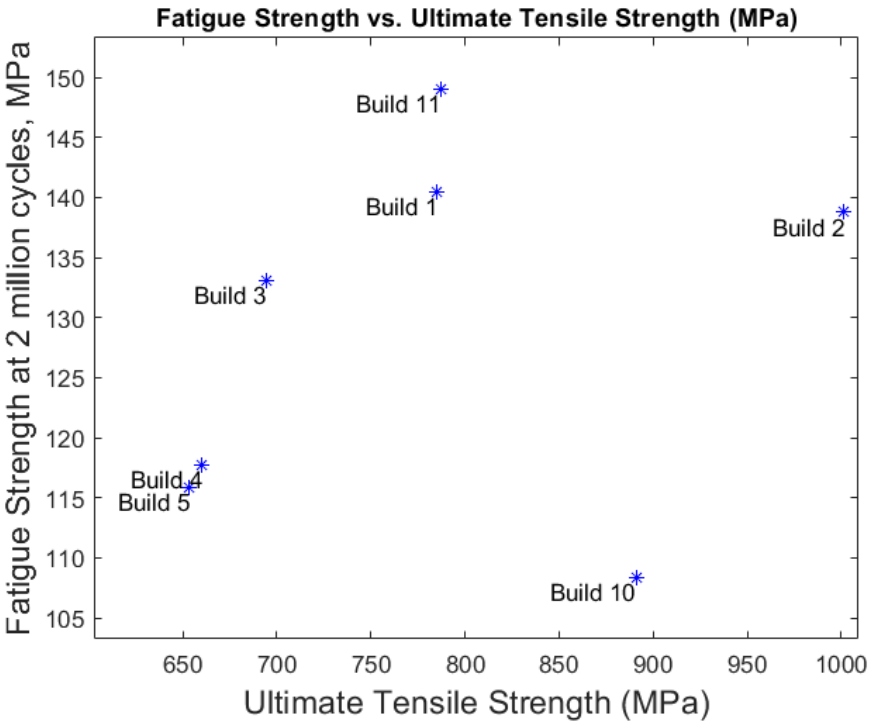

FIGURE 60: Fatigue strength (small xy, as-is) vs. ultimate tensile strength for xy specimens.

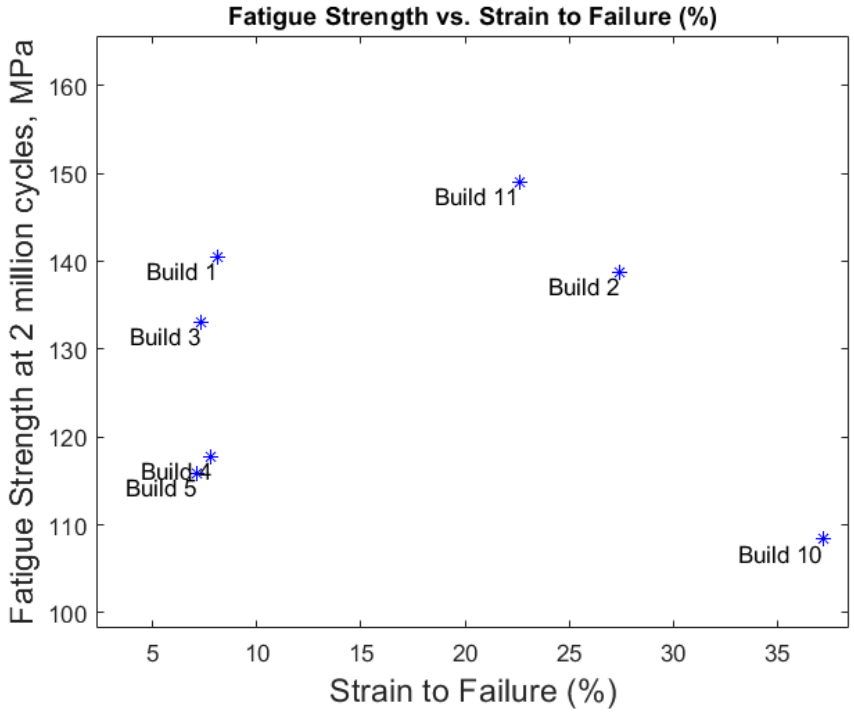

FIGURE 61: Fatigue strength (small xy, as-is) vs. strain to failure for xy specimens.

4.3. Influence of process parameters on fatigue strength

4.3.1. Small z specimens (as-is and polished)

This section contains plots to determine if there are any clear correlations of the AM process parameters with fatigue strength values measured on the small z specimens. A strong positive correlation was seen been VED (Eq. 1) and HCF strength (see FIGURE 64). Each data point corresponds to a build, with separate symbols for polished and as-is specimens. Higher VEDs yield better results in the form of improved microstructure, if no excessive VED is used as keyholing defects may be generated. As it shown in the SEM fractography (section 4.5), no keyhole defects were observed in the fractures but the improvement in strength seems to stagnate for >45 J/mm^3, suggesting an optimal VED of that value.

FIGURE 63 shows the relationship between laser velocity and fatigue strength. There is not any clear relationship between these parameters. For instance, the highest velocity (900 mm/s) generated the best (build 3) and the worst (build 7). As seen in FIGURE 13, different combinations of power and velocity are known to generate a range of microstructures and defect features. If very high power is used, the laser speed should also be increased to avoid added porosity. On the other hand, if the power is relatively low, very high laser scan speeds will not yield good results. For this project, 110 W was used which lies on the lower end of the typical power range. This factor coupled with the variability introduced by the AM machine system and the variations of hatch spacing, pattern and post-processing makes the relationship between HCF and scan velocity very complex to extract by simple regression of a single parameter.

A weak negative correlation between HCF and hatch spacing can be observed in FIGURE 62, where higher hatch spacings are associated to lower fatigue strengths. The highest strength was obtained for a hatch spacing of 70 µm. Although no clear trends can be found in the literature about the hatch spacing, Criales et al. [41] does recommend medium to high hatch spacings to obtain an isotropic characteristic.

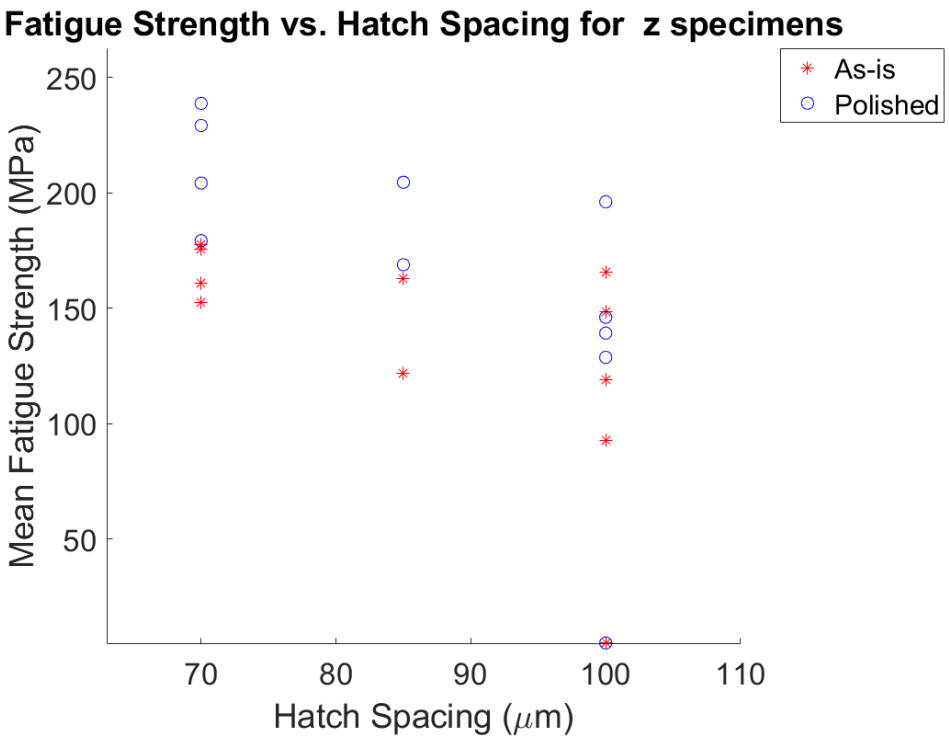

FIGURE 62: Fatigue Strength vs. Hatch Spacing for z specimens.

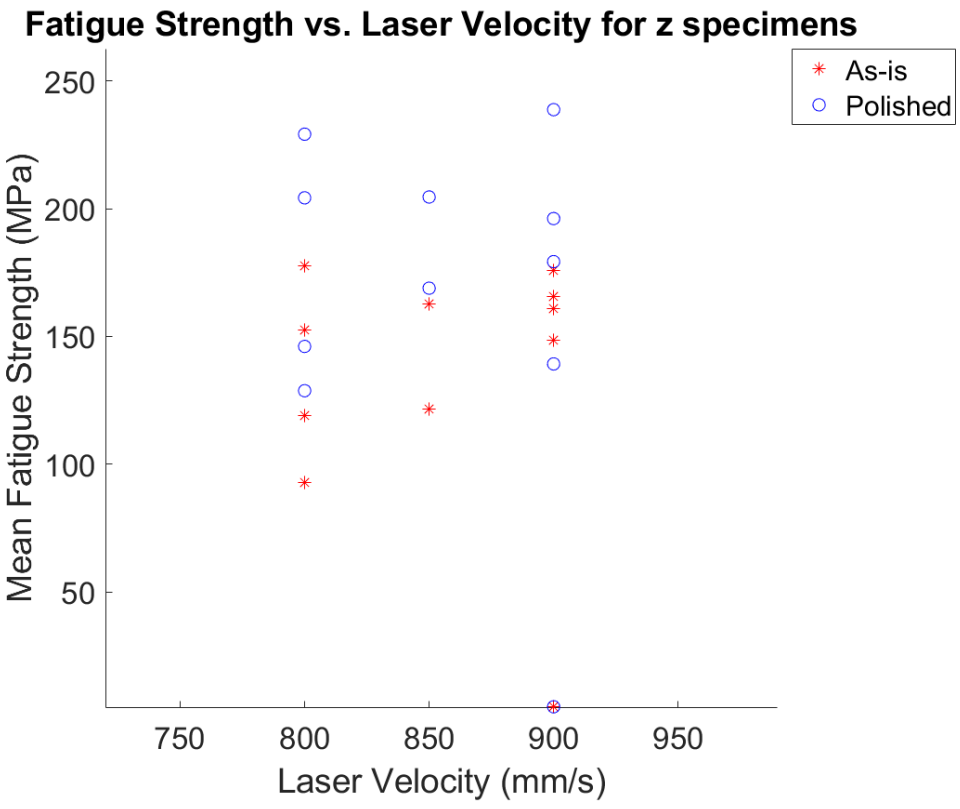

FIGURE 63: Fatigue Strength vs. Laser Velocity for z specimens.

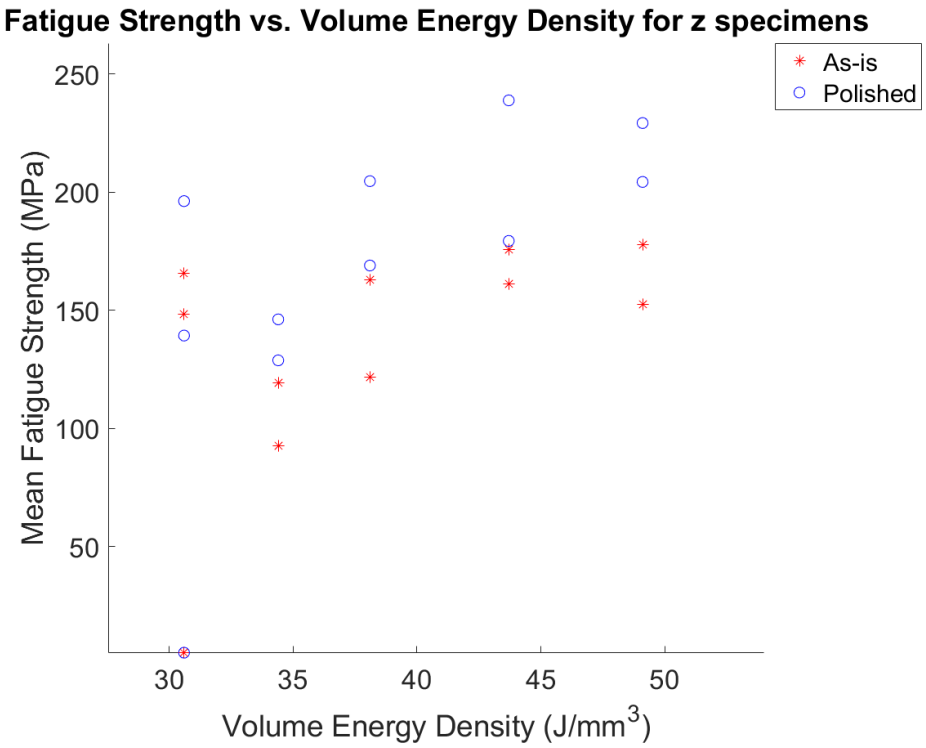

FIGURE 64: Fatigue Strength vs. Volume Energy Density of z specimens.

4.3.2. Small xy specimens (as-is).

On the other hand, the results for the xy specimens are surprisingly very different. Here, no positive correlation with HCF can be observed in the VED plot (FIGURE 67). High VED (50 J/mm^3) obtained the best results for small xy, but low VED obtained also good results for some builds.

Something similar can be observed in FIGURE 65 which compares hatch spacing to fatigue strengths. The highest (100 µm) and lowest (70 µm) values of the tested hatch spacings were the ones that generated the best results for this specimen group. The hatch spacing of 100 µm gave good results in build 2 but was also associated with the lowest performing builds (7,8). FIGURE 66 shows this same U-shaped correlation between fatigue strength and scan velocity, where a laser speed of 800 mm/s generated the best results but also the worst.

Overall, no clear trend between processing parameters and HCF was found for xy specimens. The fact that z specimens did correlate with regards to the VED exacerbates the difference in properties between z and xy specimens.

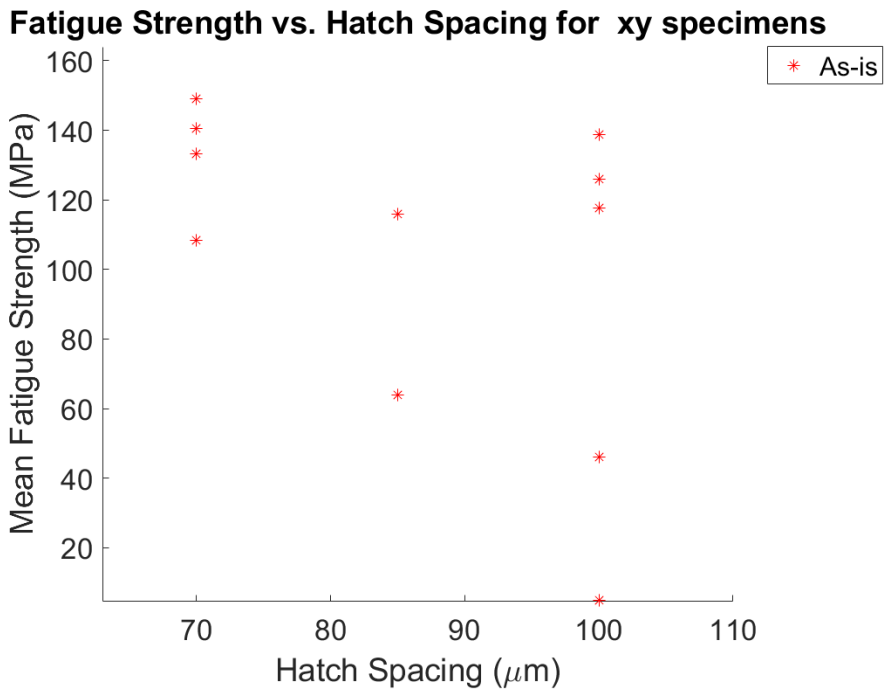

FIGURE 65: Fatigue strength vs. hatch spacing for xy specimens.

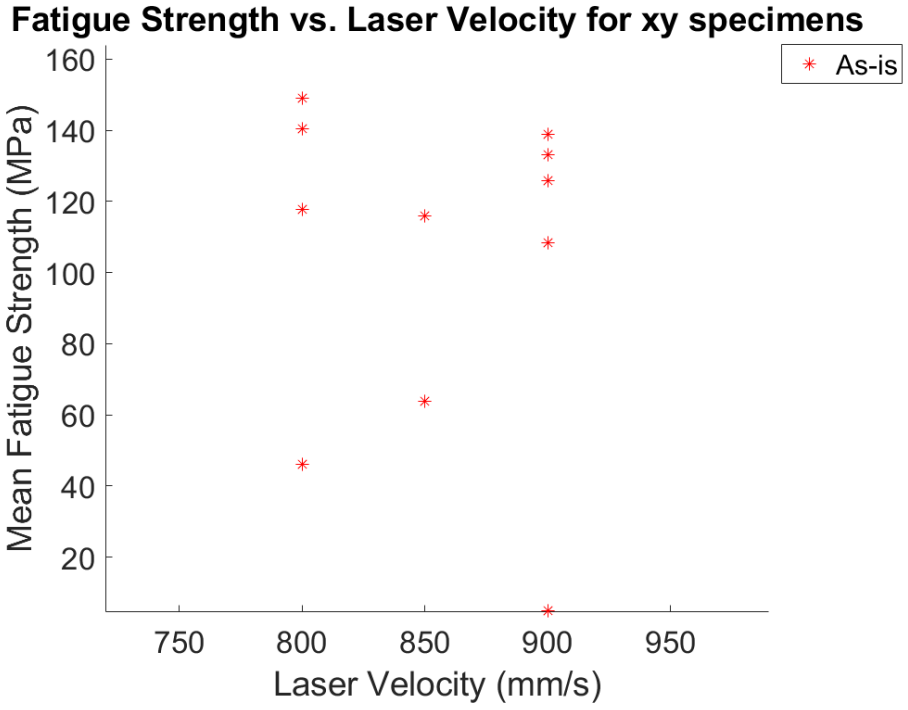

FIGURE 66: Fatigue strength vs. laser velocity for xy specimens.

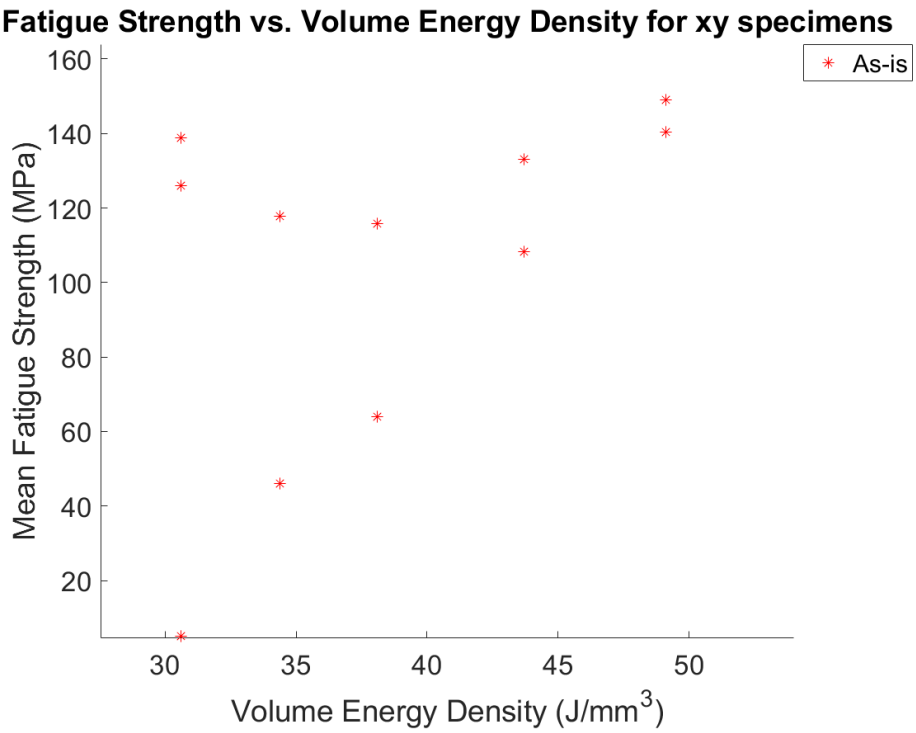

FIGURE *67*: Fatigue strength vs. volume energy density of xy specimens.

4.4. Estimation of fatigue strength for different stress ratios

The stress ratio in applications is often not the same as the stress ratio applied in the fatigue test program. Here, all tests were conducted at R = 0.1. The methods described in Chapter 3 for mean stress correction were used to create diagrams to estimate fatigue strengths at $2x10^6$ cycles for stress ratios from R = -1 (fully reversed) to R = 0.5. Fatigue strengths are based on stress amplitude. Diagrams were generated for small z specimens and for each build except build 7 (the one with extremely low fatigue strength). These are shown in FIGURES 68-78. For Goodman and Gerber, the average ultimate tensile strength was used. The value for the Concept M2 was 910 MPa (builds 1-6) and 802.4 MPa (builds 7-11). However, considering the fact that both machines obtained different values of UTS, the average was calculated for each machine. For the Walker analysis, it was assumed that $\gamma = 0.42$, which is value found that fit the data reported in MMPDS-14 for wrought IN625 [58]. It is likely that this value fits the AM specimens reasonably well, though no separate regression analysis has been done since we only have data at R = 0.1. Given that this γ value is close to 0.5 (for which the Walker equation reduces to the SWT equation), the SWT equation is also a reasonable equation to use.

As was expected from the equation forms, the SWT and Walker equations both predict similar fatigue strengths. Also, the Gerber equation provides the most conservative estimates for low values of R. For builds 1, 2, 3, 6, 9, 10 and 11 the Goodman equation yields similar results to the SWT and Walker equations, but it estimates much lower strengths as R approaches -1 for the rest of the builds. The reason for the extremely low estimates of fatigue strength of the Gerber equation is that the Gerber equation is typically used for highly ductile materials. Finally, FIGURE 78 was generated using all four mean stress correction methods to give a range of life values for fully-

reversed loading (R = -1) in the as-is condition so that the results of the different builds can be directly compared.

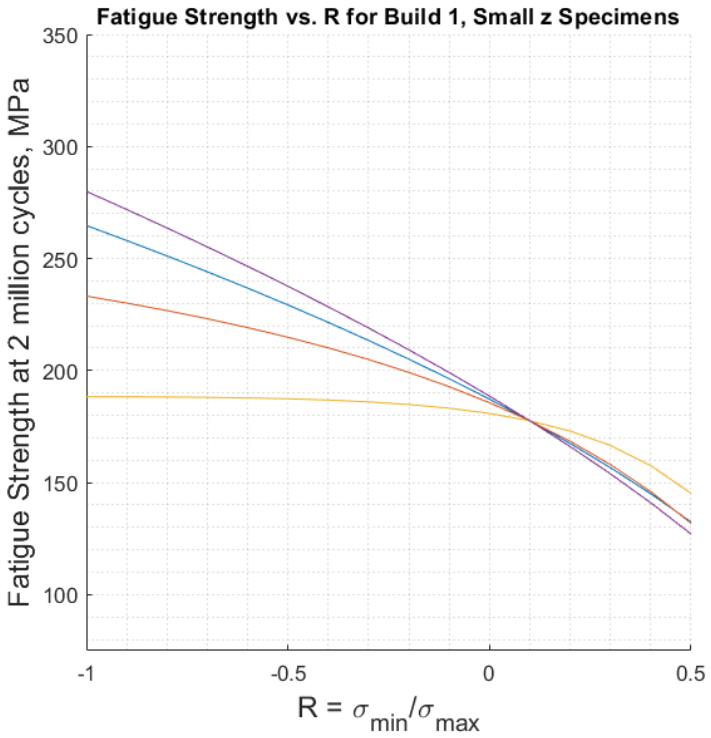

FIGURE 68: Fatigue strength vs. build 1, small z specimens.

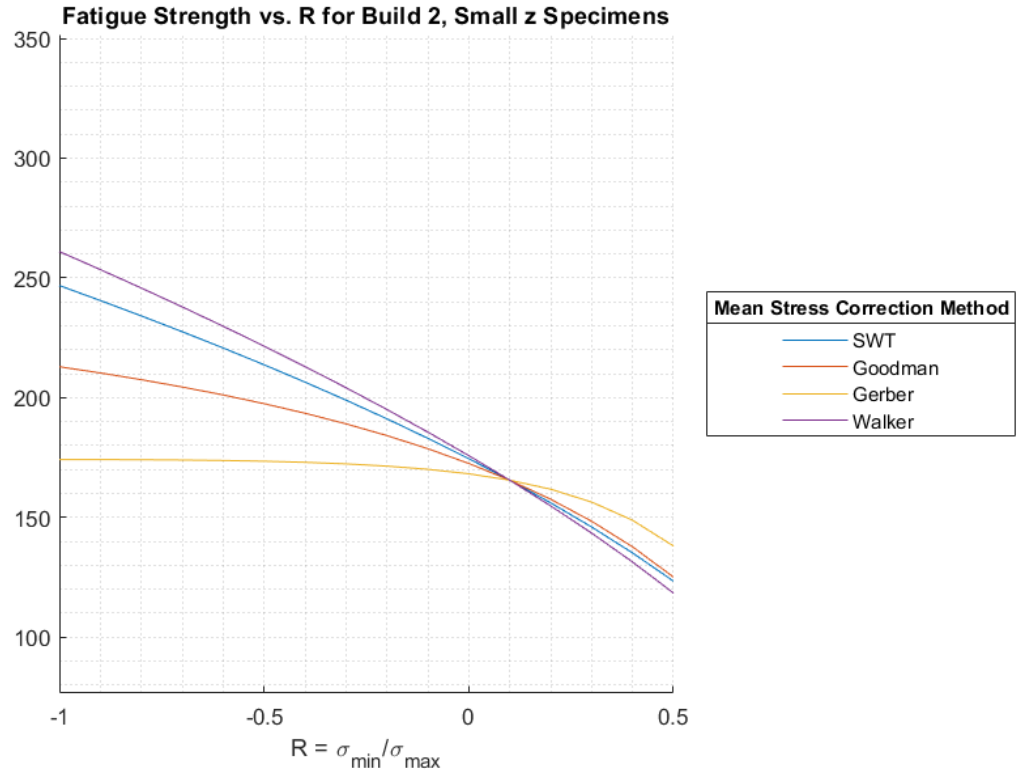

FIGURE 69: Fatigue strength vs. build 2, small z specimens.

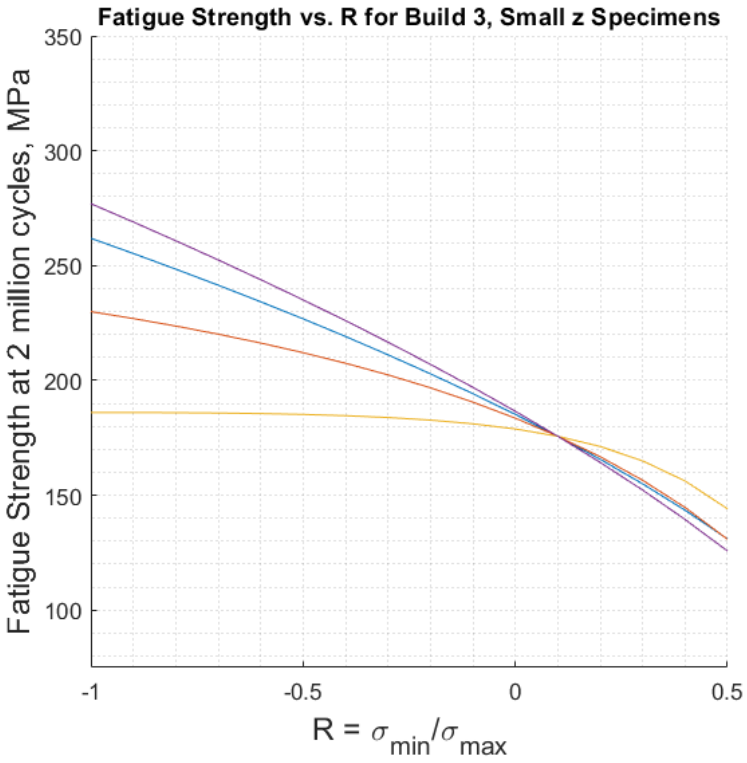

FIGURE 70: Fatigue strength vs. build 3, small z specimens.

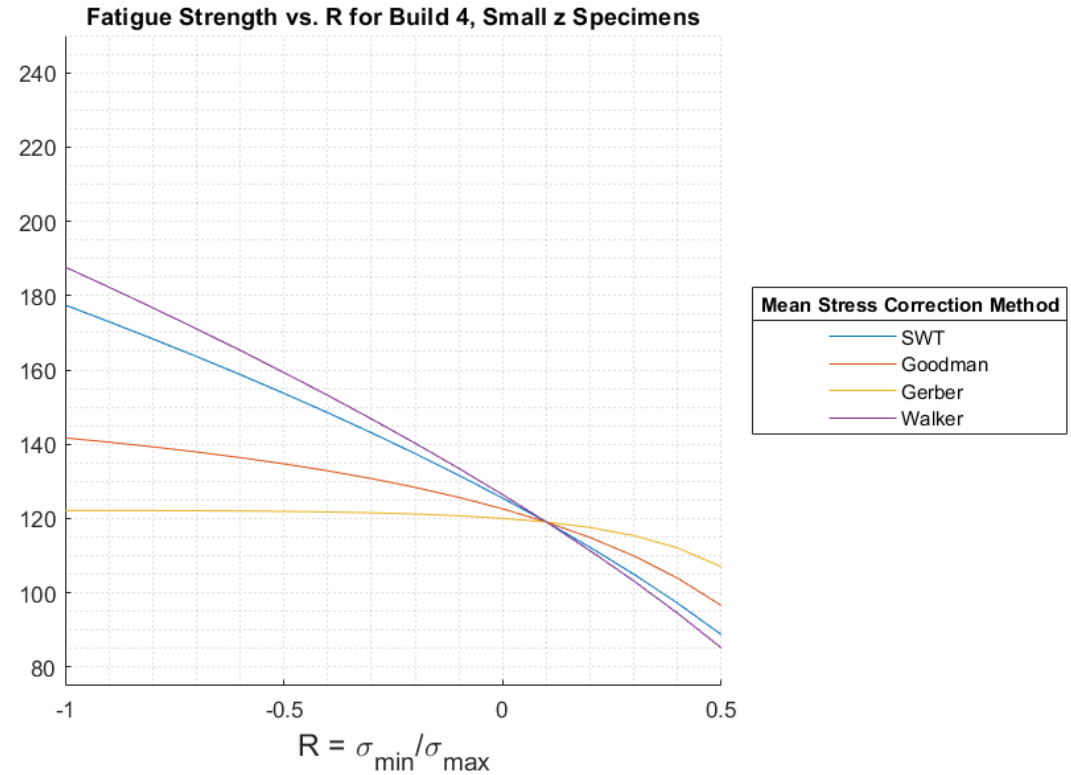

FIGURE 71: Fatigue strength vs. build 4, small z specimens.

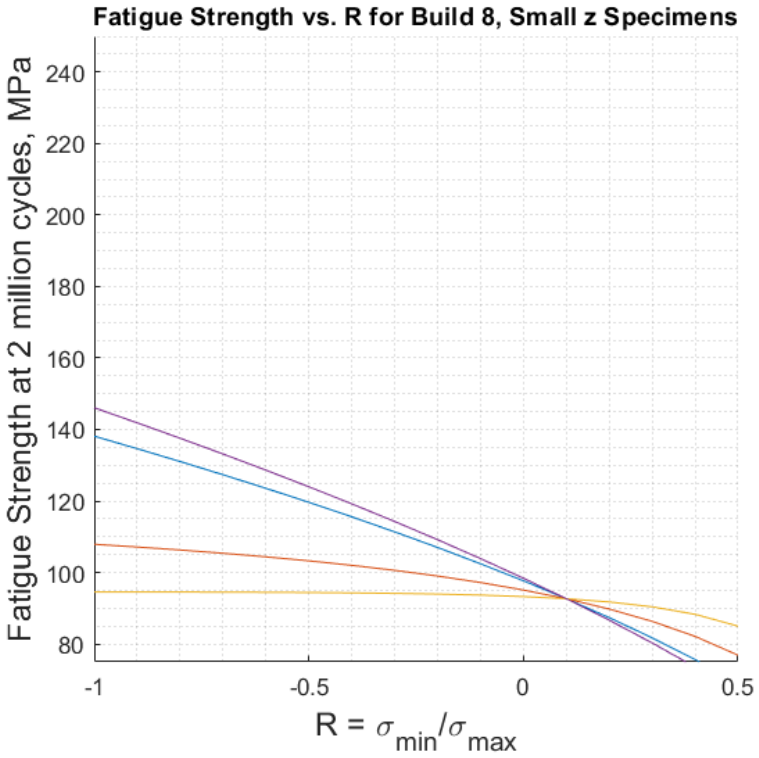

FIGURE 72: Fatigue strength vs. build 5, small z specimens.

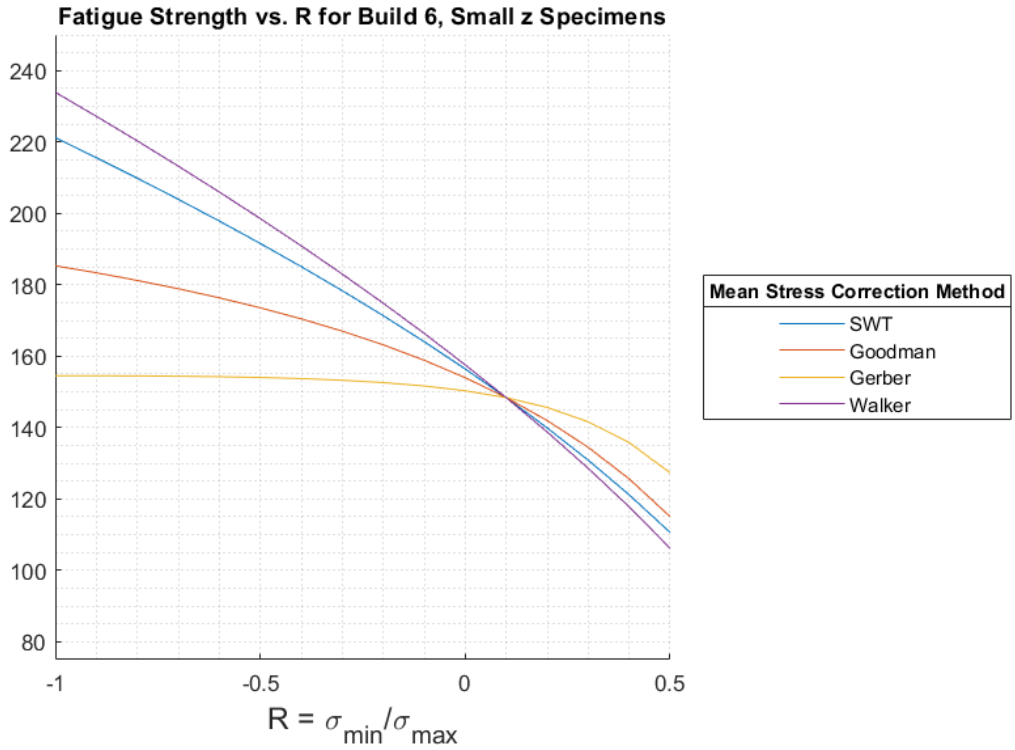

FIGURE 73: Fatigue strength vs. build 6, small z specimens.

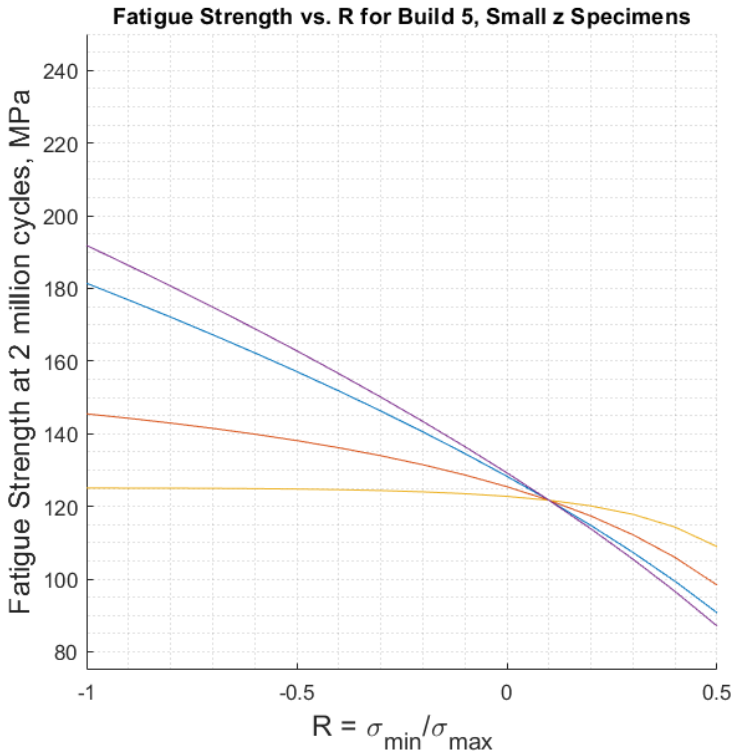

FIGURE 74: Fatigue strength vs. build 8, small z specimens.

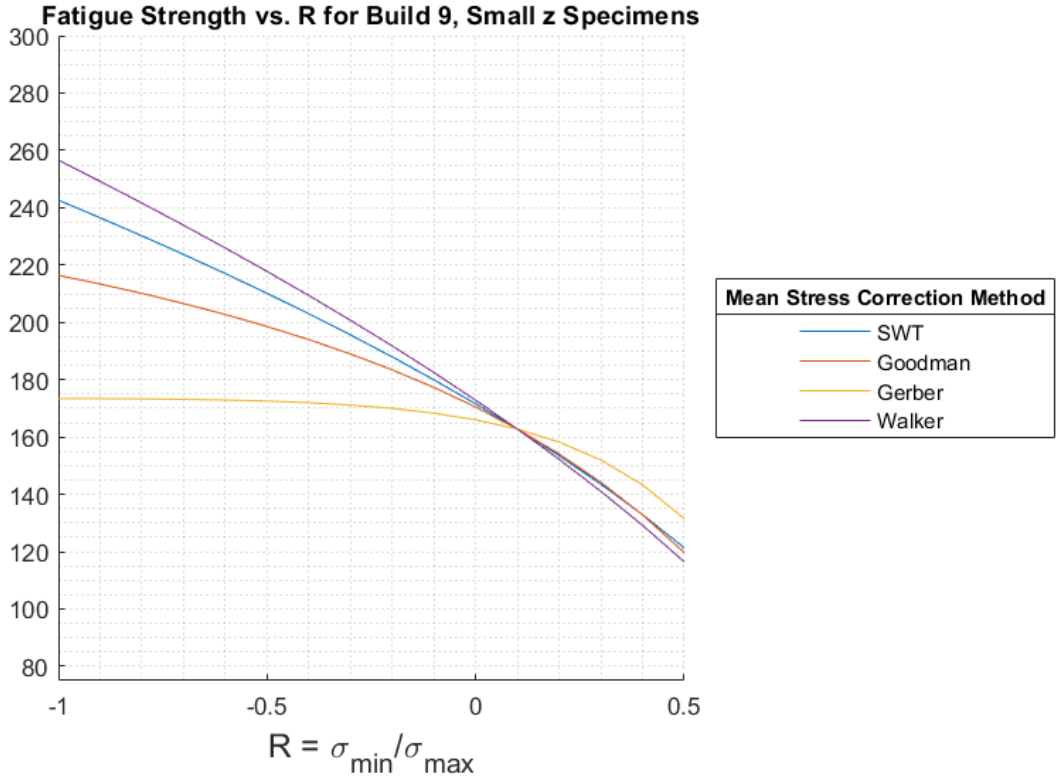

FIGURE 75: Fatigue strength vs. build 9, small z specimens.

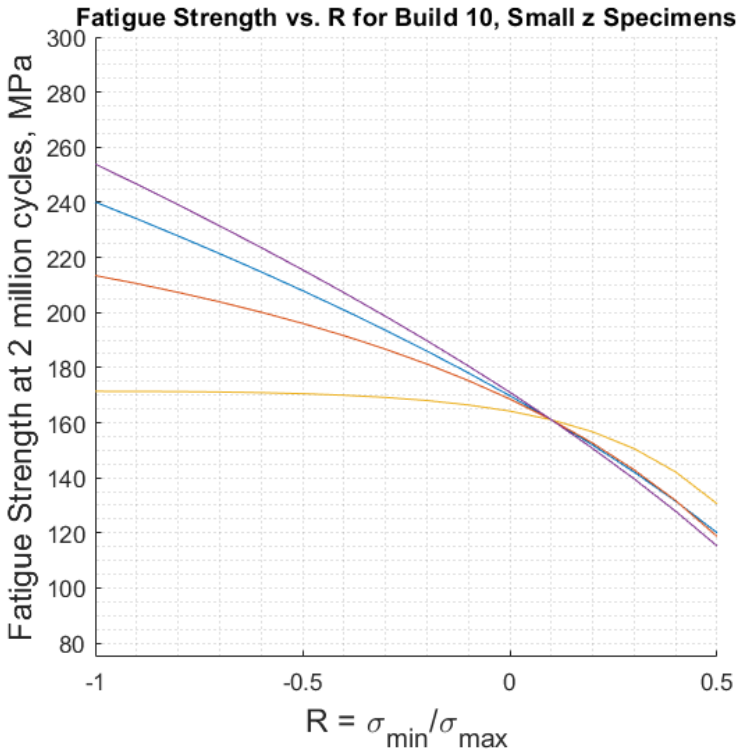

FIGURE 76: Fatigue strength vs. build 10, small z specimens.

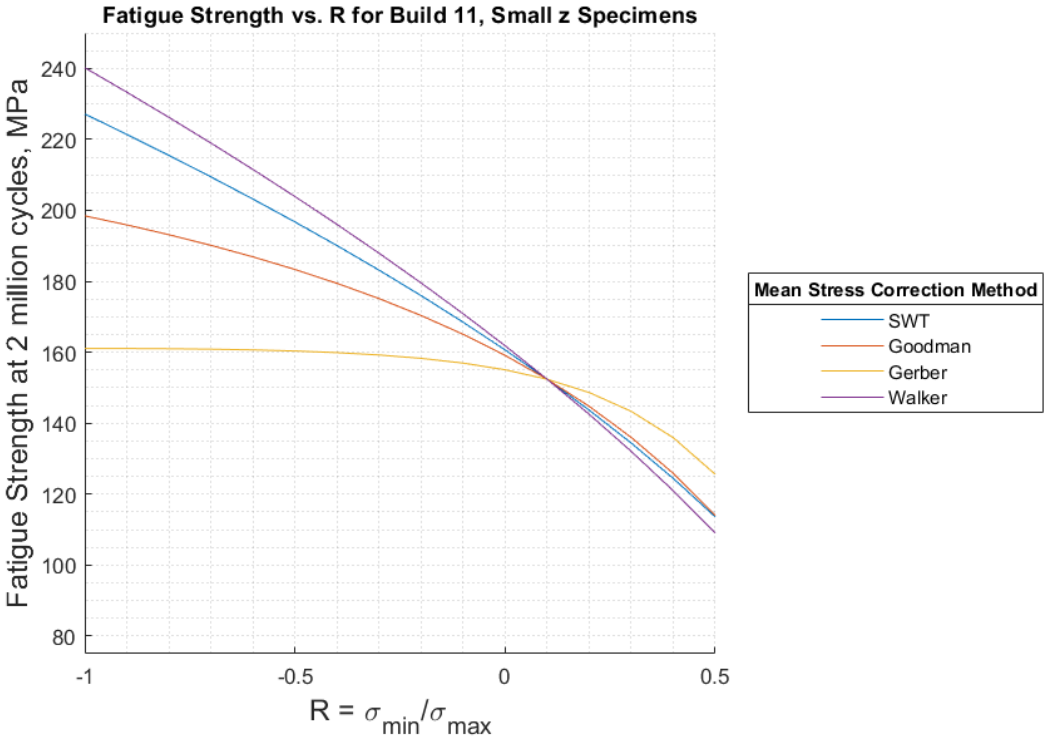

FIGURE 77: Fatigue strength vs. build 11, small z specimens.

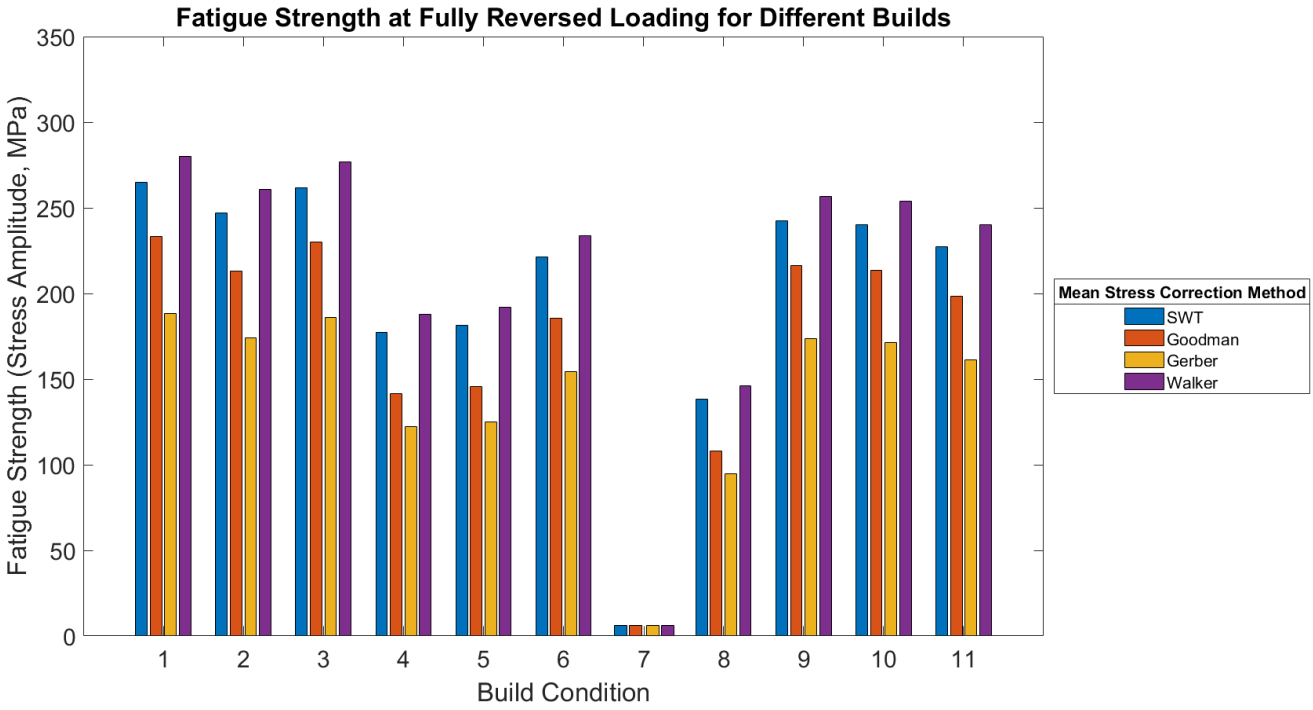

FIGURE 78: Estimates of fatigue strength for 2 million cycles under fully-reversed loading (R=-1).

4.5. Fracture surface study

The fracture surfaces of several fatigue specimens were examined to identify the "killer" defects that caused the fatigue cracks to nucleate. Fatigue specimens from all builds except builds 2 and 10 were examined. The subset of specimens examined were selected to gain the greatest contribution to the understanding of the microstructure features influence fatigue strength. The goal was to provide explanations for the large variability of fatigue strengths measured among the builds.

The first step was to conduct a macroscopic visually inspection the fractured surfaces to identify the general location where the crack appeared to nucleate in the gage section of the specimen and whether it appeared to form on the narrow edge, wide sides, at a corner, or internally. This was done to classify the specimens according to the perceived crack nucleation site, distinguishing cracks that were thought to nucleate in the internally or at the surface. However, although visual inspection and photographs taken with a regular digital camera for documentation are useful for classification, further microscopic imaging is necessary to identify the "killer" defect and other features of the microstructure that influence the fatigue crack nucleation and its growth. Both a digital optical microscope, Keyence VHX-600 and scanning electron microscope TESCAN MIRA3 (SEM) were used for the microscopic observations. Different magnifications were used to pinpoint specific features of the surfaces. Each specimen studied includes a macroscopic view of the entire fracture surface to clarify the microscopic location examined and its orientation relative to the build direction. All captions specify specimen number, build direction, specimen type and the fatigue strength at $2x10^6$ cycles. All values reported in this section for fatigue strength correspond to stress amplitude.

4.5.1. Visual inspection results

A summary of all small HCF test specimens indicating the likely location of the fatigue crack nucleation in shown in TABLE 19. This table contains a classification of all tested HCF specimens through macroscopic visual observation of the fracture surface. For each data point, the visible nucleation site is indicated. If this location was very close to one of the sides, the specific side is indicated according to the naming criteria established in the DoE. In addition, the Condition column provides some additional details: P indicates the gage section of the specimen was polished on all four sides and FFS corresponds to a failed first step. In general, the fatigue crack formed at or very close to a surface, with the narrow sides the most likely origin of the fatigue crack (75% of all analyzed specimens. Some of the small z specimens nucleated the fracture from the wide side. However, all small xy specimens failed from one of the narrow sides except specimen 11-17.

TABLE 19: Visual inspection of all tested specimens.

build	specimen	specimen type	crack initiation site	if close to side, which one?	Condition
1	7	small z	close to side	narrow side 2	
	8	small z	close to side	narrow side 2	P
	9	small z	close to side	narrow side 2	P
	10	small z			
	11	small z	close to side	narrow side 1	
	12	small z	close to side	narrow side 1	
	13	small xy	close to side	narrow side top	FFS
	14	small xy	close to side	narrow side top	
	15	small xy			
	16	small xy			
	17	small xy			
	18	small xy	close to side	narrow side bottom	
2	7	small z	close to side	wide side towards front	P
	8	small z	close to side	narrow side 1	
	9	small z	close to side	wide side towards back	
	10	small z			
		small z			P
	12	small z	close to side	wide side towards back	
	13	small xy			
	14	small xy			
	15	small xy			
	16	small xy	close to side	narrow side bottom	FFS
	17	small xy	close to side	narrow side bottom	FFS
	18	small xy	close to side	narrow side bottom	
3	7	small z	close to side	narrow side 2	
	8	small z	SCS		P
	9	small z	middle		P
	10	small z			
	11	small z	close to side	narrow side 2	

TABLE 19 continued

	12	small z	close to side	narrow side 2	
	13	small xy	close to side	wide side towards back	
	14	small xy			
	15	small xy			
	16	small xy	close to side	narrow side bottom	FFS
	17	small xy			
	18	small xy			
4	7	small z	close to side	wide side towards front	FFS
	8	small z	middle		
	9	small z	close to side	narrow side 1	
	10	small z			
	11	small z	close to side	wide side towards front	P
	12	small z	close to side	wide side towards front	P
	13	small xy	close to side	narrow side top	
	14	small xy			
	15	small xy	close to side	narrow side top	FFS
	16	small xy	close to side	narrow side bottom	FFS
	17	small xy			
	18	small xy			
5	7	small z	close to side	wide side towards front	FFS
	8	small z			P
	9	small z	close to side	wide side towards front	P FFS
	10	small z	close to side	narrow side 1	FFS
	11	small z	close to side	narrow side 2	FFS
	12	small z	close to side	wide side towards front	
	13	small xy	close to side	narrow side bottom	
	14	small xy			
	15	small xy			
	16	small xy			
	17	small xy	close to side	narrow side bottom	FFS
	18	small xy			
6	7	small z			P
	8	small z	close to side	wide side towards back	
	9	small z	middle		FFS
	10	small z			
	11	small z			P
	12	small z			
	13	small xy	close to side	narrow side bottom	FFS
	14	small xy			
	15	small xy	close to side	narrow side top	
	16	small xy	close to side	narrow side bottom	FFS
	17	small xy			

TABLE 19 continued

	18	small xy			
7	7	small z	not clear		FFS
	8	small z	not clear		P FFS
	9	small z			
	10	small z			
	11	small z			
	12	small z			
	13	small xy	not clear		FFS
	14	small xy			
	15	small xy			
	16	small xy			
	17	small xy			
	18	small xy			
8	7	small z	close to side	narrow side 1	P
	8	small z	close to side	narrow side 2	FFS
	9	small z			
	10	small z			
	11	small z			
	12	small z			
	13	small xy	close to side	narrow side top	FFS
	14	small xy			
	15	small xy			
	16	small xy			
	17	small xy			
	18	small xy			
9	7	small z	close to side	narrow side 2	
	8	small z			
	9	small z			
	10	small z	close to side	narrow side 2	
	11	small z			
	12	small z	close to side	narrow side 2	P
	13	small xy	close to side	narrow side bottom	FFS
	14	small xy	not clear		
	15	small xy	close to side	narrow side bottom	FFS
	16	small xy			
	17	small xy			
	18	small xy			
10	7	small z	close to side	narrow side 2	
	8	small z			
	9	small z			
	10	small z	not clear		FFS
	11	small z			

TABLE 19 continued

	12	small z			
	13	small xy	close to side	narrow side bottom	FFS
	14	small xy			
	15	small xy			
	16	small xy	close to side	narrow side bottom	FFS
	17	small xy			
	18	small xy	close to side	narrow side bottom	FFS
11	7	small z	close to side	wide side towards back	P
	8	small z			
	9	small z			
	10	small z	close to side	wide side towards back	]
	11	small z			
	12	small z	close to side	narrow side 2	
	13	small xy	close to side	narrow side bottom	] FFS
	14	small xy	close to side	narrow side bottom	] FFS
	15	small xy			X,R
	16	small xy	close to side	narrow side bottom	FFS
	17	small xy	close to side	wide side towards back	
	18	small xy			

4.5.2. Build 1

The good performance of build 1 specimens can be attributed to a good microstructure. FIGURE 79 shows the fatigue crack formation site of specimen 1-8 (small z, polished, 212.15 MPa of fatigue strength amplitude). The nucleation site was on the narrow edge of the specimen, where carbides were observed (FIGURE 79a). No major lack-of-fusion defects were found on the fracture surface of this specimen. The fatigue crack nucleation site appears to be associated with the carbides that are known to act as stress risers when subjected to fatigue loads. In this case, several carbides were close together resulting in a magnified effect on the cyclic stress concentration

Similarly, specimen 1-14 (small xy, as-is, 139.9 MPa), shown in FIGURE 80, was also observed to have carbides near the edge on the fracture surface. However, the fatigue crack nucleation site is associated with the presence of a large, concentrated lack-of- fusion defect close to the carbides. The exact origin of the fracture is difficult to pinpoint because the site where the crack appears to connect to both defects. Nevertheless, FIGURE 80 makes it clear that large cavities (>400 mm) such as the one seen in FIGURE 80a will reduce strength significantly. Therefore, the reduction in the fatigue strength for the small xy specimen compared to the small z specimen in build 1 is due to a larger concentration and size of lack-of-fusion defects.

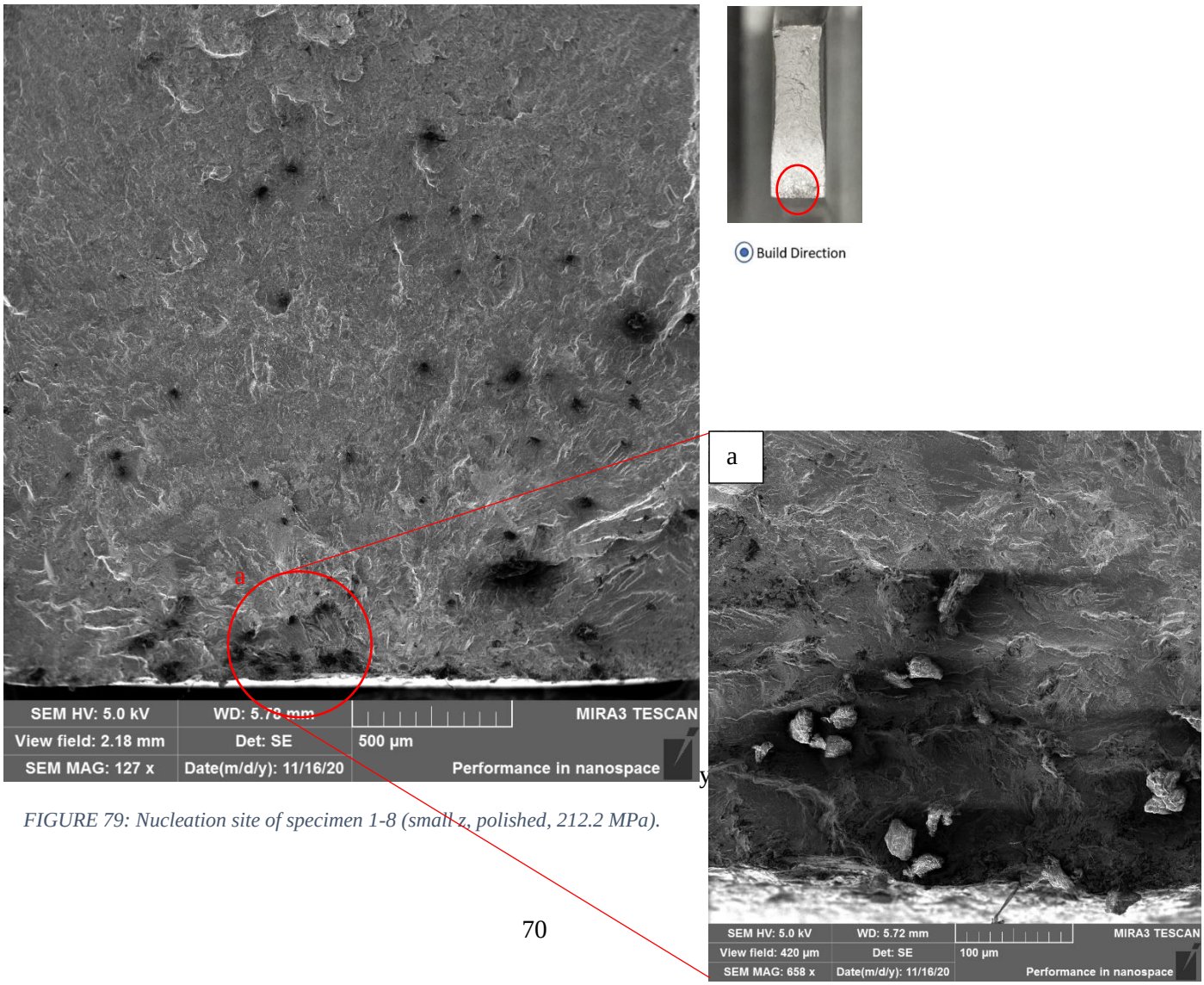

FIGURE 79: Nucleation site of specimen 1-8 (small z, polished, 212.2 MPa).

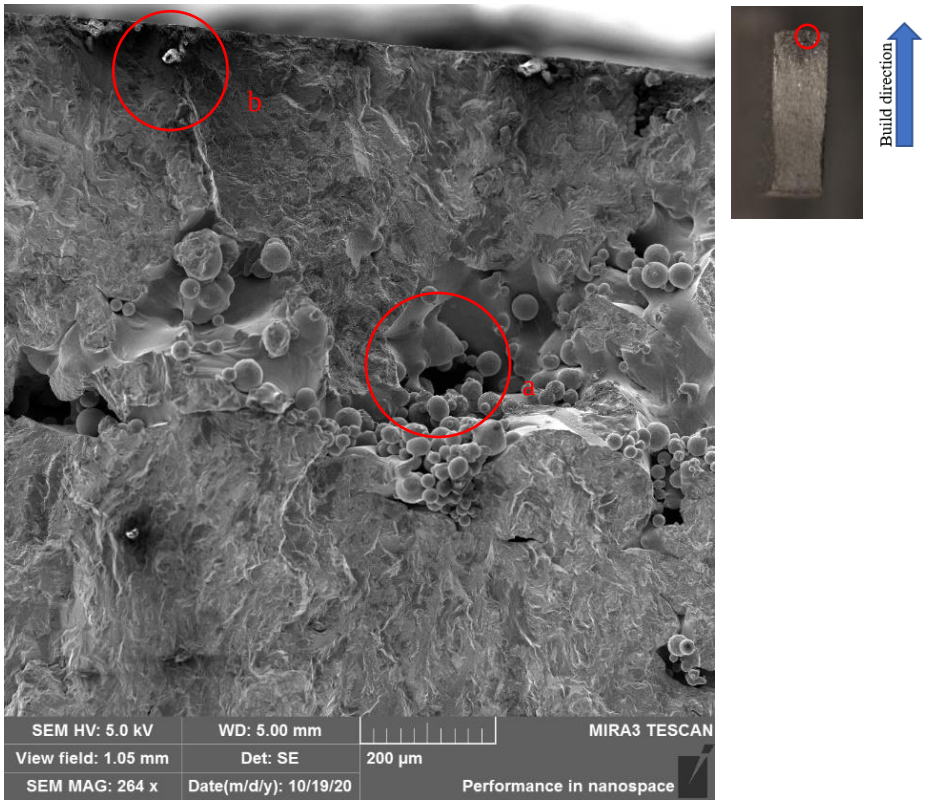

FIGURE 80: Nucleation site of specimen 1-14 (small xy, as-is, 139.9 MPa).

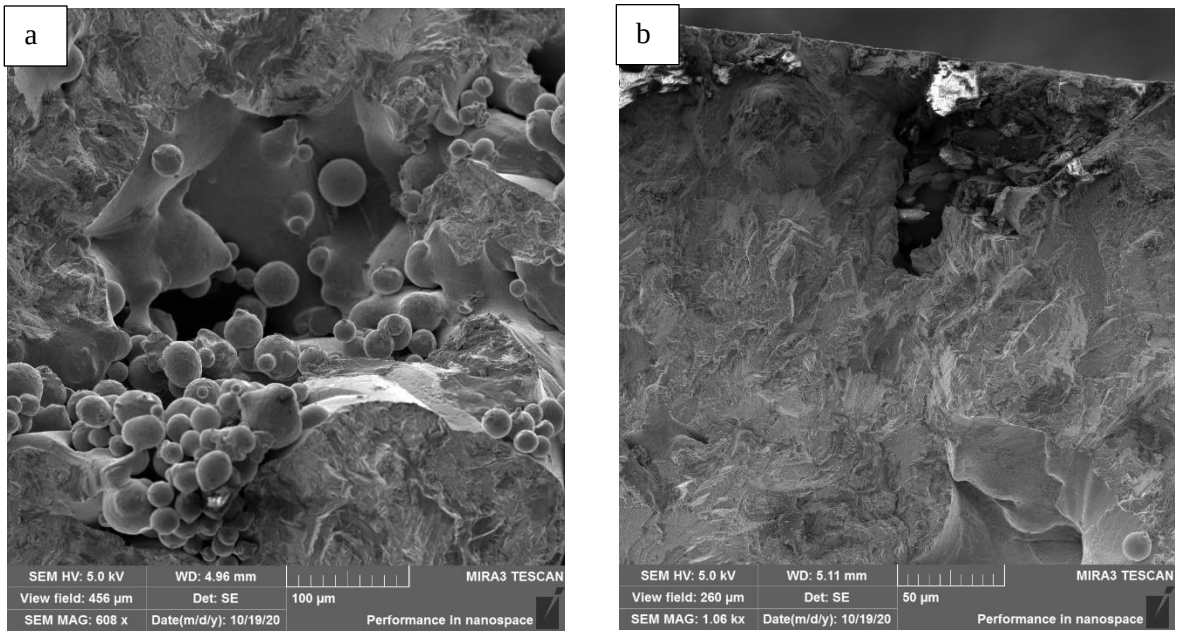

4.5.3. Build 3

Build 3 exhibited good fatigue behavior overall, but a large variability was found between as-is and polished specimens. Only one small xy specimen from build 3 was tested due to a large number of flawed specimens (some were extremely warped, some had visible cracks), which may explain the higher variability between small z and xy compared to builds 1 and 2 (see FIGURE 42). For this build, two small z specimens (as-is and polished) were imaged to understand the disparity.

The SEM imaging of specimen 3-9 (FIGURE 81) showed reduced porosity and lack-of-fusion defects. This specimen obtained a very high fatigue strength (239.6 MPa). The fatigue crack appeared to have initiated near the surface closer to the middle of the wide side (see FIGURE 81a) where a mid-sized lack-of-fusion defect (<250µm) was detected. FIGURE 81a and b reveal the presence of a carbide close to the surface of the specimen.

Carbide particles were also detected toward the edge of the fracture in specimen 3-12 (FIGURE 82a). However, this specimen obtained significantly less strength, approximately 100 MPa less (182.9 MPa). The shape of the fracture of specimen 3-12 suggests that the fatigue crack formed at a location where the carbides were most likely the origin near the as-is surfaced. The reduced fatigue life could be explained by the fact that the increase in the surface roughness coupled with the presence of the carbides near the surface caused the fatigue crack to form, while a larger stress was needed to nucleate the fatigue crack at the lack-of-fusion defect located in specimen 3-9.

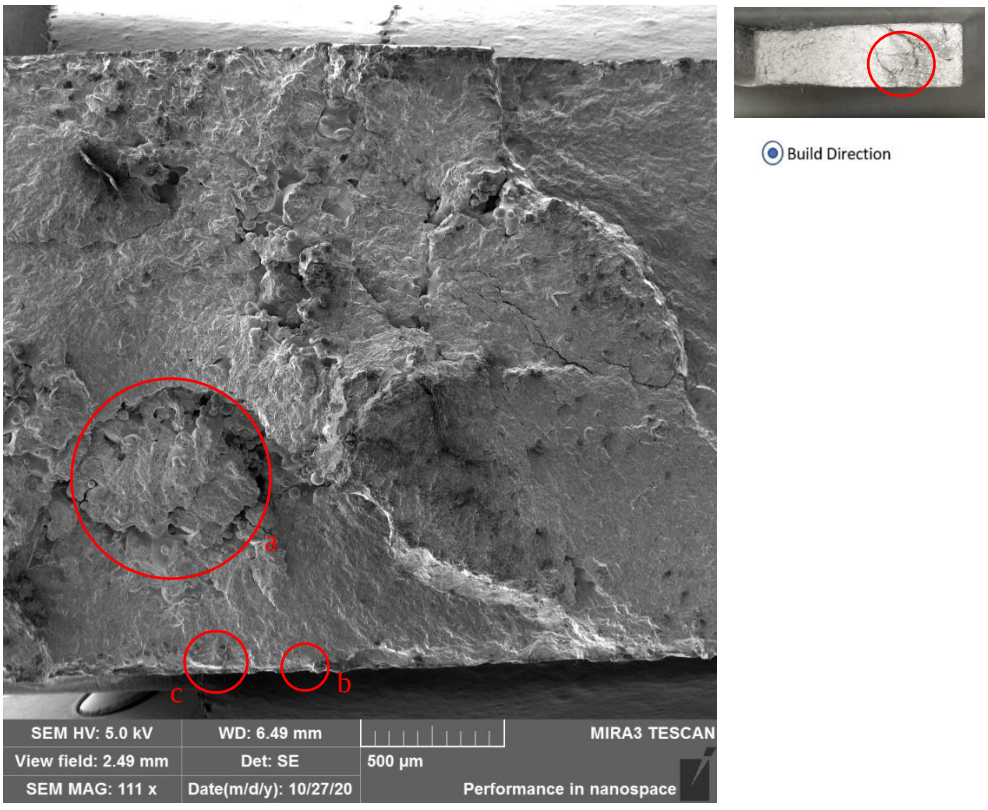

FIGURE 81: Nucleation site of specimen 3-9 (small z, polished, 239.6 MPa).

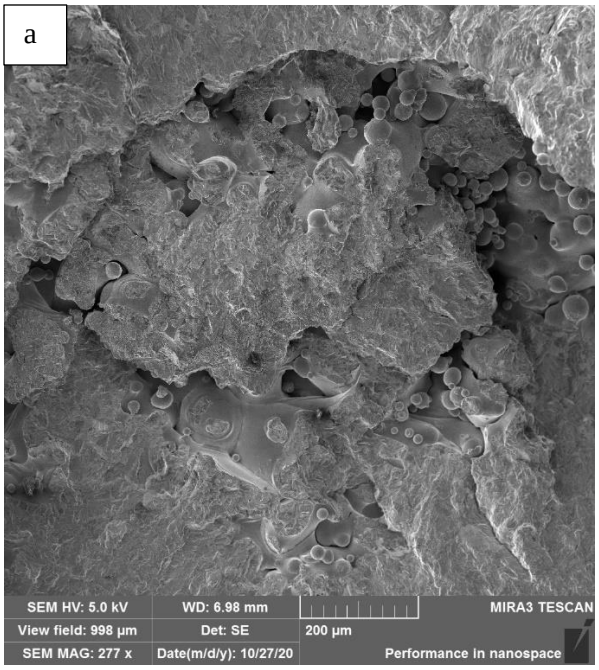
a
SEM HV: 5.0 kV
WD: 6.98 mm
MIRA3 TESCAN
View field: 998 µm
Det: SE
200 µm
SEM MAG: 277 x
Date(m/d/y): 10/27/20
Performance in nanospace

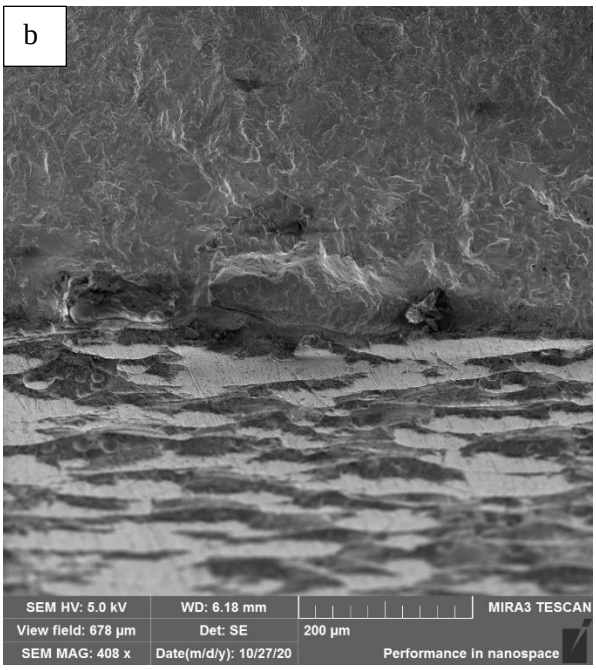
b
SEM HV: 5.0 kV
WD: 6.18 mm
MIRA3 TESCAN
View field: 678 µm
Det: SE
200 µm
SEM MAG: 408 x
Date(m/d/y): 10/27/20
Performance in nanospace

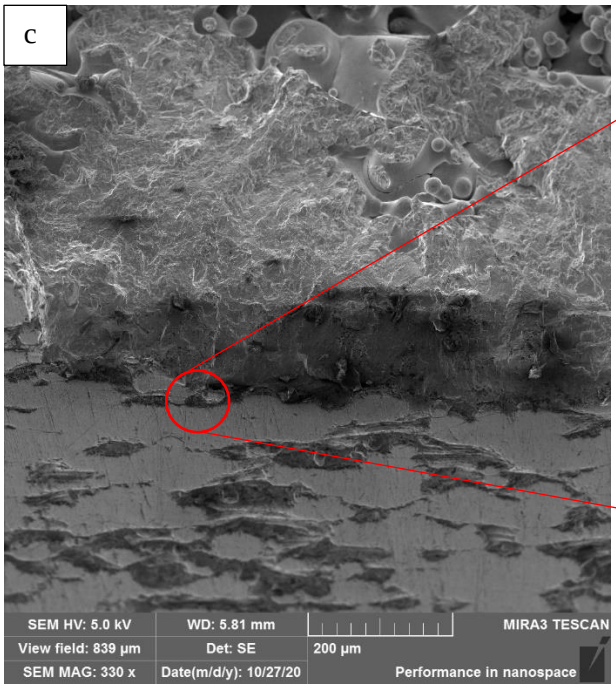
c
SEM HV: 5.0 kV
WD: 5.81 mm
MIRA3 TESCAN
View field: 839 µm
Det: SE
200 µm
SEM MAG: 330 x
Date(m/d/y): 10/27/20
Performance in nanospace

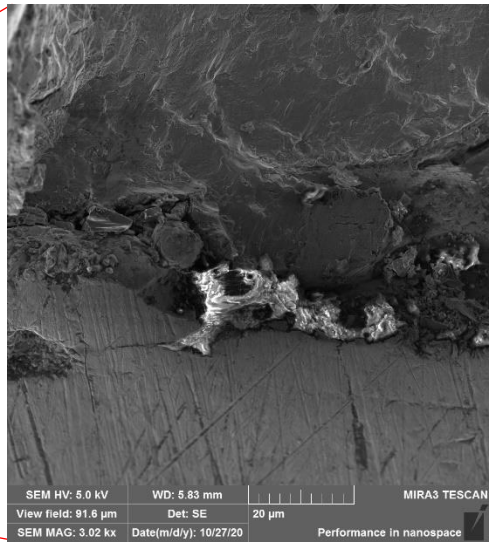
SEM HV: 5.0 kV
WD: 5.83 mm
MIRA3 TESCAN
View field: 91.6 µm
Det: SE
20 µm
SEM MAG: 3.02 kx
Date(m/d/y): 10/27/20
Performance in nanospace

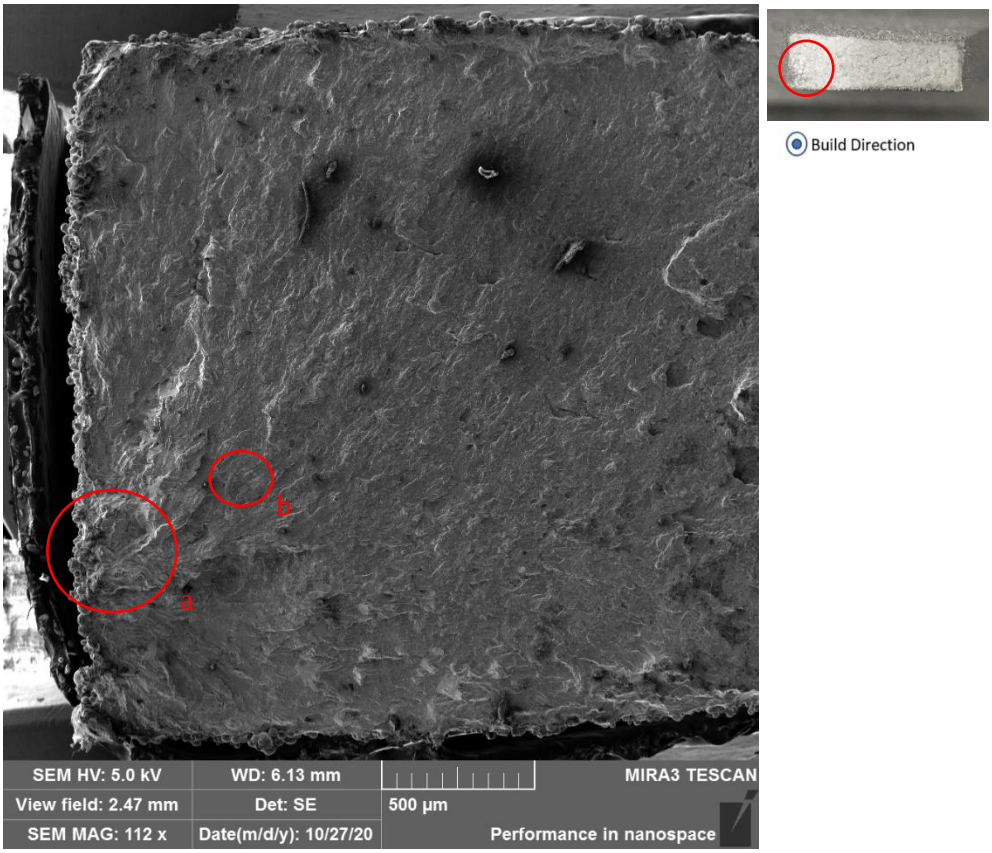

FIGURE 82: Nucleation site of specimen 3-12 (small z, as-is), 365.8 MPa.

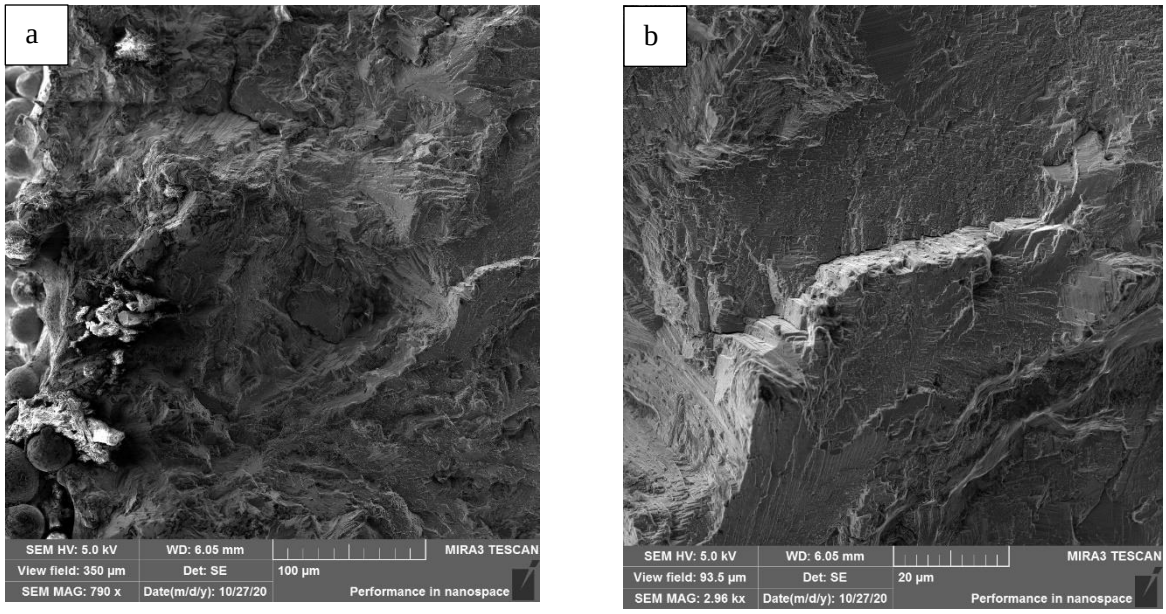

4.5.4. Build 4

Build 4 presented lower fatigue performance compared to the previous builds and a low variability between small z as-is and polished specimens. FIGURE 83a (specimen 4-12, small z, polished, 133 MPa) shows localized and significant lack-of-fusion defects towards the surface. Another specimen (4-11, small z, polished, 124.6 MPa) was imaged to confirm this tendency. The severity of the lack-of-fusion defects (>250µm) located close to the surface was likely the reason why the difference between polished and non-polished was reduced compared to the previous builds. Furthermore, the small difference between small xy and small z can also be attributed to these localized and large empty voids located near the surfaces.

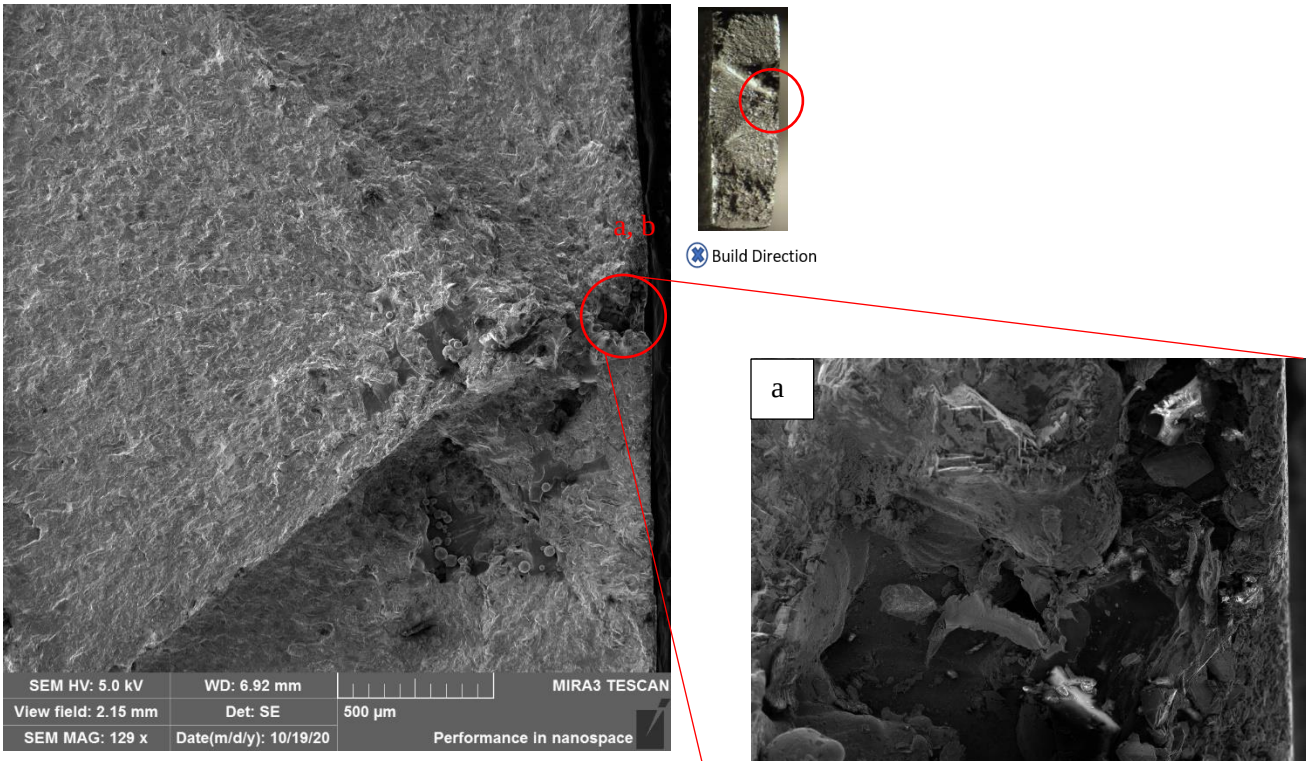

FIGURE 83: Nucleation site of specimen 4-12 (small z, polished, 133 MPa).

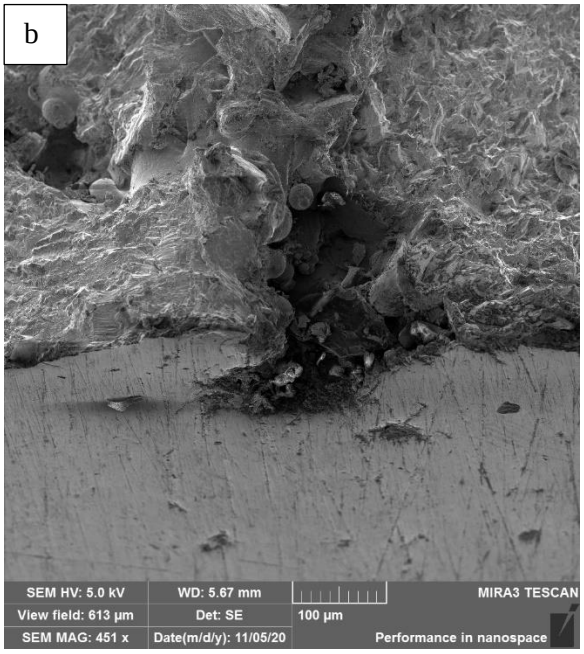

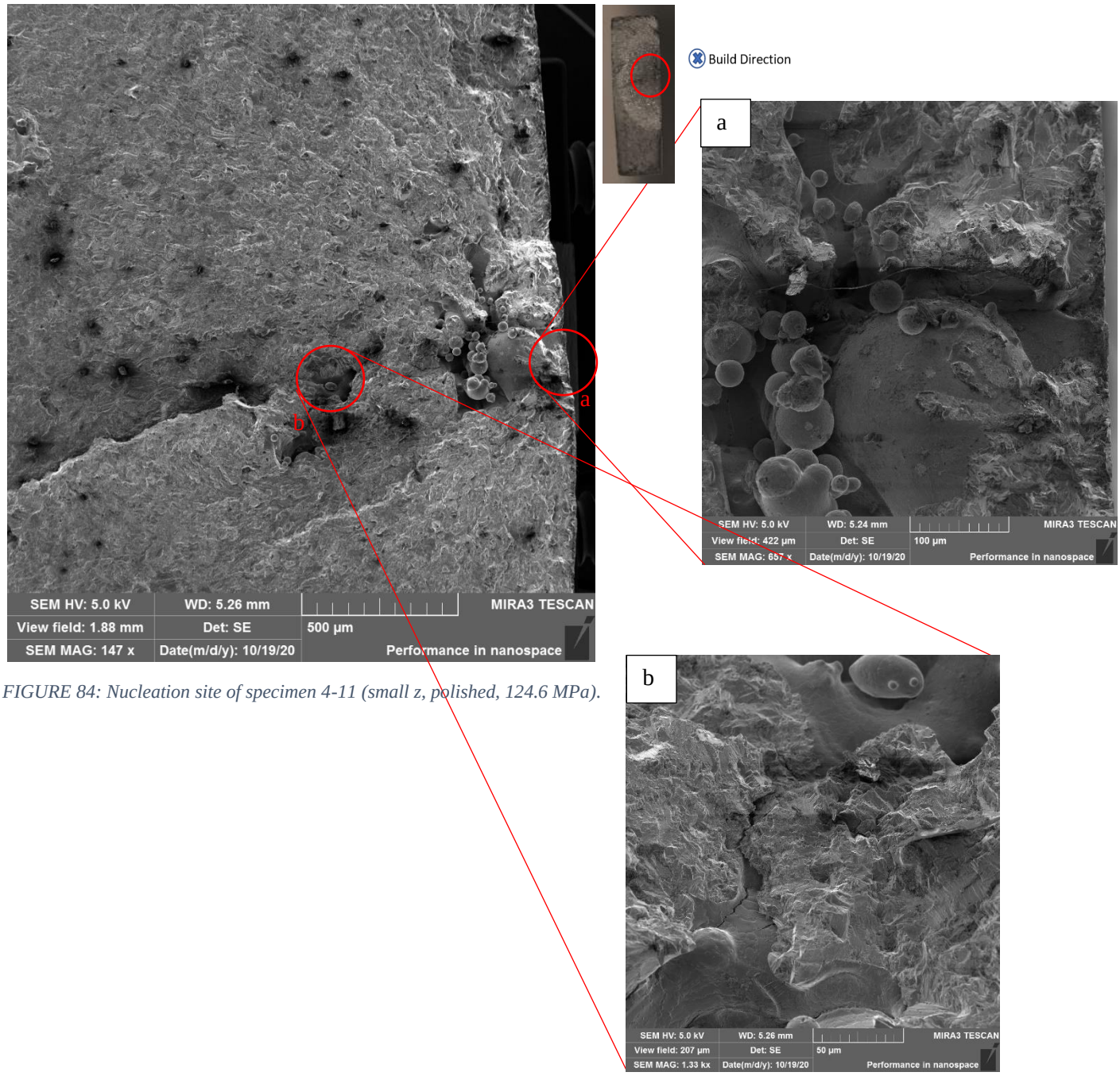

FIGURE 84: Nucleation site of specimen 4-11 (small z, polished, 124.6 MPa).

4.5.5. Build 5

Build 5 presented higher fatigue performance for the polished z specimens compared to build 4, but very similar strength between small z as-is and small xy as-is. Two specimens from small z build direction and one small xy were imaged to investigate the increase in fatigue performance for the polished small z and the matching results for the as-is specimens.

FIGURE 85 shows specimen 5-12 (small z, as-is, 131.1 MPa). Overall, this specimen presents reduced lack-of-fusion defects, but a high number of carbides can be seen (FIGURE 85a,b,c). Specimen 5-9 (small z, polished, 168.8 MPa) shows more of these carbides (FIGURE 86a,b). No major lack-of-fusion defects can be observed in this specimen, proving once again that significant empty voids are more detrimental to HCF strength than carbides.

As for the xy specimen 5-17 (small xy, as is, 110.8 MPa) shown in FIGURE 87, lack-of-fusion defects were found on the narrow edge that was connected to the build plate by supports. Although these edges were polished, the size and depth of the empty void in FIGURE 87a (>250µm) was the underlying feature behind fracture. FIGURE 87b shows again the presence of a carbide, although for this specimen it was not found to be the “killer” defect feature.

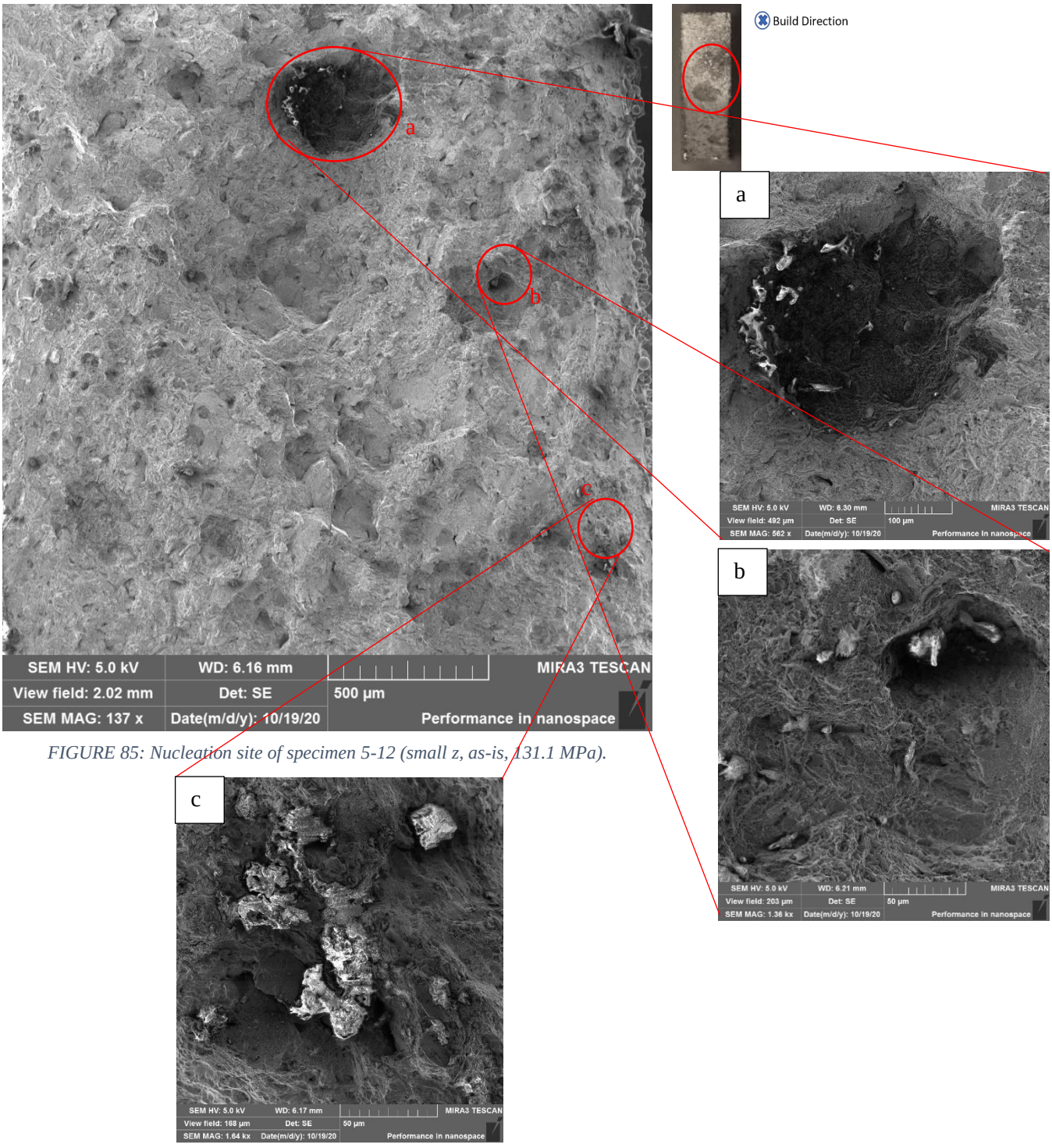

FIGURE 85: Nucleation site of specimen 5-12 (small z, as-is, 131.1 MPa).

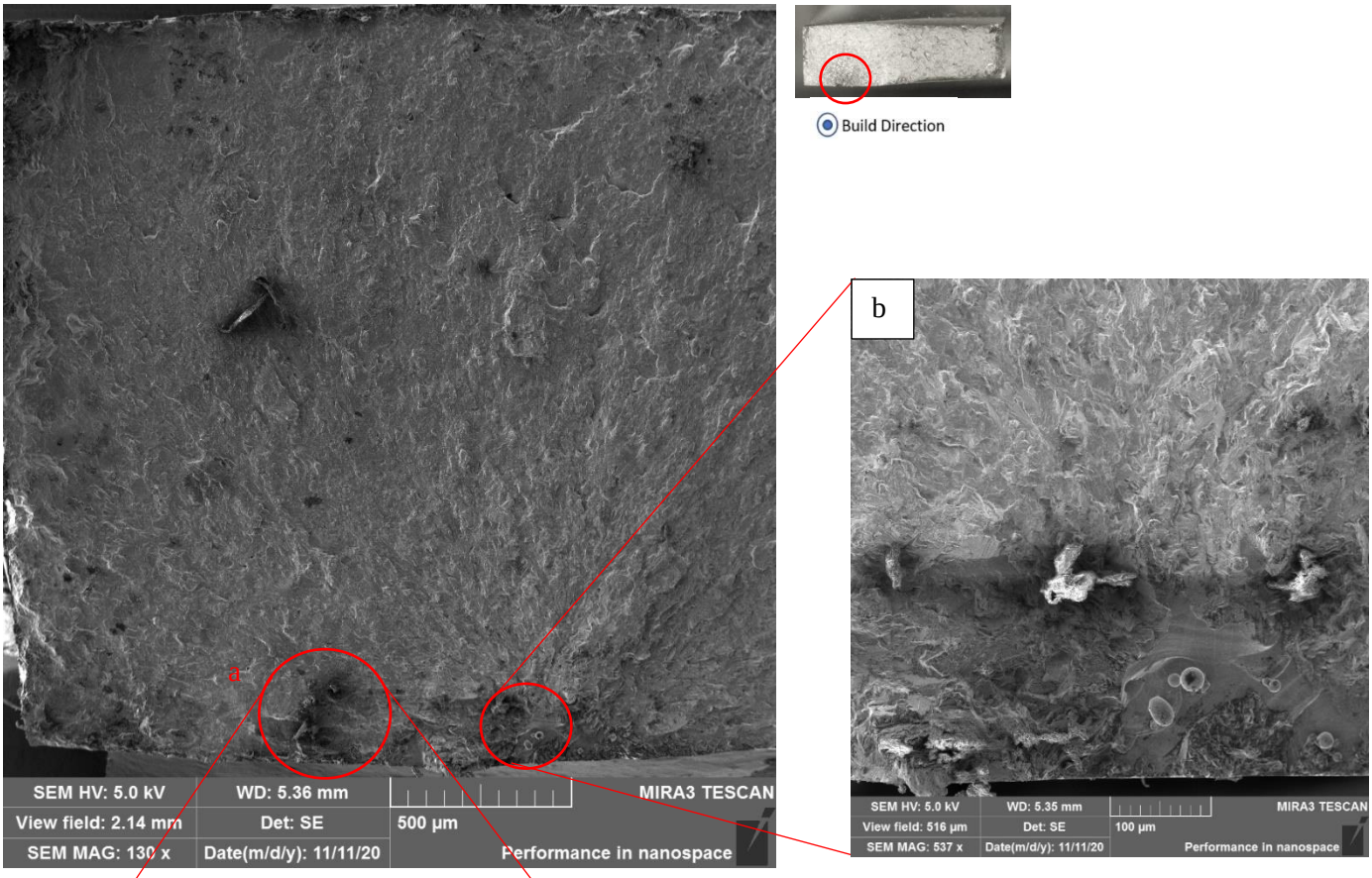

FIGURE 86: Nucleation site of specimen 5-9 (small z, polished, 168.8 MPa).

\

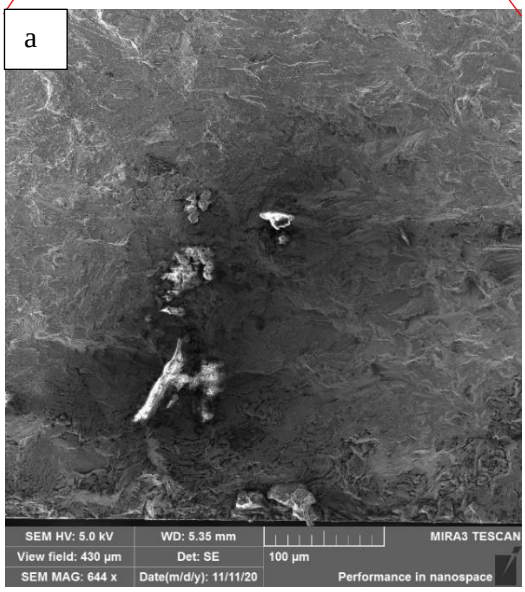

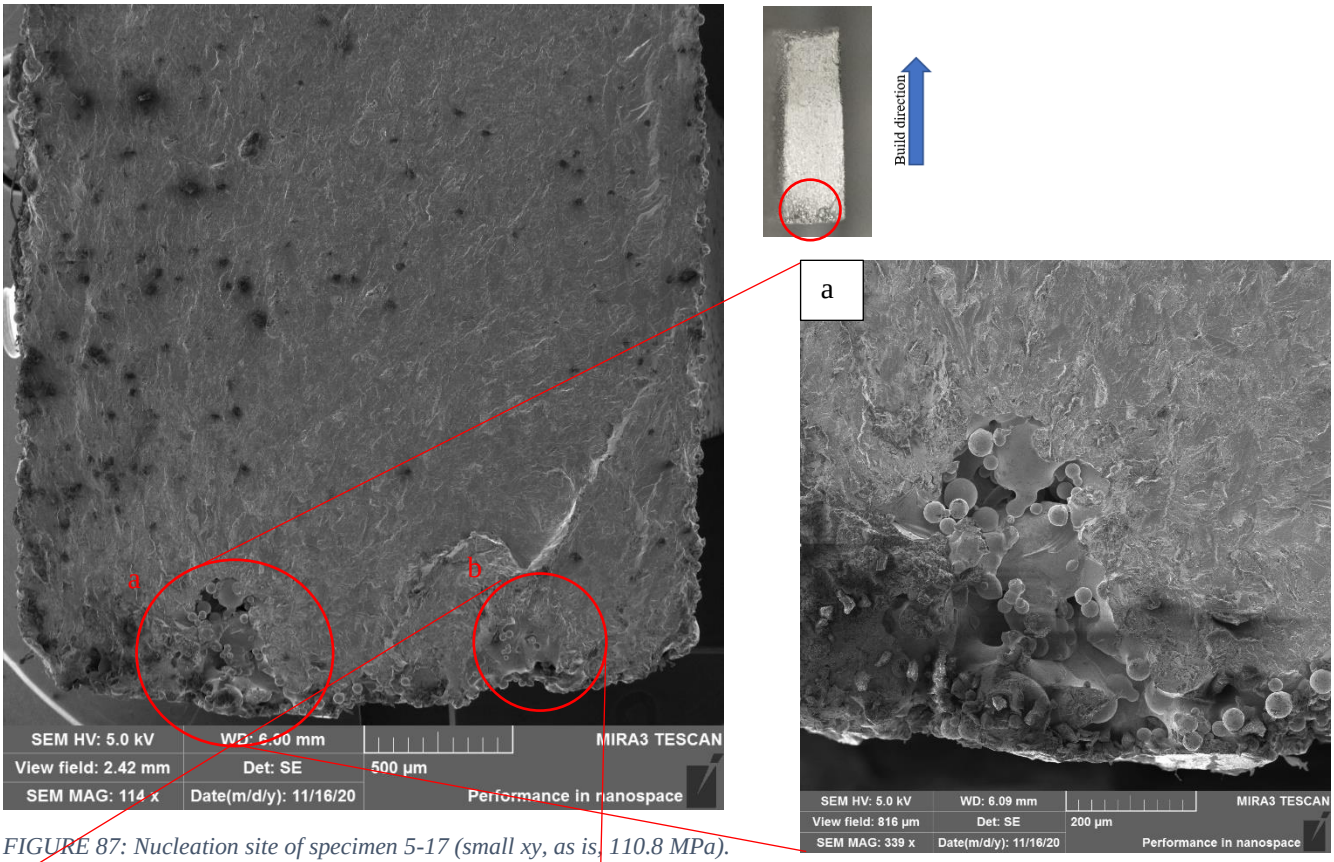

FIGURE 87: Nucleation site of specimen 5-17 (small xy, as is, 110.8 MPa).

4.5.6. Build 6

Build 6 small z specimens presented good microstructure, and reduced carbides in the fracture surface. Unlike the rest of the builds (with the exception of the extremely low fatigue strength of build 7), build 6 small z specimens were the only ones where the strength of the as-is matched the polished. In fact, the results came out to be slightly favorable to the as-is specimens.

FIGURE 88 shows the fracture surface of specimen 6-8 (small z, as-is, 150.7 MPa). No large voids can be observed except for the nucleation site where a relatively small empty void can be seen (≈200µm).

The same feature found in the previous build (specimen 5-17) was present in FIGURE 89 (specimen 6-13, small xy, as-is, 110.5). This large lack-of-fusion void (>250µm) could explain the reduction in fatigue performance of small xy vs small z for the build.

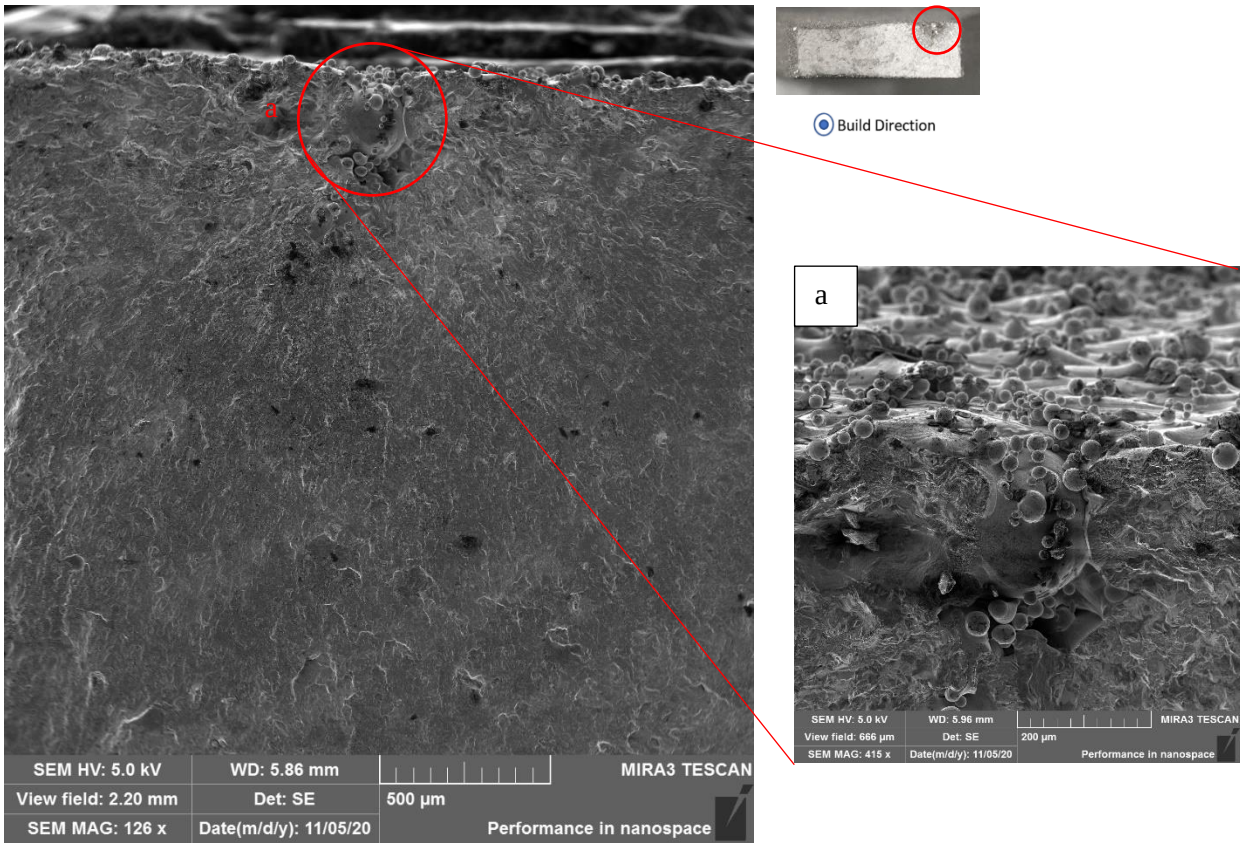

FIGURE 88: Nucleation site of specimen 6-8 (small z, as-is, 150.7 MPa).

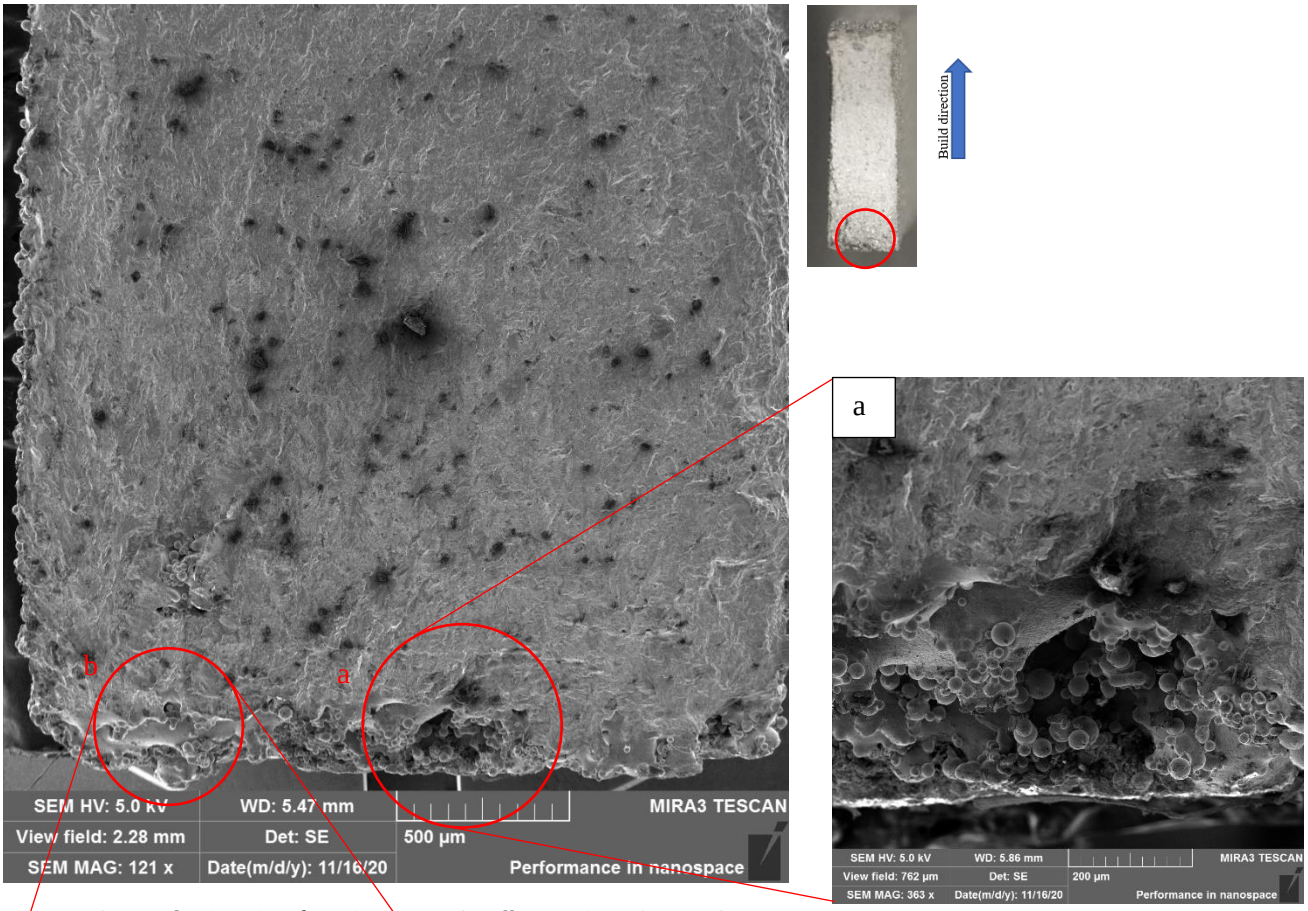

FIGURE 89: Nucleation site of specimen 6-13 (small xy, as-is, 110.5 MPa).

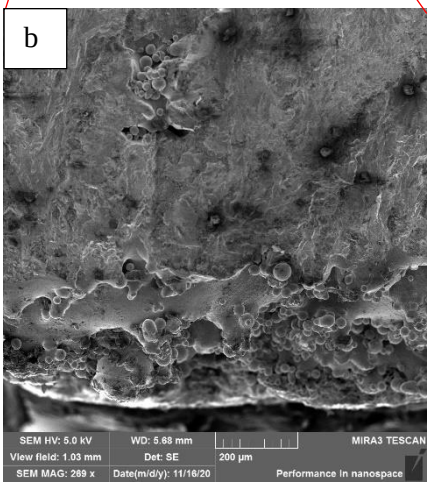

4.5.7. Build 7

As seen in the fatigue results section (section 5.1), build 7 presented extraordinarily lower fatigue than the rest of the builds. One specimen (7-13, small xy, as-is, too low fatigue strength) from this build was imaged (FIGURE 90). The poor microstructure can be readily perceived with the naked eye (FIGURE 90). This particular specimen, apart from having extreme porosity, was the only specimen that failed by interlayer delamination. The SEM image shows the delaminated layer perpendicular to the build direction. The exact origin of the fracture is not clear, as it could have happened in the perpendicular planes simultaneously. The weak bonding between layers, coupled with high porosity within the specimen was the reason behind the low fatigue performance of the build. The same poor microstructure was observed in the rest of the tested specimens from build 7.

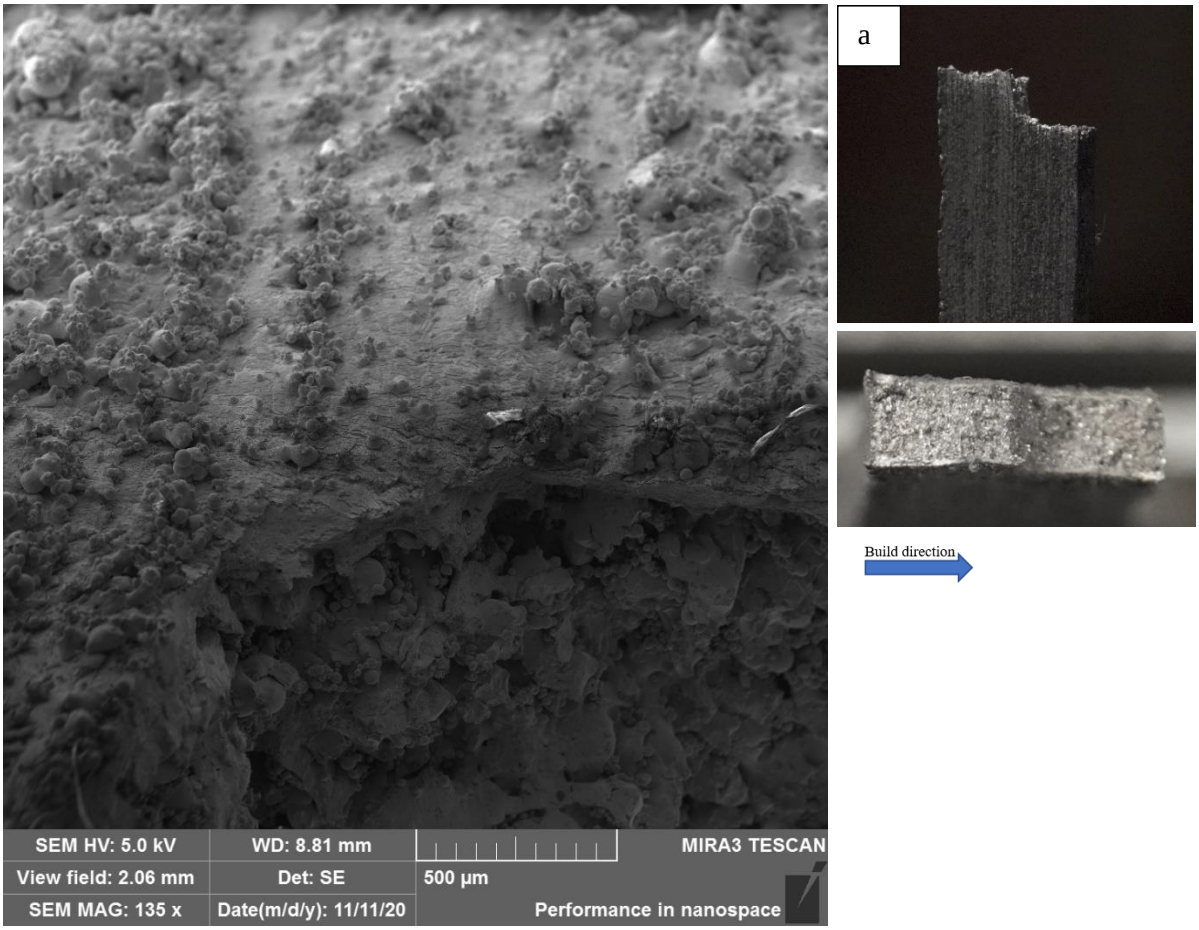

FIGURE 90: Nucleation site of specimen 7-13 (small xy, as-is, too low fatigue strength).

4.5.8. Build 8

Although build 8 exhibited better fatigue strength than the previous build 7, build 8 had a relatively low HCF compared to all of the other builds. FIGURE 91 shows the fractured surface of specimen 8-13 (small xy, as-is, 45.8 MPa), revealing large and numerous lack-of-fusion voids (>300µm). A high variability was found between small xy and small z. This was attributed to the reduced lack-of-fusion defects found on the fracture surfaces from the small z specimens. Polishing was also found to play a large role within the small z specimens, consistent with the fact that surface finish will play a bigger role when as-is roughness conditions are sub-optimal (roughness and internal porosity).

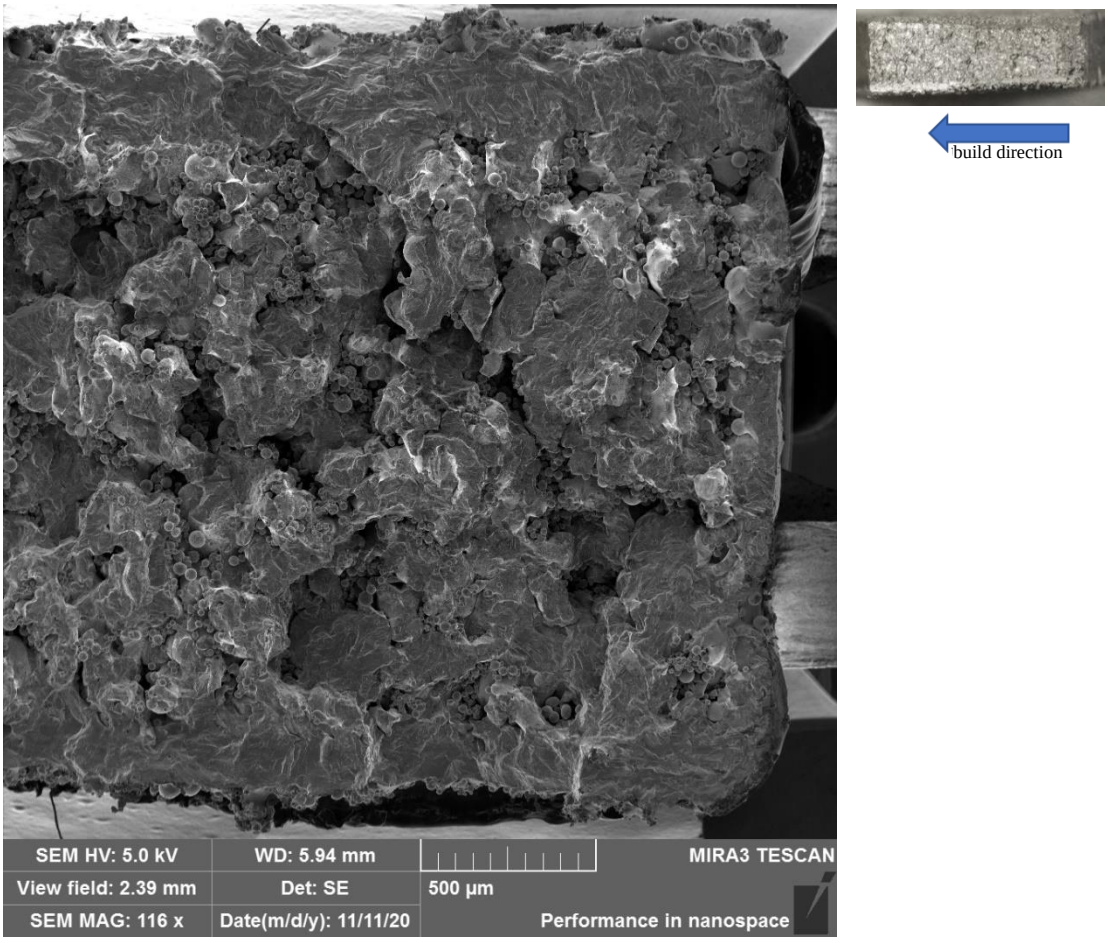

FIGURE 91: Fracture surface of specimen 8-13 (small xy, as-is, 45.8 MPa).

4.5.9. Build 9

Build 9 presented a good fatigue resistance for small z specimens in both as-is and polished conditions, but reduced strength for small xy specimens. Two specimens in the as-is condition from both build directions were imaged. FIGURE 92 shows the fracture surface of specimen 9-7 (small z, as-is, 162.8 MPa), revealing a relatively good microstructure except the large void (≈300µm) that can be seen in the top right part of the image.

On the other hand, specimen 9-14 in FIGURE 93 (small xy, as-is, 79.4 MPa) shows a larger amount of these defects, which could explain the high variability of z vs. xy specimens. No polished specimen was imaged as the difference between as-is and polished small z specimens was consistent with the average performance improvement when surface roughness was reduced by polishing.

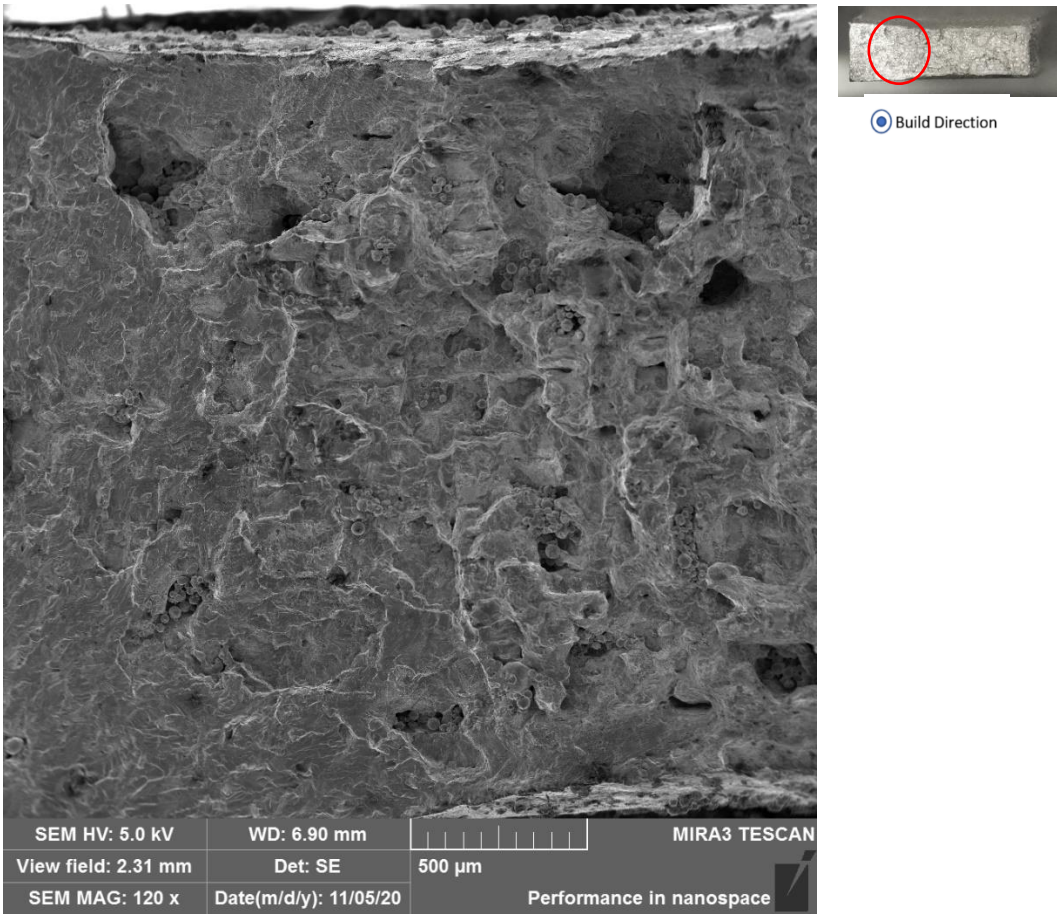

FIGURE 92: Nucleation site of specimen 9-7 (small z, as-is, 162.8 MPa).

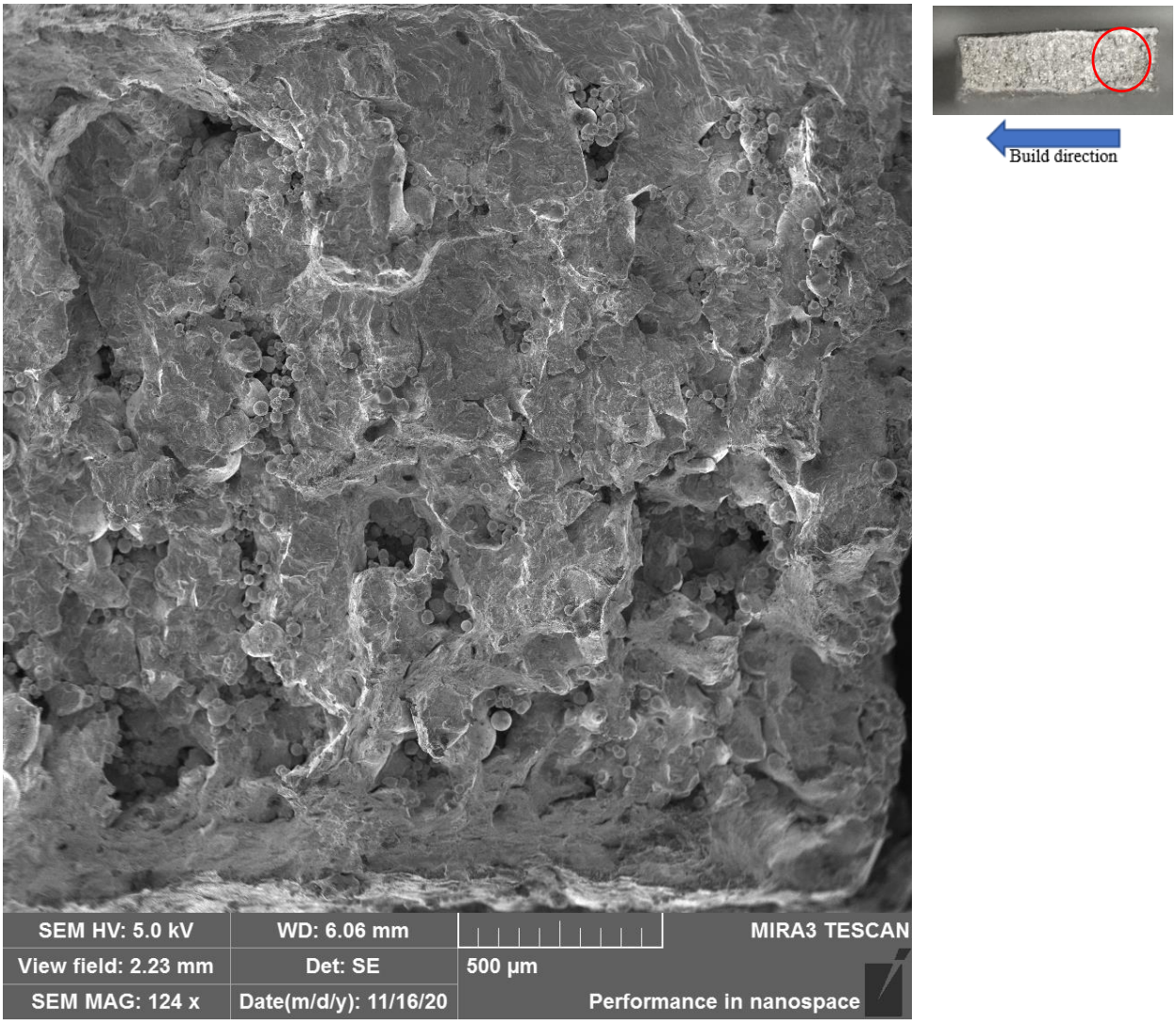

FIGURE 93: Nucleation site of specimen 9-14 (small xy, as-is, 79.4 MPa).

4.5.10. Build 11

This build presents one of the best microstructures of all of the builds. FIGURE 94 shows specimen 11-7 (small z, polished, 229.2 MPa), revealing a very good microstructure where the river marks clearly point towards the initiation site. The carbide in FIGURE 94a was found to be the reason behind fatigue crack nucleation for this specimen. Another two small z specimens were fatigue tested, with contradicting results. Specimen 11-10 (small z, as-is, 140.9 MPa) shown in FIGURE 95 had considerably lower strength compared to the polished specimen, much more than expected. FIGURE 95a shows a feature that looks like a deep void on the surface. However, specimen 11-12 (small xy, as-is, 163.9 MPa) which was not examined in the SEM had a considerably higher fatigue strength. This suggests that the previously described defect was responsible for the outlier of the small z specimens.

Furthermore, FIGURE 97 shows the fracture of specimen 11-13 (small xy, as-is, 105.3 MPa). The SEM image reveals the presence of a large lack-of-fusion defect towards the bottom narrow side where the supports were introduced during manufacture. From there, the fracture initiated and propagated through the crack and caused failure of the specimen. Once again, large, concentrated lack-of-fusion voids will have detrimental effects and punish the fatigue performance of the specimen, causing a significant difference between xy and z specimens.

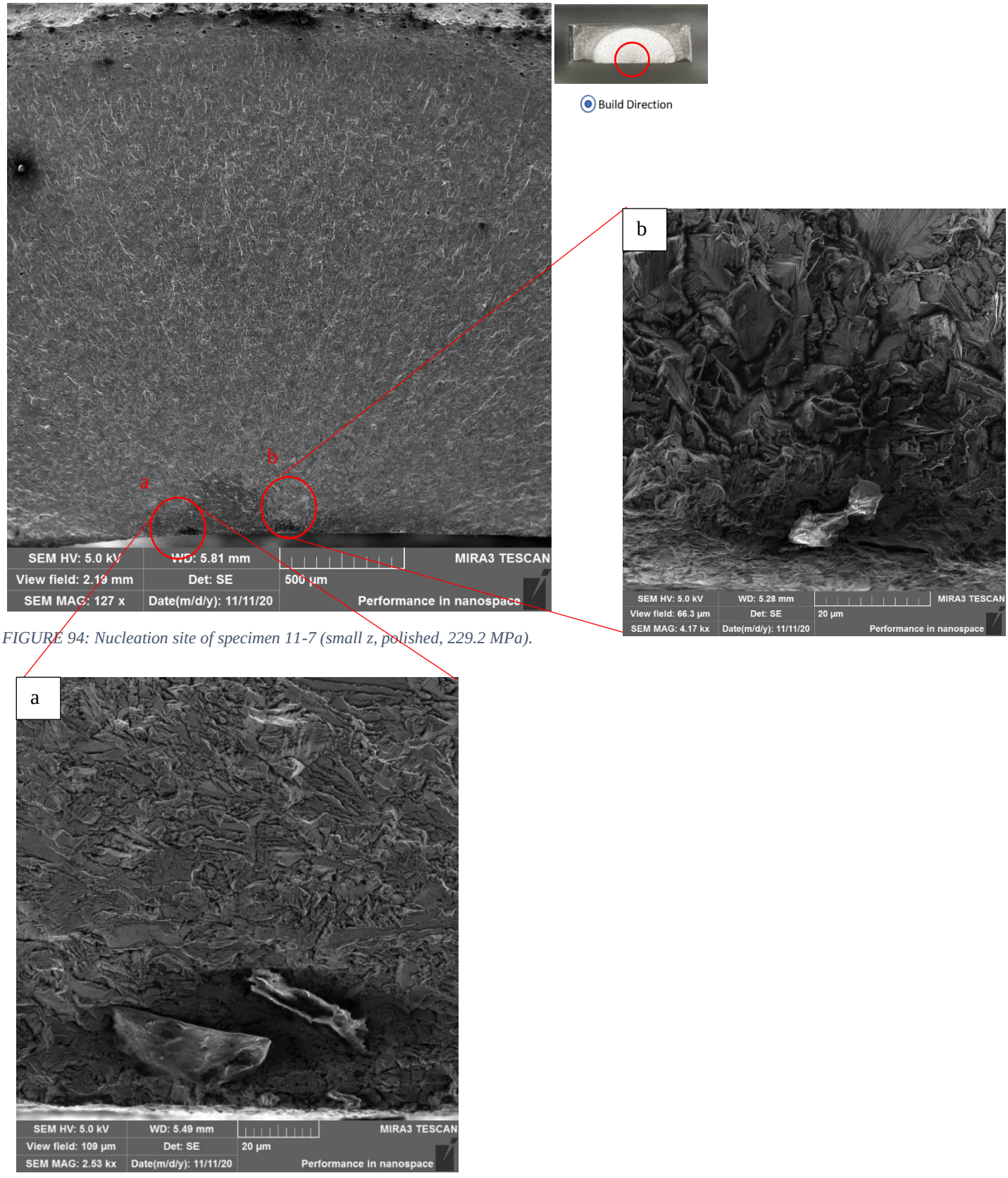

FIGURE 94: Nucleation site of specimen 11-7 (small z, polished, 229.2 MPa).

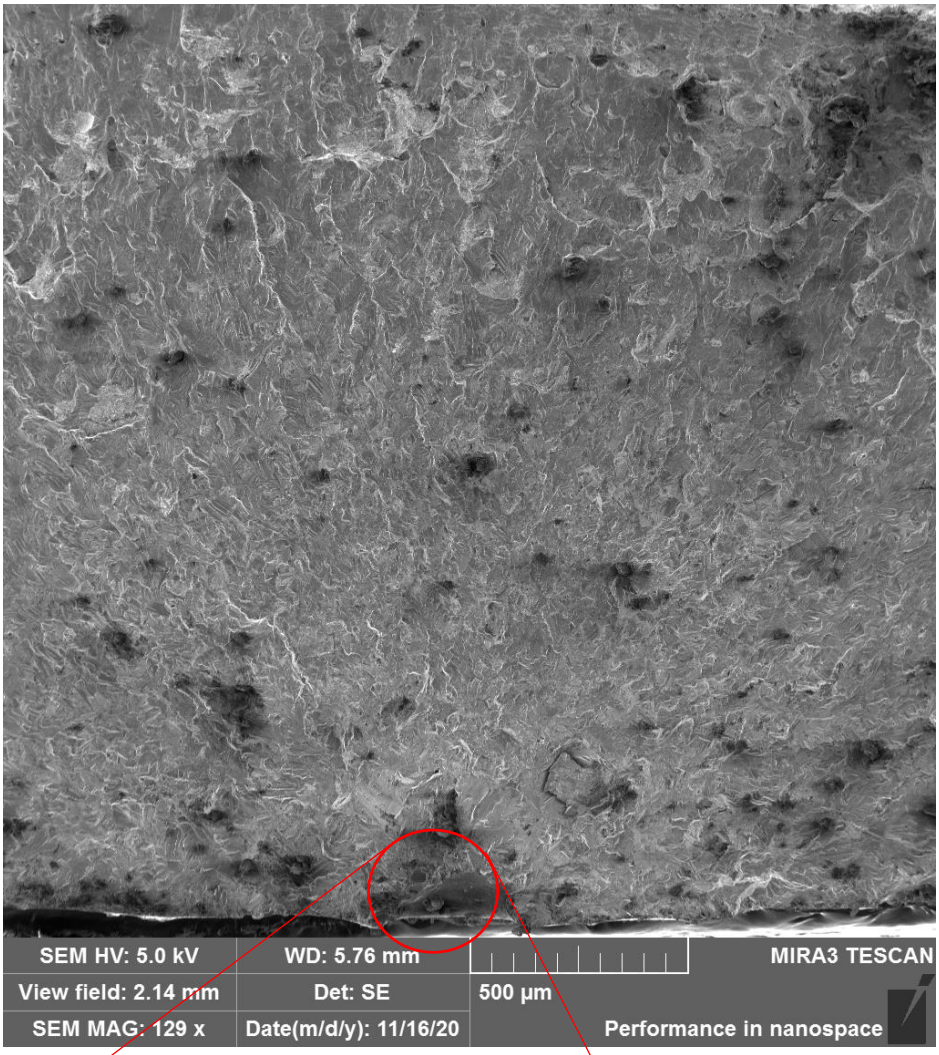

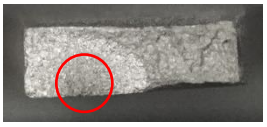

Build Direction

FIGURE 95: Nucleation site of specimen 11-10 (small z, as-is, 140.9 MPa).

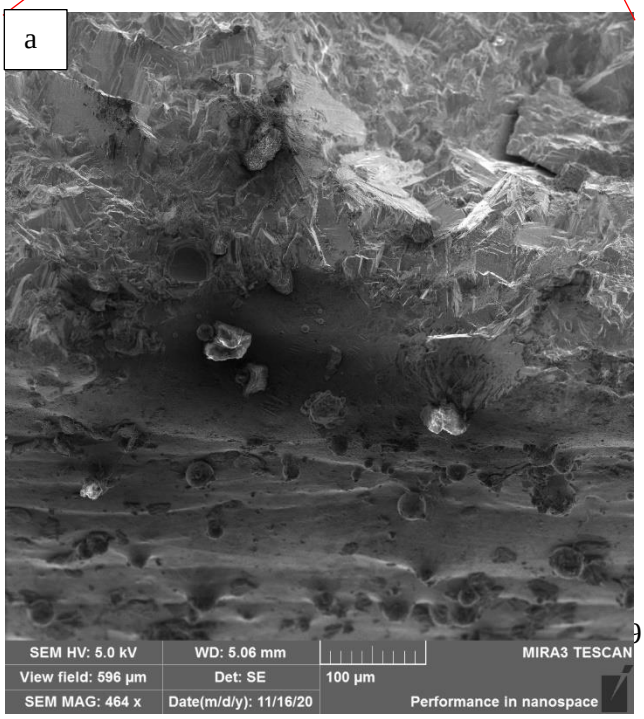

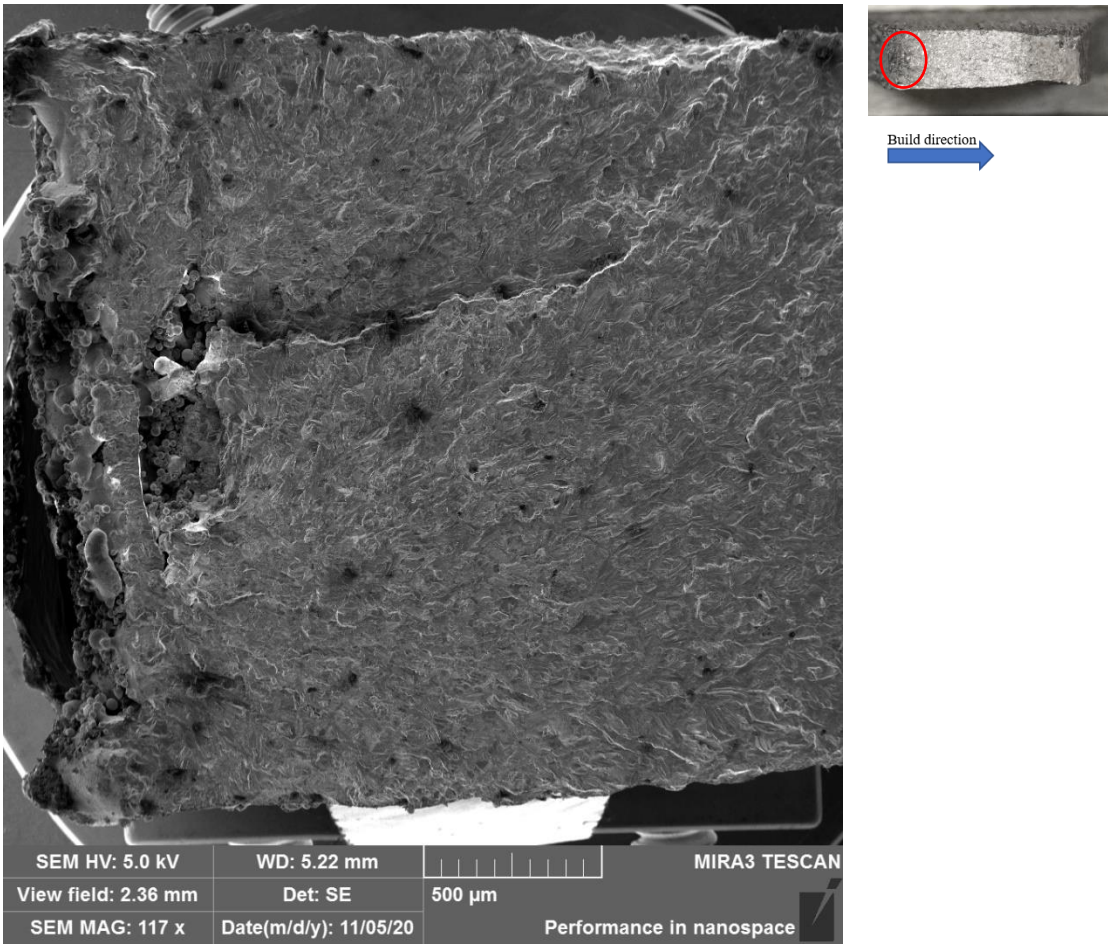

FIGURE 96: Nucleation site of specimen 11-13 (small xy, as-is, 105.3 MPa).

4.6. Surface roughness results

Comparisons of the Sa values for the small as-is z specimens are shown FIGURE 97. The Sa values ranged from 13-16 μm for most of the surfaces in the gage section for the specimens built on the Concept M2 (builds 1-6). For reference purposes, the Sa value obtained for polished specimens was <2 μm, approximately 80% less rough. The Sa values for the specimens built on the Renishaw were generally lower, particular on the wide sides, where the Sa values ranged from 5-6 μm. The narrow sides were noticeably rougher than the wide sides for the Renishaw, though not any rougher than the Concept M2.

FIGURE 98 summarizes the surface roughness results for the small xy specimens. The Sa value for the wide faces was similar for both machines, Sa < 14 μm for most builds, with the exception of build 4. The value for the Renishaw was slightly lower than the Concept M2 for the wide faces. As for the narrow sides, the narrow side towards the bottom was the roughest, Sa > 30 μm for all builds except build 1. The values for the Renishaw were similar to the Concept M2 for the narrow side towards the top (Sa ≈30 μm), but considerably higher for the narrow side towards the bottom, where the Sa values ranged from 32-53 μm. Overall, the roughness for the narrow sides is considerably higher than the wide sides, with the narrow side towards the bottom being the worst.

Finally, FIGURE 99 shows both specimen orientations on the same plot. The roughness of all wide sides was higher in value for the Concept M2 builds (Sa >10 μm). The Renishaw yielded better roughness for the wide sides (Sa < 5 μm). However, the roughness of xy specimens on the narrow sides was consistently worse than that of the small z specimens, by a large amount (ΔSa > 10 μm). This difference was more extreme for the Renishaw than the Concept M2. Moreover, the difference in roughness (ΔSa) between wide and narrow sides is also more prominent for the Renishaw than the Concept M2 builds. In some cases, the increase in Sa from the wide to the narrow > 30 μm.

Some values of roughness are missing (for instance, build 2 results in FIGURE 97) because the roughness study was initiated after the HCF testing was performed and we learned that the roughness values obtained after fatigue testing were different from before, and hence not directly compariable. Nevertheless, a large number of specimens were tested so these results do provide a comprehensive overview of the Sa values for the available builds and all sides.

From these results, we can observe that the Sa values do not directly correlate to the fatigue performance. For example, consider the z-direction specimens, FIGURE 97, the fatigue strength of build 4 was much lower than builds 1 and 3, yet it had lower surface roughness. Furthermore, builds 7 and 8 had the worst fatigue lives and had better surface roughness than builds 1-6 for small z specimens. The fact that the Sa value is consistently worse for narrow sides may explain why fatigue cracks often nucleated on the narrow sides (TABLE 19). Nevertheless, although the roughness results seem to point towards the narrow side 1 of the z specimens, no clear trend was seen between the visual inspection and the measured roughness, as the fatigue cracks formed mostly from one of the narrow sides indistinctively.

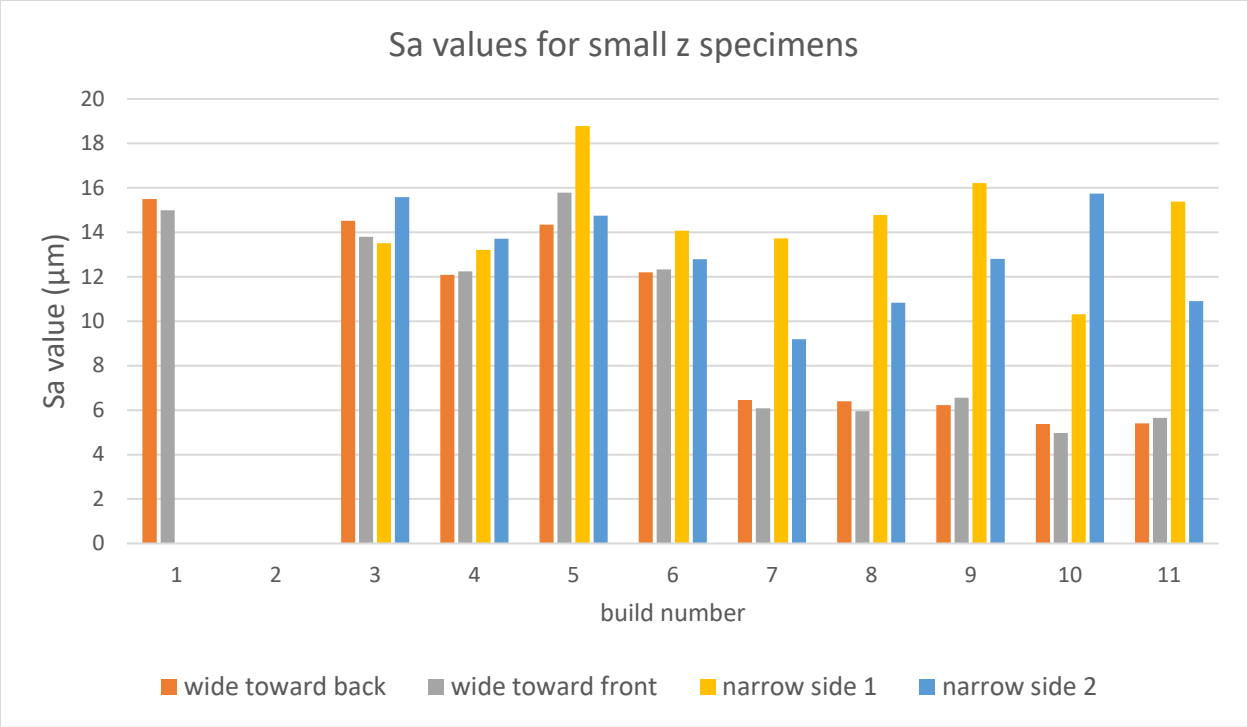

FIGURE 97: Sa values in microns for all sides of small z specimens.

The surface roughness of the small xy specimens shown in FIGURE 98 weakly correlate to the fatigue strengths. Good performing builds (1, 2, 3, 6, 10, 11) had lower Sa values on the wide sides (Sa < 14 µm) than worse performing builds (4, 5, 9) (Sa > 14 µm). This could be due to the fact that surface defects were associated with fatigue crack formation for small xy specimens, while the majority of the "killer" defects in the z specimens occurred as a result of internal features like lack-of-fusion defects and carbides described in the previous section. Similar pattern within each build was observed, where in this case the narrow side towards bottom is the side with the greatest roughness, in many cases ΔSa >10 µm of difference between sides. TABLE 19 does show a tendency of the small xy specimens to form fatigue cracks on the narrow side towards the build plate (i.e., bottom side). This is in line with the previous statement that roughness drove a larger amount of fractures in small xy than small z due to a larger Sa value for this group of specimens. However, a low Sa value for builds 7 and 8 indicates that fatigue is not necessarily correlated with Sa values when internal defects are the sites where fatigue cracks are forming. Although surface finish is an important factor when determining fatigue, other roughness values such as Sv (maximum depth) could be more significant when predicting performance as shown in FIGURE 95.

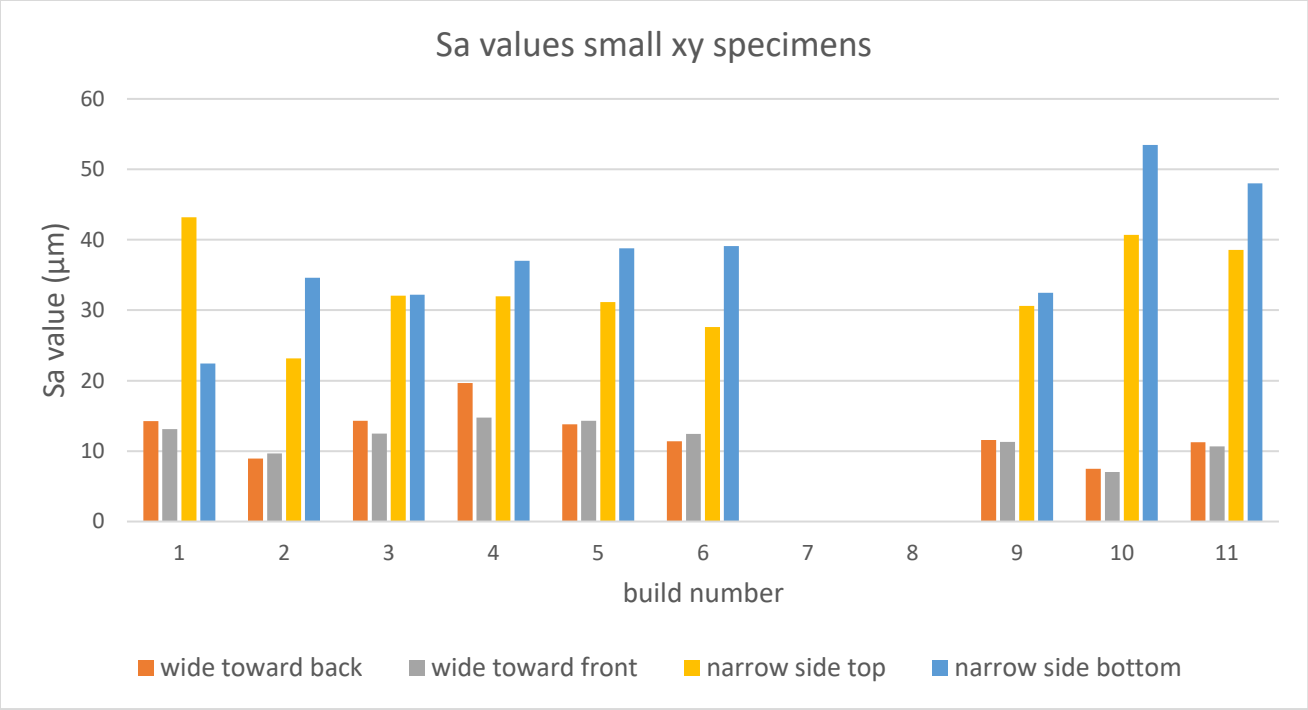

FIGURE 98: Sa values in microns for all sides of xy specimens.

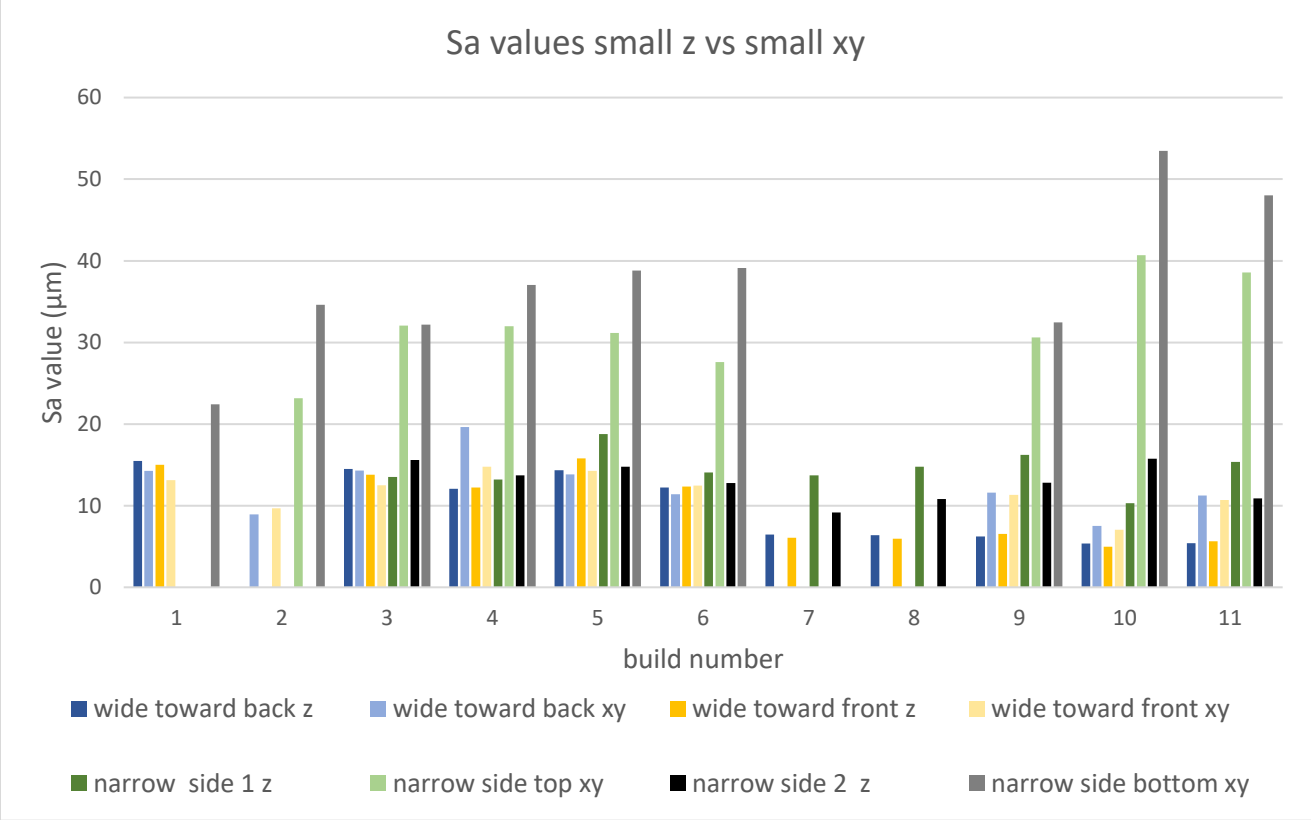

FIGURE 99: Sa values in microns for both xy and z specimens.

4.7. Estimation of stress-life curves for each build

Using the fatigue strength results, stress-life (SN) curves are estimated for each build and compared to SN curves of additively manufactured IN625 reported in the literature. The SN curves are plotted for fully-reversed loading using the Walker equation (eq. 15) with $\gamma = 0.42$. The SN curves for the small z specimens are separated into two plots (FIGURE 100 and FIGURE 101) in order to avoid crowded plots. This is also present in FIGURE 102, where the strengths of builds 7 are also not seen. All plots include the baseline wrought estimate from MMPDS-14 [58], and the additively manufactured IN625 from Koutiri et al. [13] and Anam [39]. Koutiri et al. results are only shown on the xy plot, as this author only tested fatigue specimens in this direction. Alternatively, Anam results are separated as this author tested specimens in both directions.

The MMPDS-14 data is standard benchmark used for wrought, annealed and unnotched IN625. The fatigue data from the rolled plate is comparable to the MMPDS-14 data. Small z specimens (FIGURE 100 and FIGURE 101) from builds 3 and 11 in the polished conditions offered the closest tensile and fatigue properties compared to both wrought curves.

It is relevant to note that the results obtained by Anam showed the greatest fatigue strength even better than the data for wrought material in all orientations. Furthermore, Anam obtained better results for xy (FIGURE 102) than z specimens, which is the opposite of what was obtained in this study. Anam attributes this anisotropic behavior to a higher porosity found in z samples, caused by the increase in probability of obtaining lack-of-fusion defects within layers. However, if these defects are absent, z specimens should obtain better fatigue properties due to favorable columnar grain distribution. For z specimens, the crack grows perpendicularly to the grain growth, making propagation more difficult. Alternatively, the crack growth for xy specimens is parallel to the grain orientation. However, columnar crystallographic grains were only observed in the Concept M2 specimens. The HIP process resulted in recrystallization for the Renishaw specimens, meaning that there should have been less microstructure anisotropy for the Renishaw. However, the fatigue results show more anisotropic behavior for the Renishaw than the Concept M2. This suggests that the features of the crystallographic grain size and morphology did not influence the HCF strength for the specimens tested here; instead, the HCF strength was mainly controlled by either lack-of-fusion defects or carbides, with added influence of the stress concentrations associated with increase in surface roughness.

As seen on the fracture surfaces, small z specimens obtained in many cases had fewer lack-of-fusion defects than the small xy specimen. One possible reason for the increase in fatigue strength observed by Anam is the specimen geometry used in his investigation. The fatigue tests used an hourglass test section with minimum diameter of 4 mm. This specimen type reduces the volume of material experiencing the greatest cyclic stress to a plane. When fatigue strength is controlled by the weak-link defects, this test specimen will have higher fatigue strength than one that uses a uniform gage section that all of the other investigations reported here have used.

Koutiri et al. results are very similar to the results gathered for the higher strength small xy builds (FIGURE 102). This author did obtain slightly better performance for the polished specimens, although not as much as expected. The author explains that this is due to similar sized defects

located further away from the edges, known as “killer defects”. These were found in both polished and as-is specimens. This was the case for some builds from this project specially for the worse performing small z builds where internal defects were the driving mechanism behind failure (see builds 4 and 6 from FIGURE 100).

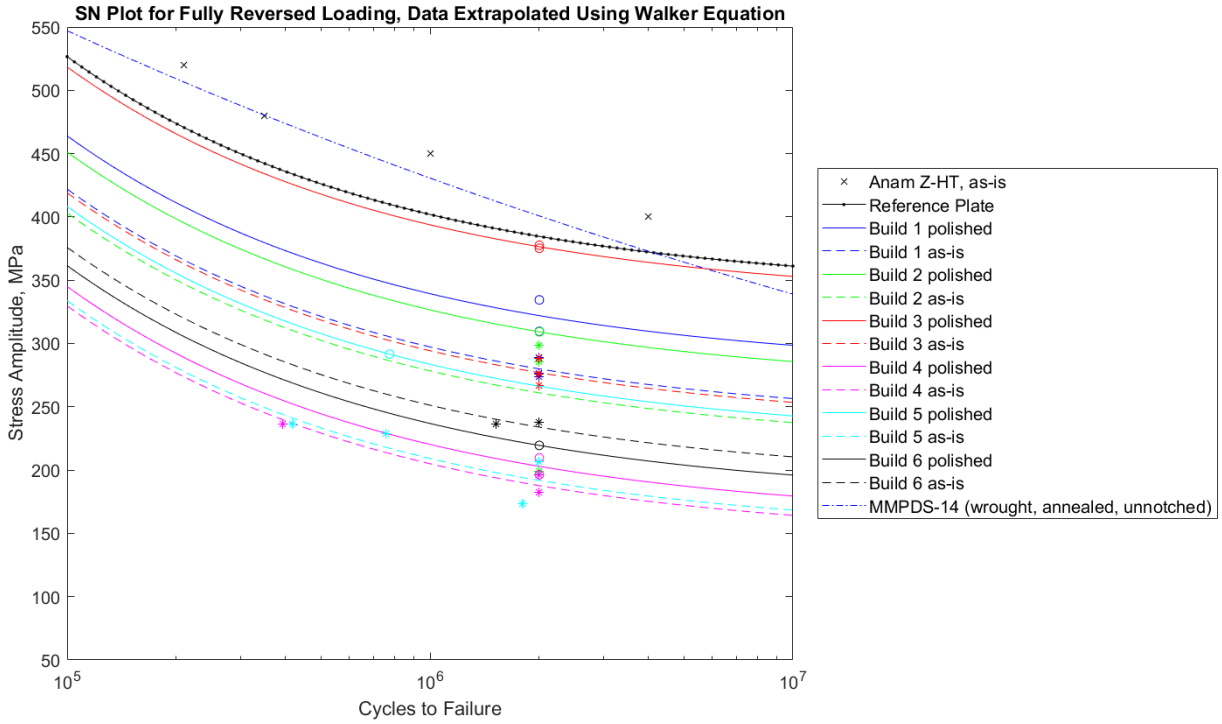

FIGURE 100: SN plot for fully-reversed (R=-1) loading using Walker equation ($\gamma = 0.42$) for small z, builds 1-6.

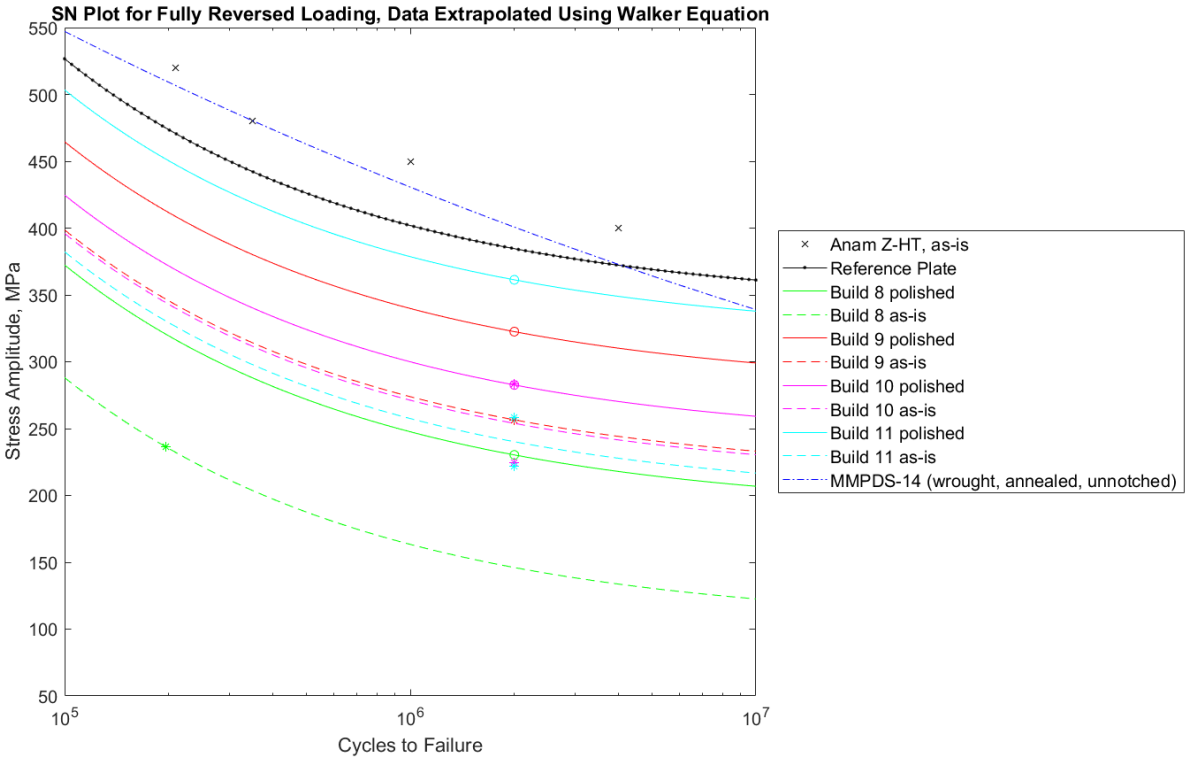

FIGURE 101: SN plot for fully-reversed (R=-1) loading using Walker equation (γ = 0.42) for small z, builds 7-11.

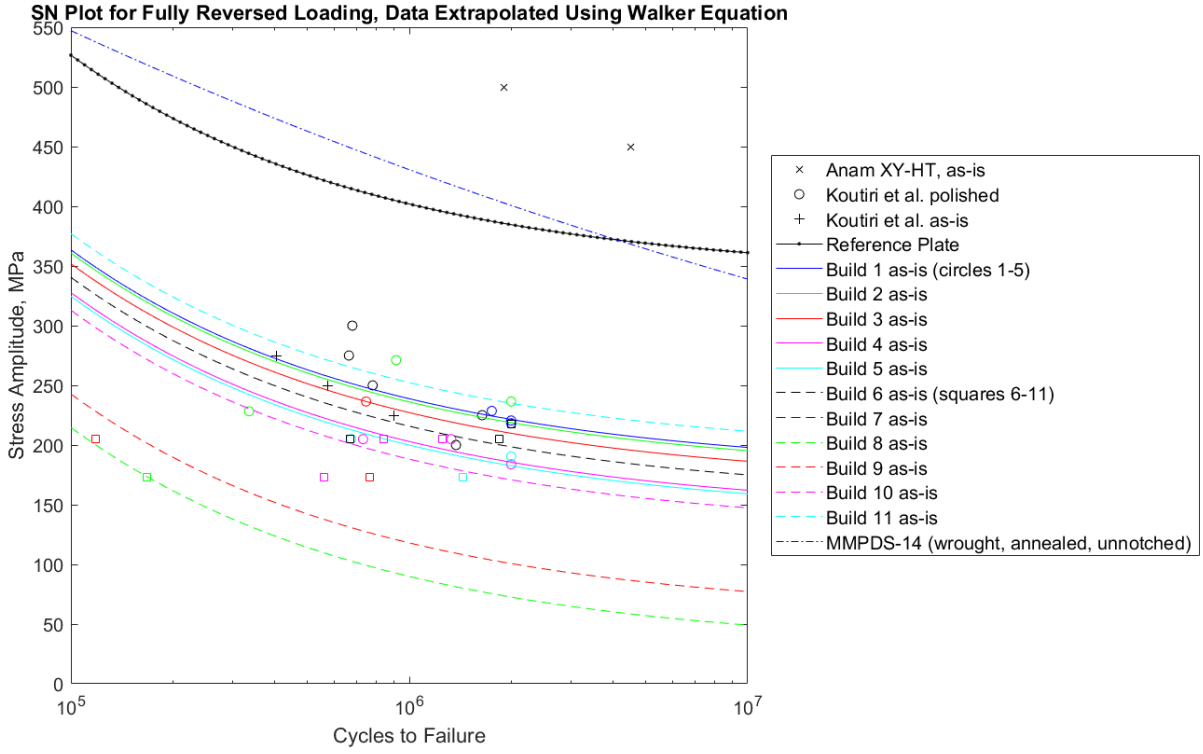

FIGURE *102*: SN plot for fully-reversed loading using Walker equation (γ = 0.42) for small xy, builds 1-11.

4.7.1. Estimated fully-reversed (R=-1) life relationships for all builds

The SN curves for all builds is given by

$$N_f = 4.78 \times 10^9 \left(\sigma_{ar} - \left(Build_{xpar}\right)\right)^{-2.06} \qquad \text{[Eq. 17]}$$

where σ_a has units of MPa and is generally applicable for fatigue lives between 10^5 and 10^7 cycles. TABLE 20 and TABLE 21 contain the parameters for the small z and small xy specimens, respectively, that can be used to obtain the fully-reversed curves for all builds except for 7 which had very low fatigue strength.

TABLE 20: build parameter ($Build_{xpar}$) for small z specimens (eq. 17).

Build no.	Polished (MPa)	As-is (MPa)
1	277	235
2	263	216
3	331	233
4	157	142
5	221	147
6	175	188
7	N/A	N/A
8	186	102
9	277	212
10	238	216
11	216	195

TABLE 21: build parameter ($Build_{xpar}$) for small xy specimens (eq. 17).

Build no.	As-is (MPa)
1	176
2	174
3	165
4	141
5	138
6	154
7	N/A
8	28
9	98
10	126
11	190

5. CONCLUSIONS

The results show that the high cycle fatigue (HCF) performance can be obtained for L-PBF IN625 for different combinations of processing parameters and microstructures using a fatigue step test method. The fatigue step test was found to have considerable utility for obtaining fatigue information efficiently. Another application of the step test method is the evaluation of one-of-a-kind witness specimens built adjacent to components on the build plate that can be used for quality assurance and as data for digital threads. This work showed the high variability of HCF strength with different internal microstructures and surface roughnesses. The data gathered shows a complex relationship between processing parameters, structure, and fatigue life. Considerable structure and property differences between two different L-PBF machines using nominally the same processing conditions was observed suggesting that the type of machine will exacerbate variability. Volumetric energy density (VED) has been found to be the stronger indicator for high cycle fatigue performance in the case of small z specimens, as the highest energy densities exhibited lower porosity and higher fatigue strength. The large amount of lack-of-fusion "killer" defects suggests that the volumetric energy density used was not large enough in the DoE. A higher energy density should be used to mitigate this defect, but without incurring in too high VED values to avoid keyholing defects. HIPping was found to not reduce porosity completely particularly when lack-of-fusion defects were widespread, making optimal choice of processing parameters more important when extending the fatigue life of specimens.

It was shown that HCF life does not necessarily correlate with yield strength. The fatigue strength weakly correlated with ductility for z specimens, but this correlation was not apparent in the xy build direction. However, xy specimens did weakly correlate with yield strength, although the reliability of these results can be questioned due to the low amount of tensile xy specimens tested. The yield strength was clearly not sensitive to processing defects, except when extreme porosity was present.

Several processing influences were studied under HCF. The surface roughness was shown to play some role as polishing the surfaces was found to increase the fatigue longevity for the vast majority of builds particular for the small z HCF specimens. The increase in fatigue strength with polishing was more prominent for the builds with fewer defects and higher fatigue strengths, for which the internal defects did not override the surface roughness effect. The most relevant result of this study is the anisotropy of the strengths observed between z and xy specimens, with the z specimens exhibiting higher fatigue strength than the xy in the same build. This is contrary to what was reported in previous work, as z specimens were found to have larger concentrations of lack-of-fusion defects due to the larger number of layers perpendicular to the build direction.

The majority of the fatigue crack formation sites, i.e., the "killer" defects, were associated with lack-of-fusion defects, mostly near a surface. In specimens where the lack-of-fusion defects were minimal, fatigue cracks tended to form at sites where several carbides were close together and acting as stress risers during HCF testing, also typically close to a surface. However, high amounts of lack-of-fusion defects were considerably more detrimental than the presence of carbides which also tended to be smaller in size than the porosity associated with the lack-of-fusion defects. It was also found that when there is a higher the concentration of lack-of-fusion defects, there is a higher probability of the fatigue crack forming internally and hence a less dependence of HCF strength to the surface finish. Overall, the observed porosity was build location dependent in both xy and z specimens.

The surface roughness value Sa did not show a correlation to fatigue performance. The fatigue crack nucleation sites in the majority of the cases were located on the narrow sides where the Sa value was considerably higher. However, some poor performing builds with high porosity had lower Sa values than better performing builds with lower porosity, suggesting the surface roughness alone cannot provide a definite indicator of fatigue performance. Therefore, future work should analyze other roughness parameters such as Sv, or maximum depth of the surface, as large depressions found on a couple of the surfaces were sites where fatigue cracks formed.

APPENDIX

A.1 Stress-strain diagrams

Rolled Sheet

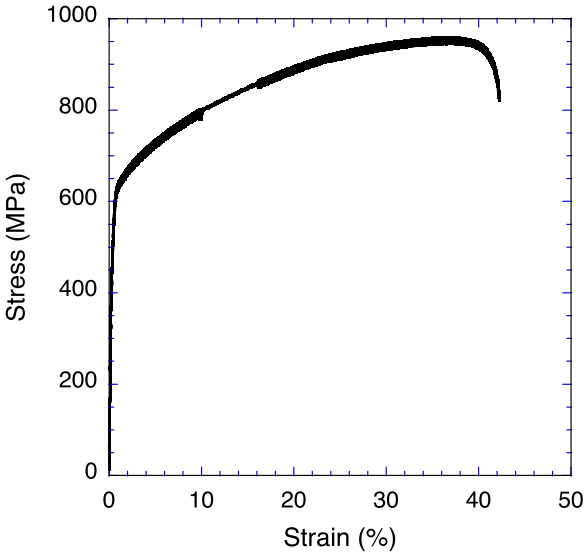

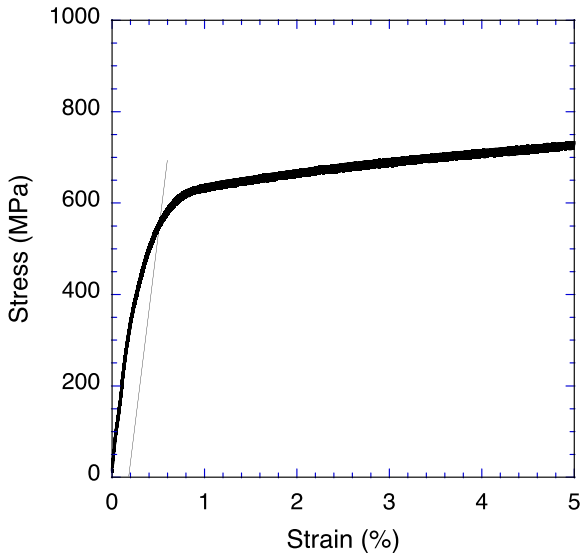

build 1

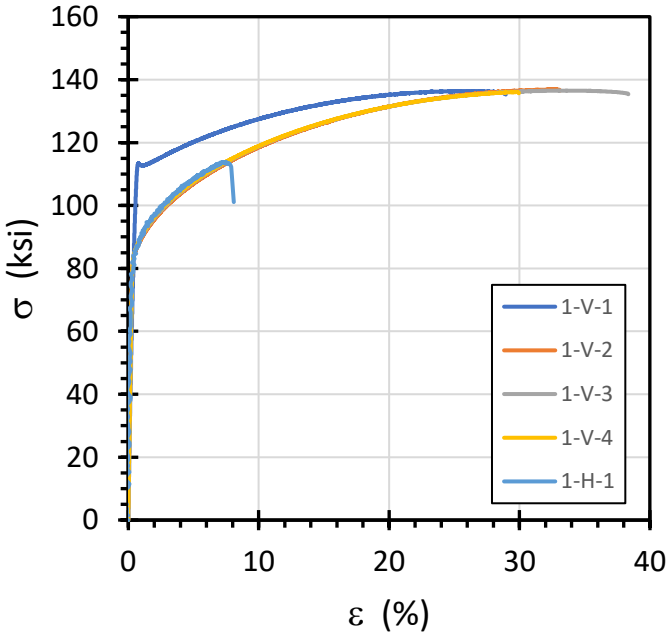

build 2

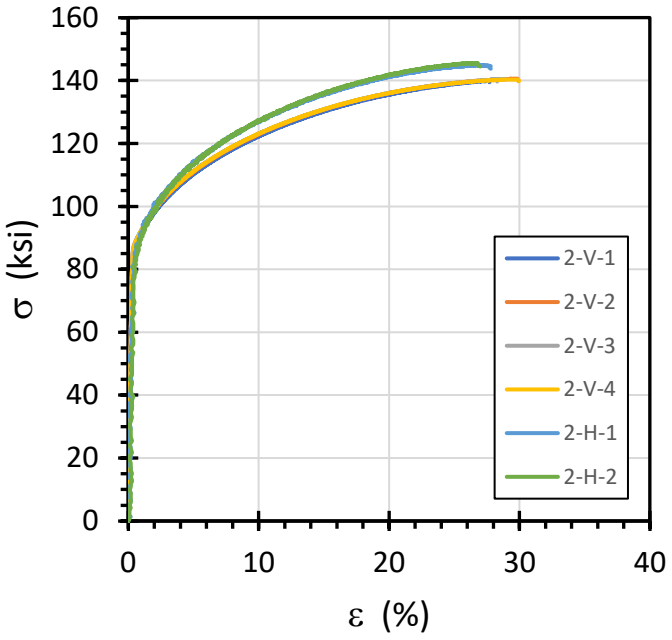

build 3

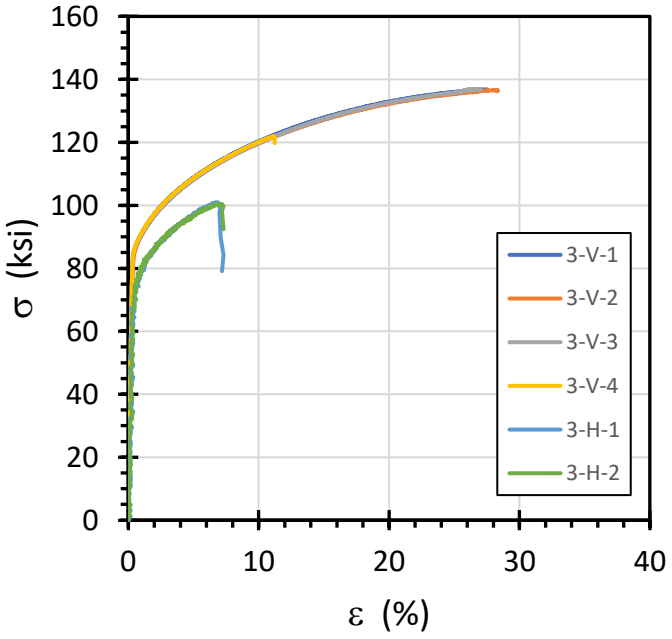

build 4

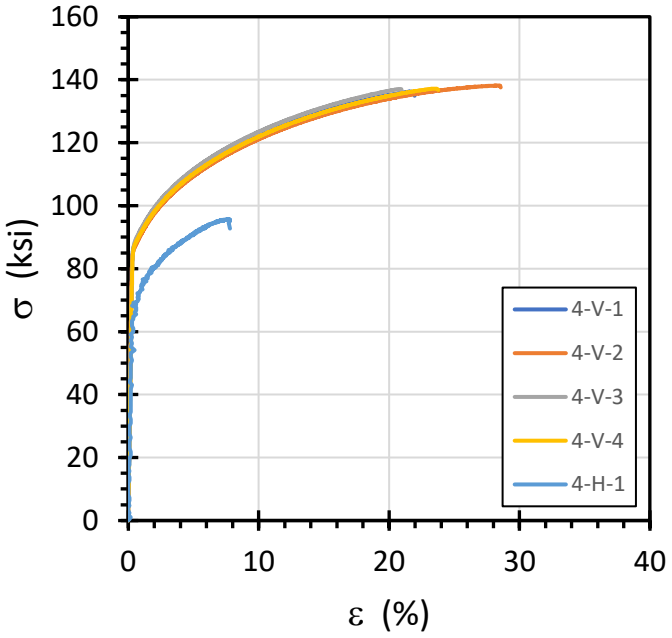

build 5

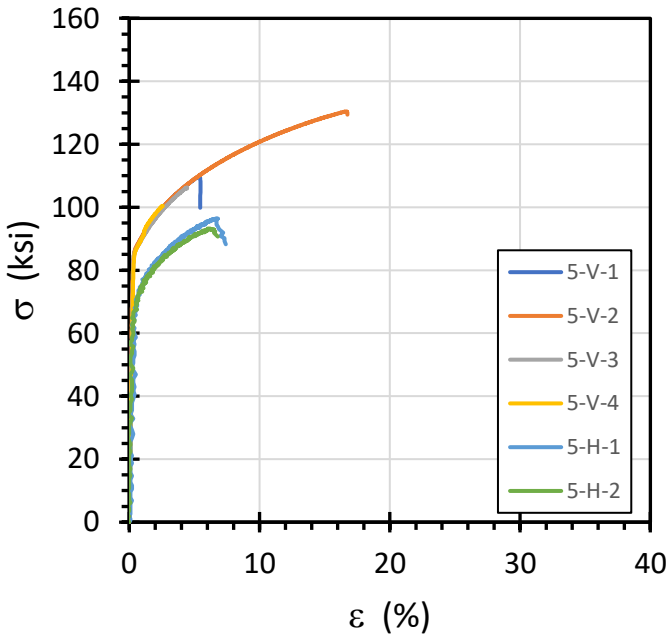

build 6

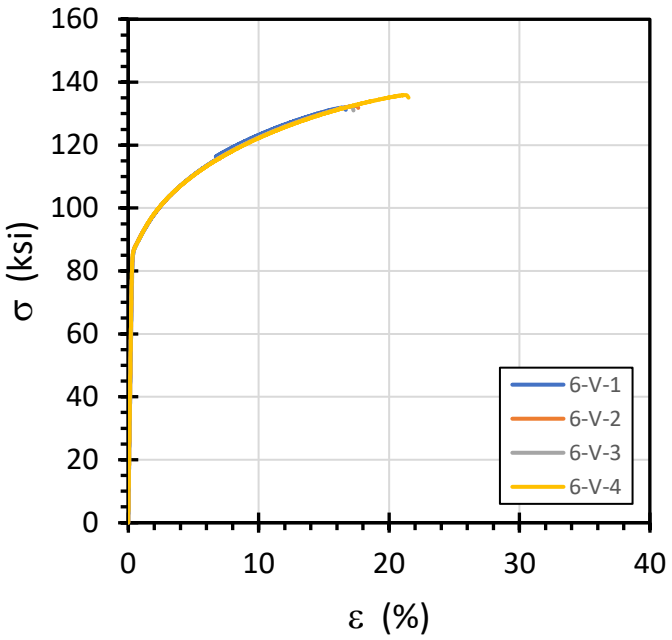

build 9

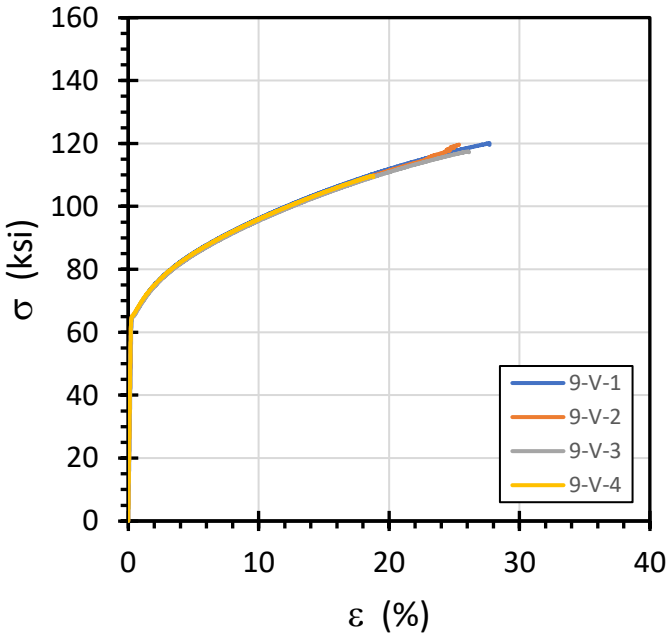

build 10

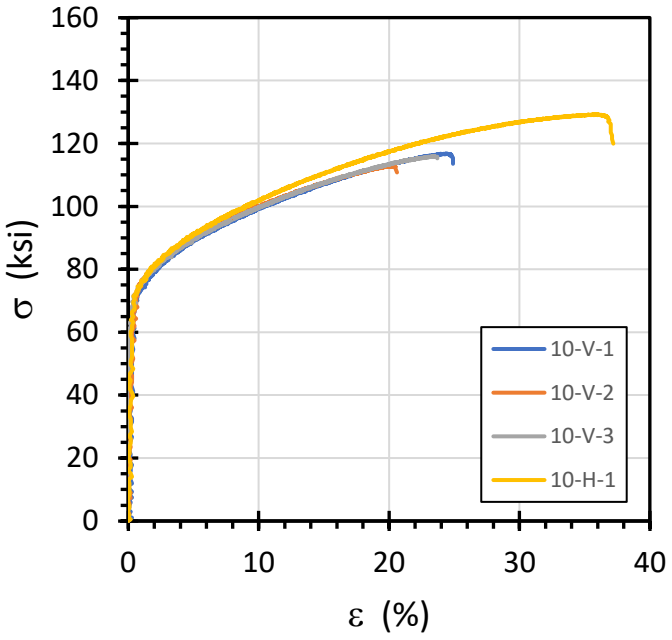

build 11

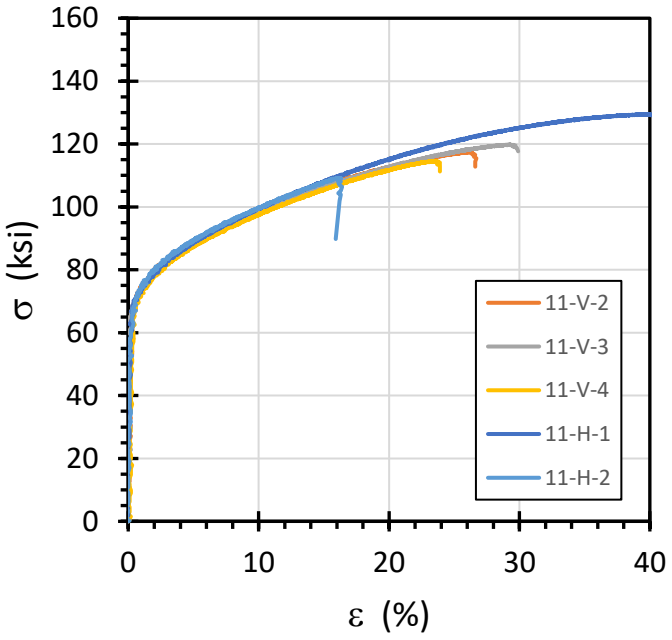

6. REFERENCES

[1] J. A. Gonzalez, J. Mireles, S. Stafford, M. A. Perez, C. Terrazas and R. B. Wicker, "Characterization of Inconel 625 Fabricated Using Powder-Bed-Based Additive Manufacturing Technologies," University of Texas, El Paso, Texas, 2018.

[2] Kuscer, Danjela, Shen and J. Zhijian, "Advanced Direct Forming Processes for the Future," 2014.

[3] RapidMade, "What is the difference between SLS and SLM?," 30 June 2014.

[4] L. Lao, Z. Y. Chua, S. K. Moon and J. Song, "Femtosecond Laser Produced Hydrophobic Hierarchical Structures on Additive Manufacturing Parts," *Nanomaterials* , vol. 8, no. 8, p. 601, 2018.

[5] S. Kumar, Advances in Additive Manufacturing and Tooling, 2014, pp. 1-2.

[6] L. Criales, "Laser Powder Bed Fusion of Nickel Alloy 625: Experimental Investigations of Effects of Process Parameters on Melt Pool Size and Shape with Spatter Analysis," International Journal of Machine Tools and Manufacture, 2017.

[7] L. e. a. Criales, "Laser Powder Bed Fusion of Nickel Alloy 625: Experimental Investigations of Effects of Process Parameters on Melt Pool Size and Shape with Spatter Analysis," *International Journal of Machine Tools and Manufacture,* pp. 3-5, 2017.

[8] M. a. M. S. (. The Minerals, "A history of superalloy metallurgy for superalloy metallurgists," *Superalloys,* pp. 399-419, 1984.

[9] H. Eiselstein and D. Tillack, "The Invention and Definition of Alloy 625.," *TMS The Minerals, Metals and Materials Society.,* Vols. Superalloys 718, 625 and Various Derivatives., p. 1–14, 1991.

[10] G. Smith, D. Tillack and S. Patel, "Alloy 625: Impressive Past/Significant Presence/Awesome Future," *TMS The Minerals, Metals and Materials Society,* Vols. Alloy 625 - Impressive Past, Significant Presence, Awesome Future, p. 35–46, 2001.

[11] V. Shakar, K. Bhanu, S. Rao and S. Mannan., "Microstructure and mechanical properties of Inconel 625 superalloy," *Journal of Nuclear Materials,* vol. 288, pp. 222-232, 2001.

[12] V. Shankar, S. L. Mannan and K. B. Sankara, "Microstructure and mechanical properties of Inconel 625 superalloy," *Journal of Nuclear Materials,* vol. 288, no. 2-3, pp. 222-232, 2001.

[13] I. Koutiri, E. Pessard, P. Peyre and O. A. a. T. D. Terris, "Influence of SLM process parameters on the surface finish, porosity rate and fatigue behavior of as-built Inconel 625 parts," Journal of Materials Processing Technology, 2018.

[14] M. Cieslak, T. Headley, T. Kollie and J. A. D. Romig, "A melting and solidification study of Alloy 625," *Metall Mater Trans A,* vol. 19, p. 2319–2331, 1988.

[15] J. J. Schirra, R. H. Caless and R. W. Hatala., The effect of the lave phase on the mechanical properties of wrought and cast+HIP Inconel 718, East Hartford: United Technologies Corporation, 1991.

[16] S. Floreen, G. E. Fuchs and W. J. Yang, "The Metallurgy of Alloy 625," *Superalloys,* pp. 13-37, 1994.

[17] R. Wickens, "Introduction to Alloy 625," LFF Group, 9 September 2019. [Online]. Available: https://www.lff-group.com/posts/introduction-to-alloy-625-part-3. [Accessed 4 April 2020].

[18] E. A. Lass, M. R. Stoudt, M. E. Williams, M. B. Katz, L. E. Levine, T. Q. Phan, T. H. Gnaeupel-Herold and D. S. Ng, "Formation of the Ni3Nb δ-Phase in Stress-Relieved Inconel 625 Produced via Laser Powder-Bed Fusion Additive Manufacturing," *Metallurgical and Materials Transactions A,* vol. 48, pp. 5547-5558, 2017.

[19] F. Zhang, L. E. Levine, A. J. Allen and M. Stoudt, "Effect of Heat Treatment on the Microstructural Evolution of a Nickel-Based Superalloy AdditiveManufactured by Laser Powder Bed Fusion," *Acta Materialia,* vol. 152, pp. 200-214, 2018.

[20] Metallic Materials Properties Development and Standardization (MMPDS-14), Battelle Memorial Institute, 2019.

[21] "Special Metals Corporation," Special Metals Corporation, [Online]. Available: https://www.specialmetals.com/tech-center/alloys.html. [Accessed June 2020].

[22] N. D. Ghate, A. Pandey and A. Shrivastava, "Annealing of Additively Manufactured Inconel 625," in *TMS 2020 149th Annual Meeting & Exhibition Supplemental Proceedings,* Pittsburgh, 2020.

[23] "Industrial Steel Treating Co.," IST, [Online]. Available: https://www.indstl.com. [Accessed 18 May 2020].

[24] "AZO Materials," 27 July 2011. [Online]. Available: https://www.azom.com/.

[25] "Kobelco. What is Isostatic Pressing?," Kobelco, [Online]. Available: https://www.kobelco.co.jp. [Accessed 18 May 2020].

[26] I. Koutiri, E. Pessard, P. Peyre, T. O, Amlou and T. D. Terris, "Influence of SLM process parameters on the surface finish, porosity rate and fatigue behavior of as-built Inconel 625 parts,," Journal of Materials Processing Technology, 2018.

[27] F. Zhang, L. E. Levine, A. J. Allen, C. E. Campbell, E. A. Lass, S. Cheruvathur, M. R. Stoudt, M. E. Williams and Y. Idell, "Homogenization kinetics of a nickel-based superalloy produced by powder bed fusion laser sintering," *Scripta Materiala,* vol. 131, pp. 98-102, 2016.

[28] L. Xue, Y. Li, T. V. Daam and C. Bampton, "Investigation of laser consolidation for manufacturing functional net-shape components for potential rocket engine applications," in *Proceedings of the 26th International Congress on Applications of Lasers and Electro-Optics,* Orlando, 2007.

[29] EOS GmBH, "“Material Data Sheet: EOS NickelAlloy IN625," 2010.

[30] E. e. a. Betts, "Using innovative technologies for manufacturing rocket engine hardware," 2011.

[31] Yadroitsev and e. al., "Mechanical properties of samples fabricated by selective laser," *14èmes Assises Européennes du Prototypage & Fabrication Rapide,* pp. 24-25, 2009.

[32] Optomec, "LENS Superalloys Material Data Sheet," 2015.

[33] L. E. Murr, E. Martinez, S. M. Gaytan, D. A. Ramirez, B. I. Machado, P. W. Shindo, J. L. Martinez, F. Medina, D. C. J. Wooten, U. Ackelid and R. B. Wicker, "Microstructural architecture, microstructures, and mechanical properties for a nickel-base superalloy fabricated by electron beam melting," *Metallurgical and Materials Transactions A.,* vol. 42, no. 11, pp. 3491-3508, 2011.

[34] M. Rombouts and M. Mertens, "Laser metal deposition of Inconel 625: Microstructure and mechanical properties," *Journal of Laser Applications,* vol. 24, no. 5, pp. 232-240, 2012.

[35] R. M, G. M. and R. Persoons, "Material study of laser cladded Inconel 625," *Journal of Materials Processing Technology,* vol. 217, pp. 232-240, 2011.

[36] K. N. Amato, S. .. Gaytan, L. E. Murr, E. Martinez, P. W. .Shindo, J. Hernandez, S. Collins and F. Medina, "Microstructures and mechanical behavior of Inconel 718 fabricated by selective laser melting," *Acta Materialia,* vol. 60, no. 5, pp. 2229-2239, 2012.

[37] EOS GmbH, "Material Data Sheet: EOS NickelAlloy IN625," 2011.

[38] B. Dutta, J. Choi, S. Palaniswamy and L. Song, "Rapid Manufacturing g and remanufacturing of DoD components using direct metal deposition," *The AMMTIAC Quarterly,* vol. 6, no. 2, p. 5, 2011.

[39] A. Anam, "Microstructure and mechanical properties of selective laser melted superalloy IN625," University of Louisville, Louisville, 2018.

[40] C. Montgomery, J. Beuth, L. Sheridan and N. Klingbeil, "Process Mapping of Inconel 625 in Laser Powder Bed Additive Manufacturing," pp. 1195-1204, 2015.

[41] L. E. Criales, Y. M. Arisoy, B. Lane, S. Moylan, A. Donmez and T. Ozel, "“Laser Powder Bed Fusion of Nickel Alloy 625 : Experimental Investigations of e Ff Ects of Process Parameters on Melt Pool Size and Shape with Spatter," International Journal of Machine Tools and Manufacture, 2015.

[42] S. A. Khairallah, A. T. Anderson, A. M. Rubenchik and W. E. King, "Laser powder-bed fusion additive manufacturing Physics of complex melt flow and formation mechanisms of pores, spatter, and denudation zones," *Acta Materiala,* pp. 36-45, 2016.

[43] "Material Fatigue," Comsol, 15 March 2016. [Online]. Available: https://www.comsol.com/multiphysics/material-fatigue. [Accessed 7 May 2020].

[44] L. O. A. Affonso, Fatigue Fractures. Machinery Failure Analysis Handbook, Gulf Publishing Company, 2007.

[45] "Stress-Life Diagram (S-N Diagram)," 2018.

[46] P. P. D.M. Lambert, "Evaluation of the effect of surface finish on high cycle fatigue of IN718," Jacobs ESSSA Group, NASA-MSFC, Alabama, 2016.

[47] M. Aydinöz, F. Brenne, M. Schaper, C. Schaak, W. Tillmann, J. Nellesen and T. Niendorf, "On the microstructural and mechanical properties of post-treated additively manufactured Inconel 718 superalloy under static anc cyclic loading," pp. 246-258, 2016.

[48] D. B. Witkin, P. Adams and T. Albright, "Microstructural evolution and mechanical behavior of nickel-based superalloy 625 made by selective laser melting," in *Laser 3D Manufacturing II*, San Francisco, 2015.

[49] D. B. Witkin, D. N. Patel, H. Helvajian, L. Steffeney and A. Diaz, "Surface Treatment of Powder-Bed Fusion Additive Manufactured Metals for Improved Fatigue Life," *Journal of Materials Engineering and Performance volume,* vol. 28, pp. 681-692, 2019.

[50] S. Subresh, Fatigue of Materials, 2nd, Cambridge, UK: Cambridge University Press, 1998.

[51] D. Z. Avery, O. G. Rivera, C. J. T. Mason, B. J. Phillips and J. B. Jordon, "Fatigue Behavior of Solid-State Additive Manufactured Inconel 625," *JOM,* vol. 70, p. 2475–2484, 2018.

[52] P. Gauthier, D. R. H. and J. & Auvinet, "Secondary cracking process during fatigue crack propagation. Engineering Fracture Mechanics," 1973.

[53] M. Mazur, M. Benoit, M. Easton and M. Brandt, "Selective Laser Melting of Inconel 625 Alloy with Reduced Defect Formation," in *8th International Congress on Applications of Lasers & Electro-Optics (ICALEO),* Orlando, 2019.

[54] S. M., Y. Tse and C. Tuck, "Effect of the build orientation on the mechanical properties and fracture modes of SLM Ti–6Al–4V," *Materials Science and Engineering: A,* vol. 616, pp. 1-11, 2014.

[55] P. S., W. Chen and W. Wang, "A quantitative model of keyhole instability induced porosity in laser welding of titanium alloy," *Metallurgical and Materials Transactions A,* vol. 45, no. 6, pp. 2808-2818, 2014.

[56] X. Hu, G. Zhao, Y. Jiang, X. Ma, F. Liu, J. Huang and C.-L. Dong, "Experimental Investigation on the LCF Behavior Affected by Manufacturing Defects and Creep Damage of One Selective Laser Melting Nickel-Based Superalloy at 815 °C," Acta Metallurgica Sinica (English Letters), 2019.

[57] Standard Specification for Additive Manufacturing Nickel Alloy (UNS N06625) with Powder Bed Fusion (ASTM F3056-14), ASTM INTERNATIONAL, 2014.

[58] Rice, R. C, "Metallic Materials Properties Development and Standardization (MMPDS-14)," Battelle Memorial Institute, 2019.

[59] S. R. Institute, "AM Inconel 625 Lit. Review," Southwest Research Group, San Antonio, 2020.

[60] Military Handbook: Matellic Materials and Elements for Aerospace Vehicles Structures, United States Department of Defense, 1998.

[61] D. Verdi, M. A. Garrido, P. Poza and C. J. Munez, "Microscale evaluation of laser cladded Inconel 625 exposed at high temperature in air," *Materials & Design,* vol. 114, pp. 326-338, 2016.

[62] S. Gribbin, S. Ghorbanpour, N. C. Ferreri, J. Bicknell, I. Tsukrov and M. Knezevic, "Role of grain structure, gran boundaries, crystallographic texture, precipitates, and porosity on fatigue behavior of Inconel 718 at room and elevated temperatures," *Materials Characterization,* vol. 149, pp. 184-197, 2019.

[63] J. A. Graham, Fatigue Design Handbook, Society of Automotive Engineers. Iron and Steel Technical Committee, 1968.

[64] C. Li, R. White, X. Y. Fang, M. Weaver and Y. B. Guo, "Microstructure evolution characteristics of Inconel 625 alloy from selective laser melting to heat treatment," *Materials Science & Engineering A,* pp. 2-10, 2017.

[65] D. Witkin, D. Patel and G. Bean., "Notched fatigue testing of Inconel 718 prepared by selective laser melting.," Fatigue & Fracture of Engineering Materials & Structures, 2018.

[66] S. K. A. H. Hallberg and B. Skallerud, "Crystal plasticity modeling of microstructure influence on fatigue crack initiation in extruded Al6082-T6 with surface irregularities," 2018.